

**Master Thesis**

**Large-scale Magnetohydrodynamic Numerical  
Simulations on the Solar Flux Emergence and  
the Formation of Active Region**

**Shin Toriumi**

鳥海 森

**Space and Planetary Science Group  
Department of Earth and Planetary Science  
Graduate School of Science, The University of Tokyo**

**February 21, 2011**



# Abstract

It is widely accepted that the solar active regions including sunspots are the consequence of the buoyant rise of magnetic flux from the convection zone, i.e, flux emergence. In this Thesis, we perform large-scale two- and three-dimensional magnetohydrodynamic (MHD) simulations to study flux emergence and the resultant formation of active region.

First, we run two-dimensional (2D) calculations for the evolutions in the cross-sections parallel (Chapter 3) and perpendicular (Chapter 4) to the tube axis and find the following results. The initial flux embedded deep in the adiabatically stratified convection zone at a depth of 20,000 km starts rising through the interior. As the flux reaches the surface, it slows down due to the isothermally stratified photosphere in front and extends horizontally to create a flat magnetized layer around the surface. Since the flux is continuously transported from below, the surficial field increases with time. When the magnetic pressure gradient in the photosphere locally satisfies the criterion for the magnetic buoyancy instability, the magnetic field bursts again into the rarefied upper atmosphere. Eventually, magnetic loops are built in the high-temperature corona. By conducting parametric surveys, we find that the magnetic flux tube that yields an actual active region is expected to have a field strength of  $10^4$  G, a total flux of  $(10^{21}-10^{22})$  Mx, and a sufficient twist  $> 2.5 \times 10^{-4} \text{ km}^{-1}$  at  $-20,000$  km in the convection zone.

Applying these values as the initial condition, we then carry out a simulation in three-dimension (3D) and confirm that the emergence process observed in the 2D experiments above is also consistent in 3D (Chapter 5). Moreover, several magnetic elements separate horizontally at the photosphere and show shearing motions as to create main sunspots,

which is well in accordance with observations. On the basis of the numerical results, we newly suggest a theoretical model for the flux emergence and the formation of active region.

By conducting smaller-scale 3D experiments from a depth of 1700 km, we also study the dependence of the flux evolution on the twist strength of the initial flux tube (Chapter 6). We figure out that, when the initial twist is strong, the tube keeps its coherency and evolves directly into the corona with a slight deceleration at the photosphere. The rise time becomes longer with decreasing twist, and the weakest twist tube stops at the photosphere, never to re-emerge.

# 要旨

黒点を含む太陽の活動領域は、対流層から磁束管が浮上することで形成されると考えられている。これを浮上磁場と呼ぶ。本論文では、浮上磁場と活動領域の形成について研究することを目的として、大規模な2次元・3次元磁気流体(MHD)シミュレーションを行った。

はじめに2次元計算を、磁束管の軸に平行(第3章)および垂直(第4章)な断面内における発展について2通り行い、いずれについても以下のようないくつかの結果を得た。初期条件として磁束を対流層の深さ2万kmに設置し、浮上を開始させた。太陽表面に接近すると、磁束は上方にある等温成層した光球の影響を受けて減速し、水平に広がることで平板状の磁気構造を形成した。磁束は下方から継続的に輸送されるため、表面磁場は時間とともに増加した。光球で磁気圧勾配が局所的に磁気浮力不安定条件をみたすと、磁場は希薄な上空大気へ向けて再び浮上を開始した。最終的に高温コロナに磁気ループが形成された。また、パラメータ研究を行った結果、実際の観測と一致する活動領域を形成するような磁束管は、対流層の深さ2万kmにおいて磁場強度 $10^4$ G、総磁束量( $10^{21}$ – $10^{22}$ )Mx、ねじれ強度 $>2.5\times10^{-4}\text{ km}^{-1}$ を持つと期待されることが分かった。

次に、以上で得られた物理量を初期条件として3次元数値計算を行い、2次元計算で見られた浮上過程が3次元計算でも一致することを確認した(第5章)。また、太陽表面で複数の磁気要素が水平に分裂し、黒点を形成するようにシア運動を示した。これは活動領域観測によく一致する。さらに、数値計算の結果に基づいて浮上磁場と活動領域形成の理論モデルを新たに提案した。

また、対流層深さ1700kmからの小規模な3次元浮上磁場計算を用いて、磁束

浮上の初期磁束管ねじれ強度に対する依存性を研究した(第6章)。その結果、初期ねじれ強度が強い場合には磁束管は構造を保ち、光球でほとんど減速を示さず直接的にコロナへと浮上することが分かった。ねじれが弱くなるほど浮上速度は遅くなり、最もねじれが弱い場合では磁束管は光球で停止し再浮上は見られなかった。

# Contents

<b>Abstract</b>	<b>i</b>
<b>要旨</b>	<b>iii</b>
<b>1 General Introduction</b>	<b>1</b>
1.1 Flux Emergence and Active Region . . . . .	1
1.2 Observational Characteristics of Flux Emergence . . . . .	4
1.2.1 Birth of Active Region . . . . .	4
1.2.2 Multi-step Evolution . . . . .	7
1.2.3 Recent High-resolution Observations . . . . .	10
1.2.4 Summary of this Section . . . . .	10
1.3 Numerical Analyses and Theoretical Modelings of Flux Emergence . . . . .	11
1.3.1 Flux Emergence and the Dynamo Theory . . . . .	11
1.3.2 Thin-flux-tube Approximation . . . . .	13
1.3.3 Twist Component of the Flux Tube . . . . .	14
1.3.4 Emergence from the Surface to the Corona . . . . .	15
1.3.5 Summary of this Section . . . . .	22
1.4 Purpose of the Thesis . . . . .	22
<b>2 Basic Equations</b>	<b>25</b>
<b>3 Two-dimensional Experiment: Undular Evolution</b>	<b>29</b>
3.1 Introduction . . . . .	29

3.2	Numerical Model . . . . .	29
3.3	General Evolution . . . . .	34
3.3.1	First Stage ( $0 < t/\tau_0 < 700$ ) . . . . .	34
3.3.2	Second Stage ( $700 < t/\tau_0 < 1900$ ) . . . . .	36
3.3.3	Third Stage ( $1900 < t/\tau_0 < 2000$ ) . . . . .	40
3.3.4	Fourth Stage ( $t/\tau_0 > 2000$ ) . . . . .	42
3.4	Parameter Survey and Discussion . . . . .	44
3.4.1	Direct emergence . . . . .	44
3.4.2	Two-step emergence . . . . .	47
3.4.3	Failed emergence . . . . .	49
3.5	Conclusions . . . . .	53
<b>4</b>	<b>Two-dimensional Experiment: Cross-sectional Evolution</b>	<b>57</b>
4.1	Introduction . . . . .	57
4.2	Numerical Model . . . . .	58
4.3	Results . . . . .	61
4.3.1	Magnetic Fields and Vorticity . . . . .	65
4.3.2	Comparison with an Analytic Model . . . . .	69
4.3.3	Further Evolution to the Corona . . . . .	75
4.4	Dependence on the Initial Twist and the Field Strength . . . . .	78
4.5	Summary and Discussion . . . . .	84
<b>5</b>	<b>Three-dimensional Experiment</b>	<b>89</b>
5.1	Introduction . . . . .	89
5.2	Numerical Setup . . . . .	90
5.3	Results . . . . .	94
5.3.1	General Evolution . . . . .	94
5.3.2	Magnetic Structure in the Convection Zone . . . . .	96
5.3.3	Magnetic Buoyancy Instability at the Surface . . . . .	99

5.3.4	Time-evolution of the Photospheric Magnetic and Flow Fields . . .	105
5.3.5	Coronal Magnetic Field and the Shearing Motion . . . . .	110
5.4	Discussion . . . . .	114
5.4.1	Overall Evolution . . . . .	114
5.4.2	Comparison with NOAA AR 5617 . . . . .	115
5.4.3	A Model for the Flux Emergence and the Formation of Active Region . . . . .	117
5.4.4	Comparison with 2.5D Cross-sectional Experiment . . . . .	118
5.5	Conclusions . . . . .	120
<b>6</b>	<b>Dependence on the Twist Intensity</b>	<b>123</b>
6.1	Introduction . . . . .	123
6.2	Numerical Setup . . . . .	127
6.3	Results . . . . .	129
6.3.1	Overview of the Results . . . . .	129
6.3.2	Parameter Study on the Twist Strength . . . . .	134
6.3.3	Comparison of the Magnetic Field Structure at the Surface . . . .	135
6.3.4	Undulating Configuration of the Photospheric Field Lines . . . .	138
6.3.5	Magnetic Energy in the Atmosphere and the Initial Tube's Twist .	138
6.4	Summary . . . . .	141
6.5	Discussion . . . . .	142
6.5.1	Twist Intensity and the Interchange Instability . . . . .	142
6.5.2	Twist of the Actual Flux Tube in the Sun . . . . .	143
6.5.3	Formation of Undulating Photospheric Fields . . . . .	144
6.5.4	For Future Observations . . . . .	144
<b>7</b>	<b>Summary</b>	<b>147</b>
7.1	Emergence from a Depth of -20,000 km . . . . .	147
7.2	Dependence on the Initial Tube's Twist . . . . .	149

<b>8 Discussion</b>	<b>151</b>
8.1 Effect of Thermal Convection . . . . .	151
8.2 Tube Twist and Active Region Helicity . . . . .	152
8.3 Future Works . . . . .	153
<b>A Instabilities of a Magnetized Atmosphere</b>	<b>155</b>
A.1 Interchange and Undular Mode Instabilities . . . . .	155
A.2 Derivation of Acheson's Condition for the Interchange Mode Instability .	158
A.2.1 Derivation by the Thought Experiment . . . . .	158
A.2.2 Derivation from Newcomb's Condition . . . . .	160
A.3 Derivation of Acheson's Condition for the General Undular Mode Instability	161
A.4 Normal Mode Analysis of Undular Mode Instability . . . . .	162
<b>B Tips on Flux Emergence Simulation</b>	<b>169</b>
B.1 Computational Difficulty of the Emergence from the Base of the Convection Zone . . . . .	169
B.2 Importance of the Coriolis Effect . . . . .	170
<b>Acknowledgments</b>	<b>173</b>
<b>References</b>	<b>175</b>

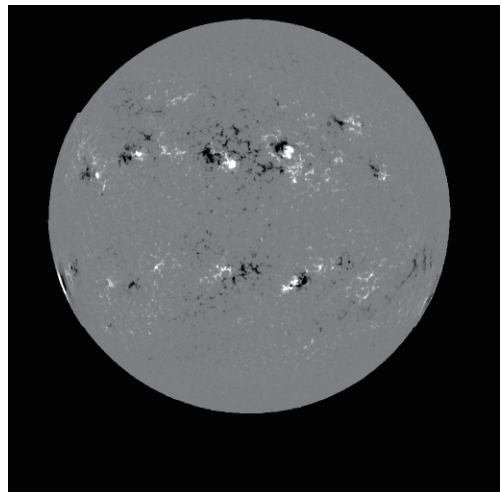
# Chapter 1

## General Introduction

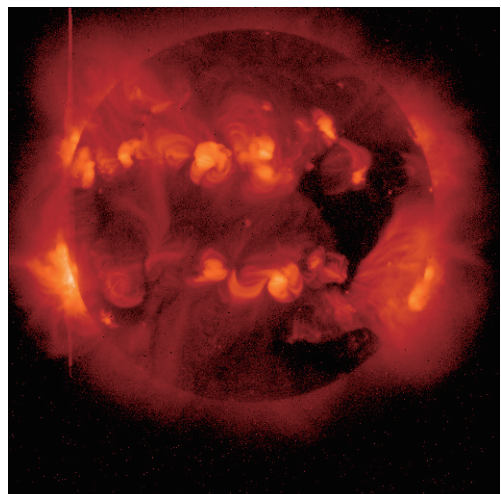
### 1.1 Flux Emergence and Active Region

Solar activity is highly related with magnetism. Figure 1.1(a) shows the full disk magnetogram (magnetic field intensity on the surface), on which we can see two alignments of bipolar active regions in northern and southern hemisphere. Each region consists of positive (white) and negative (black) magnetic elements. The place where the magnetic flux seems less dense is called a quiet Sun. The flux in this area is thought to originate from fragmented active region fields. Seen in X-ray (see Figure 1.1(b)), active regions appear as high-temperature bright coronal loops. Some strongest loops may cause flares or CMEs through magnetic reconnection. They have a violent impact on the interplanetary space around the Earth. In the Figures 1.1(a) and 1.1(b), the sites of coronal structures are highly associated with the surface magnetism. At the same time, there is hardly any coronal loop with X-ray emission over the quiet Sun. Thus, we can see that solar activity has a direct relation with magnetic fields.

Active regions are generally thought to be the consequence of flux emergence, i.e., dynamo-generated magnetic fluxes risen from the deep convection zone (Parker, 1955). The flux rotates around the Sun as a toroidal flux rope, which finally appears as an alignment of active regions at the surface (see Figure 1.1(a)). Observations indicate that the



(a)



(b)

Figure 1.1: (a) Solar magnetogram taken by Kitt Peak Solar Observatory. This image shows the line-of-sight magnetic field on the solar photosphere on May 11, 2000. White (black) indicates a positive (negative) field. (b) X-ray image taken by Soft X-ray Telescope (SXT) on board *Yohkoh* satellite taken on the same day as Panel (a). Each group of bright loops is an active region. Both images are cited from Fan (2009).

flux tube should be twisted and strong enough so as not to be disintegrated by the turbulent motion during its ascent through the convection zone. For generating such a strong flux, the subadiabatically stratified overshoot region at the bottom of the convection zone has been suggested as a suitable place (Parker, 1975). Therefore, flux emergence should be understood in a self-consistent manner as a coherent process from the bottom of the convective layer to the upper atmosphere through the surface.

Figure 1.2 shows an illustration of the widely-accepted solar dynamo model. In this

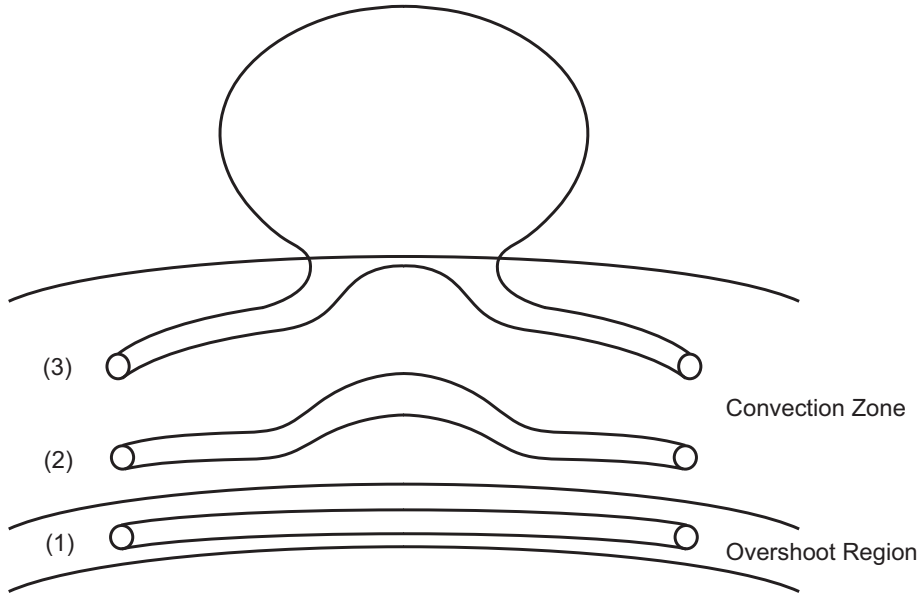


Figure 1.2: Flux emergence and the formation of an active region. (1) In the overshoot region at the bottom of the convection zone, the velocity shear (differential rotation) stretches and amplifies the global toroidal flux tube. (2) The tube becomes buoyantly unstable and rises through the interior. (3) Finally, the tube penetrates the surface to make an active region. The consequent coronal loops are the continuation of the toroidal flux extending toward the deep convection zone.

figure, (1) a toroidal magnetic flux tube is created in the overshoot region at the bottom of the convection zone. (2) The flux rises through the interior due to its magnetic buoyancy, and (3) finally appears at the surface to make an active region. It is thought that the cross-section of the emerged flux is the sunspots and pores, and the coronal loops are the continuation of the flux rope extending deeper into the interior.

## 1.2 Observational Characteristics of Flux Emergence

### 1.2.1 Birth of Active Region

Observationally, the first appearance of the new emerging flux is the small and bright bipolar plage in the chromospheric Ca II H and K line cores (Fox, 1908; Sheeley, 1969). Soon the arch filament system (AFS) composed of parallel dark fibrils appears in the line core of H $\alpha$  (Bruzek, 1967, 1969). The fibrils are magnetic field lines connecting the faculae of opposite polarity. They are (20–30) Mm in length with the maximum height of 5 Mm. The apex of a loop rises upward at the speed of up to 10 km s $^{-1}$ , while, in both legs, the redshift up to 50 km s $^{-1}$  is observed, i.e., the plasma flows down with the speed exceeding a local sound velocity. Also, in the photosphere, small pores are formed at the root of chromospheric filaments with downflows up to about 1 km s $^{-1}$ . Figure 1.3 shows AFS and plages in H $\alpha$  and the corresponding pores in H $\alpha \pm 1$  Å. The pores are located at the footpoints of the chromospheric arch filaments. Ellerman bombs (Ellerman, 1917), also known as moustaches due to the shape of the H $\alpha$  spectral profile, are found under the growing AFSs (Bruzek, 1967).

The faculae of opposite polarity separates, initially at the rate of  $> 2$  km s $^{-1}$ , and the rate drops to (1.3–0.7) km s $^{-1}$  during the next 6 hours (Harvey & Martin, 1973). New magnetic flux emerges continuously within the opposite polarities. If the flux is sufficient, the pores are gathered, and gradually sunspots are formed near the leading and the following plages (Zirin, 1972, 1974). Zirin (1972) named this area as an emerging flux region (EFR).

Zwaan (1985) suggested a model for the emergence of magnetic flux (see Figure 1.4). The magnetic flux emerges as a bundle of separated flux tubes from the convection zone. Magnetic elements at the surface (i.e., the cross-sections of the flux tubes) separate with each other, and are concentrated into sunspots at the both ends of the active region.

Zwaan (1978, 1987) introduced the hierarchy of magnetic elements of EFR. The

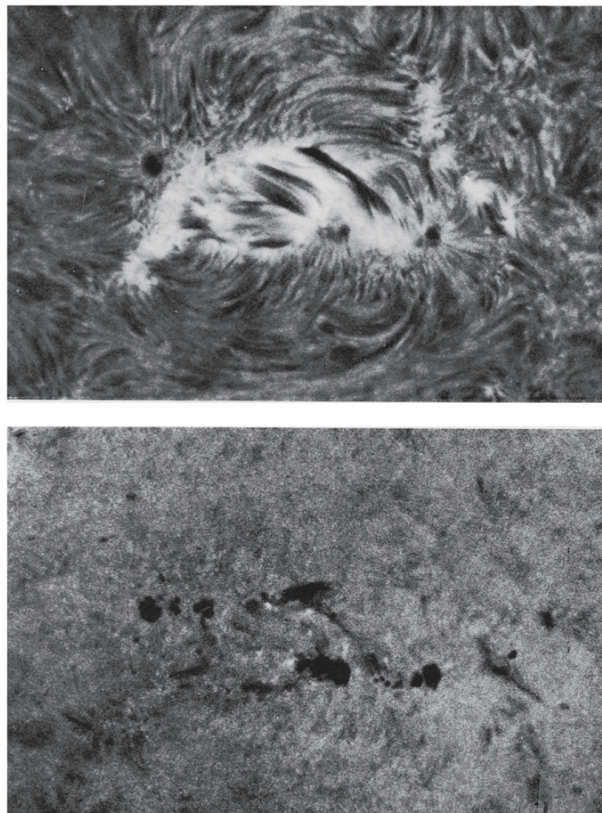


Figure 1.3: Active region seen from above. (*Top*) Filtergram taken in  $H\alpha$  line core shows arch filament system (AFS) connecting leading and following plages. (*Bottom*) Filtergram at  $H\alpha \pm 1\text{\AA}$  shows all spots with bright points (Ellerman bombs). Both images are from Bruzek (1967).

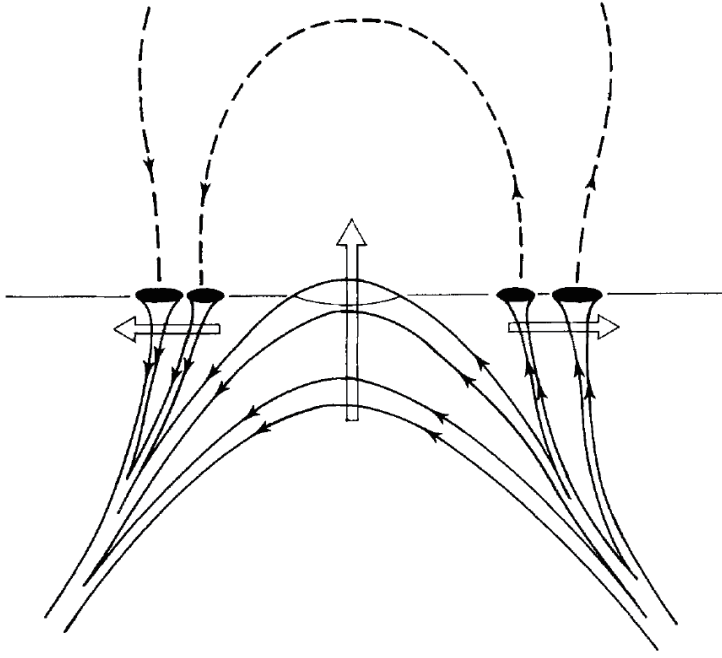


Figure 1.4: Model of flux emergence by Zwaan (1985). At the surface, magnetic elements of the opposite polarity separate and coalesce into main sunspots.

sunspots with the flux  $3 \times 10^{22} > \Phi > 5 \times 10^{20}$  Mx have penumbras. In this group, the umbral field strength is between (2900–3300) G, sometimes exceeding 4000 G. The flux of pores (small spots without penumbras) are between  $5 \times 10^{20} > \Phi > 2.5 \times 10^{19}$  Mx with the field strength  $\sim 2000$  G. When the flux is less than  $10^{20}$  Mx, EFRs do not develop beyond ephemeral active regions (Harvey & Martin, 1973).

All sunspots are formed by the coalescence of pores: in the EFR, pores stream into the main sunspot of each polarity. Upon observations, Vrabec (1974) suggests two types of magnetic flux inflow that pores move into main sunspots (see Figure 1.5). The first is that the newly emerged pores of opposite polarity separate with each other and are transported directly into the boundary of supergranular cell by the convective flows, forming main spots (Figure 1.5(a)). In the second case, emerged magnetic elements are arranged in the alignment of pores of the same polarity behind the main spot, and the elements stream along the alignment into the main spot (Figures 1.5(b) and (c)). In this scheme, magnetic elements are thought to be advected by the convection. However, Harvey &

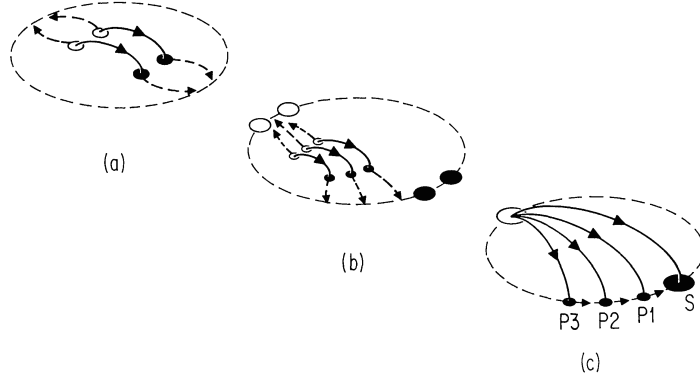


Figure 1.5: Two schemes of magnetic flux inflow into the main sunspots (Vrabec, 1974). (a) Pores appear near the center of a supergranular cell outlined by the dashed lines. Then they are transported by the material outflow to the cell boundary where the sunspots form. (b)-(c) The pores are transported into the supergranulation cell boundary to make an aligned strings of pores. Then they move into the sunspot along the axis of string.

Martin (1973) found that emerging fluxes occur adjacent to the chromospheric network, i.e., the boundary of a supergranule. Zirin (1974) insisted that there is no relation between EFR and supergranulation.

### 1.2.2 Multi-step Evolution

An active region observed by Strous et al. (1996) and Strous & Zwaan (1999) is somewhat similar to the latter case by Vrabec (1974) (see Figures 1.5(b) and (c)). Using Swedish Vacuum Solar Telescope, Strous et al. (1996) studied the motion of magnetic elements (faculae, pores, and sunspots) in the NOAA AR 5617 and found the hierarchy of movement of these elements: faculae of either polarity scatter throughout the region and move obliquely toward the edges of the region, which is defined by strings of pores of the same polarity. Faculae move faster ( $0.84 \text{ km s}^{-1}$ ) than the pores ( $0.73 \text{ km s}^{-1}$ ). The pores move along the edges toward the major sunspots of their own polarity, and the major spots of either polarity move apart (at the rate  $0.50 \text{ km s}^{-1}$ ). Strous & Zwaan (1999) found that flux emergence occurs recurrently to form a pattern with a wavelength of about 8 Mm (Figure 1.6). The spatial patterns of the emergence locations, the emergence events themselves,

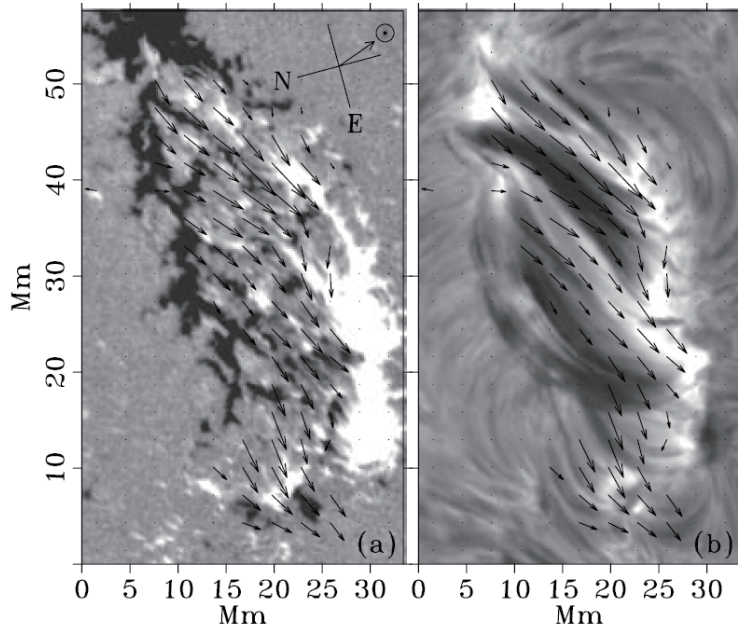


Figure 1.6: (a) Photospheric magnetogram and (b) chromospheric arch filament system (AFS) of NOAA AR 5617 (Strous & Zwaan, 1999).

subsequent footpoint motions, H $\alpha$  arch filament systems, and the alignments of unipolar faculae show a preferred orientation that fits Hale's polarity law. From these findings, they adapt a model that each emergence occurs within a set of slightly curved, nearly parallel vertical sheets (Figure 1.7). The photospheric undulations with a wavelength of  $\sim 8$  Mm is due to the undular instability of buoyant rising flux loops (Parker, 1979).

Using data of NOAA AR 8844 taken by balloon-borne Flare Genesis Experiment, Bernasconi et al. (2002) found that the moving dipolar features (MDFs) merge into the main spots. They observed that the photospheric fields have undulating, nearly horizontal shape, and the dips of the field are the MDFs. Using same data sets, Georgoulis et al. (2002) found that Ellerman bombs occur on separatrix, or quasi-separatrix layers in the low chromosphere, i.e., Ellerman bombs is caused by the reconnection. Pariat et al. (2004) found that the Ellerman bombs are correlated with bald patches (the sites where the field lines submerge) and suggested the resistive emergence model that the undulating photospheric fields reconnect with each other to make larger coronal loops (see Figure 1.8).

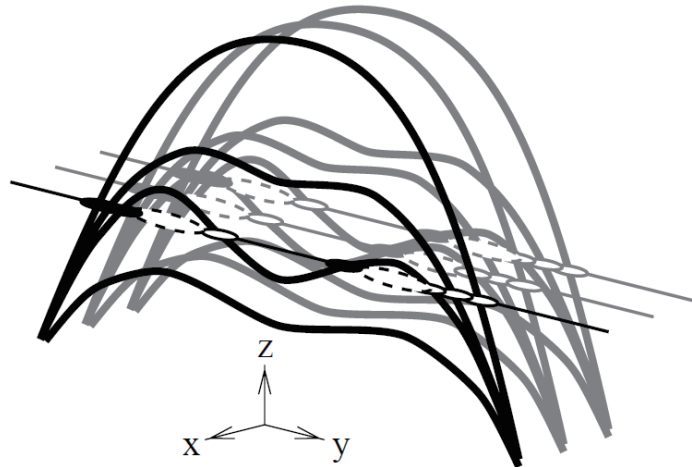


Figure 1.7: Model of flux emergence by Strous & Zwaan (1999). A rising fields undulate at the surface and emerge at multiple area. The black and white ellipses indicate the photospheric footpoints of both polarities. Each emergence event occurs in a vertical sheet. In this figure, three nearly parallel sheets are illustrated. The white and black patches flow out into magnetic alignments, which follow the main sunspots of the same polarity.

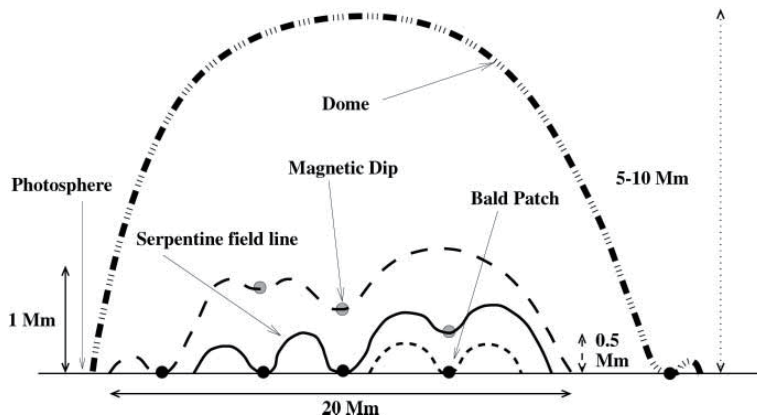


Figure 1.8: An illustration of the resistive emergence model by Pariat et al. (2004). At the photosphere, field lines are undulating, of which the wavelength is due to the Parker instability. At the dip of serpentine fields, magnetic reconnection occurs in a bold patch to make a longer coronal field overlying the whole region. Through the reconnection, the trapped plasma is ejected downward (Ellerman bomb).

### 1.2.3 Recent High-resolution Observations

Solanki et al. (2003) observed a young active region using full Stokes vectors of He I line to measure the magnetic fields in the upper chromosphere, which had been difficult to see. They plotted the three-dimensional structure of emerging magnetic loops from the chromospheric magnetogram, confirming that the loops are reminiscent of arch filament system observed in H $\alpha$ . The field strength decreases with height from about 390 G and 500 G at the two chromospheric footpoints to below 50 G at the apex.

Magara (2008) observed newly emerged active region using Solar Optical Telescope (SOT) aboard the *Hinode* satellite (Kosugi et al., 2007). Recently, Otsuji et al. (2010) observed the birth of small scale active region using SOT and Domeless Solar Telescope of Hida Observatory. They found that the emerging magnetic flux expands laterally with the speed of 2.9 km s $^{-1}$  at the surface before further evolution occurred. As time goes on, the flux gradually rise upward at the rate of 2.1 km s $^{-1}$ . Also, using SOT, Iida et al. (2010) measured photospheric magnetic elements in the quiet Sun, finding that the observed cancellation of the elements of both polarities is due to “ $\Omega$ -loop submergence” rather than “U-loop emergence.”

### 1.2.4 Summary of this Section

The followings are a brief summary of this Section.

The birth of active regions is characterized by (1) the separation of the magnetic elements of two polarities (faculae or magneto-patches) and (2) the chromospheric arch filament system (AFS) rising upward with strong downdrafts at its footpoints. (3) In the center of emerging flux region (EFR), the flux continuously emerges, and (4) the magnetic elements of the same polarities gather to make pores. If the flux is sufficient, (5) the pores stream into sunspots, which also separate from each other.

The typical wavelength of the “sea-serpent” fields is consistent with that of Parker instability at the photosphere. Undulating fields are thought to reconnect with each other

and make longer coronal loops that cover the entire active region. Each emergence event occurs in a series of aligned vertical sheets.

## 1.3 Numerical Analyses and Theoretical Modelings of Flux Emergence

### 1.3.1 Flux Emergence and the Dynamo Theory

Active regions are the appearance of emerging flux transported from the deep convection zone. That is, the flux emergence is a part of a global dynamo mechanism in the Sun. The early works on the flux emergence were done in the context of the dynamo theory.

Parker (1955) showed that the horizontal magnetic flux tube is buoyant and will tend to rise (magnetic buoyancy). If we assume pressure  $p$ , density  $\rho$ , and temperature  $T$  of the plasma inside and outside the flux tube, of which the field strength is  $B$ , the force balance at the tube's surface yields

$$p_e = p_i + \frac{B^2}{8\pi}, \quad (1.1)$$

where subscript e and i denote the value outside and inside the tube, respectively. When the plasma is in the thermal equilibrium, namely,  $T_e = T_i = T$ , the above equation can be rewritten as

$$\rho_e = \rho_i + \frac{B^2}{8\pi} \frac{m}{k_B T}, \quad (1.2)$$

where  $m$  is mean molecular mass and  $k_B$  is the Boltzmann constant. Thus, we can see that the flux tube is buoyant ( $\rho_e > \rho_i$ ), and the buoyancy per unit volume is

$$f_B = (\rho_e - \rho_i)g = \frac{B^2}{8\pi} \frac{mg}{k_B T} = \frac{B^2}{8\pi H_p}, \quad (1.3)$$

where  $H_p$  is the local pressure scale height.

Parker (1975) calculated the rising time of the emerging flux tube in the convection zone. He assumed that only aerodynamic drag force counteracts the magnetic buoyancy of the flux tube. For a unit length of the tube of the radius  $a$  (constant), the magnetic buoyancy is

$$F_B = \pi a^2 (\rho_e - \rho_i) g, \quad (1.4)$$

while the aerodynamic drag is

$$F_D = \frac{1}{2} \rho_e V_z a C_D, \quad (1.5)$$

where  $V_z$  and  $C_D$  ( $\sim 3$ ) are the rising velocity of the tube and the drag coefficient, respectively. From these equations, one can calculate the rising speed when it reaches the terminal velocity as

$$V_z = \left( \frac{2\pi a g}{C_D} \frac{\rho_e - \rho_i}{\rho_e} \right)^{\frac{1}{2}} = V_A \left( \frac{\pi a}{C_D H_p} \right)^{\frac{1}{2}}, \quad (1.6)$$

that is, the rising speed is of the order of Alfvén velocity  $V_A = B/(4\pi\rho)$ . According to Parker (1975)'s calculation, the rising time is down to less than a year for a flux tube of 100 G. This value is shorter than the expected time of 10 years, i.e., the solar cycle. That is, there appeared a problem that the flux tube emerges before the field is strengthened enough. It should be noted that the field amplification in the overshoot region (see Section 1.1) was not considered in those days. Rather, the tube was thought to be amplified during its ascent within the convection zone, influenced by the Coriolis effect ( $\alpha\Omega$ -dynamo). To deal with this problem, Schüssler (1977) assumed the conservation of mass and flux together in the calculations. Here, the tube's radius is not a constant but a function of height. As a result, the rising time was found to be about 10 years, which is consistent with the solar cycle.

In his 1979 paper, Schüssler revisited this problem by conducting numerical simulations. He calculated the cross-sectional evolution of rising flux tubes in the convection zone. As the tube rises higher, it expands according to the decreasing of the external density. He found that the rising velocity was consistent with the analytical velocity in Schüssler (1977) as long as the tube does not expand significantly and stays roughly circular. As the tube expands, the relative flow from the apex to the flanks of the tube causes a drastic fragmentation. The cross-sectional shape approaches an “umbrella shape” with an arc-shaped edge, which is similar to large gas bubbles rising through the liquid. Finally, the tube fragments and loses its “identity”.

### 1.3.2 Thin-flux-tube Approximation

The magnetic field at the base of the convection zone has at least  $B_{\text{eq}}$ , where  $B_{\text{eq}}$  is the field strength that is in equipartition with the kinetic energy density of the convective motions:

$$\frac{B_{\text{eq}}^2}{8\pi} = \frac{\rho v_c^2}{2}. \quad (1.7)$$

From the mixing length models for the flow velocity at the bottom  $v_c \sim 10 \text{ m s}^{-1}$  (Stix, 1989),  $B_{\text{eq}}$  is estimated to be  $10^4 \text{ G}$ . Considering the total flux of the active region is ( $10^{20}\text{--}10^{22}$ ) Mx (see Section 1.2), the cross-sectional size of the flux tube at the bottom should be 1000 km, which is much shorter than the local pressure scale height of a few 10,000 km. It should be noted that this approximation is not applicable in the upper convection zone ( $\gtrsim -30 \text{ Mm}$ ) where the diameter of the flux tube exceeds the local pressure scale height (Fan, 2009).

Under the above mentioned assumption, Spruit (1981) introduced the thin-flux-tube (TFT) approximation that the cross-sectional variation of physical quantities is negligible (see also Longcope & Klapper, 1997). Numerical calculations using this model have revealed that flux emergence can explain many observed aspects. Choudhuri & Gilman

(1987) found that the Coriolis force drifts the rising tube poleward and thus the flux tube of  $10^4$  G emerges at high latitudes of the Sun. To overcome the poleward drift, the initial tube requires a field strength of  $10^5$  G (Caligari et al., 1995), which is ten times stronger than the local equipartition field strength. D’Silva & Choudhuri (1993) showed, for the first time, that the Coriolis force explains the active region tilts described by Joy’s law (Hale et al., 1919). Also, TFT calculations have revealed that Coriolis force causes the asymmetries of leading and following spots of bipolar active regions (Fan et al., 1993). One of the most important conclusions obtained from the various TFT simulations is that rising tubes with small magnetic flux (below  $10^{21}$  Mx for  $10^4$  G at the base) cannot reach the photosphere because the apices of the loops lose magnetic fields and subsequently “explode” (Moreno-Insertis et al., 1995). For more detailed discussions, see Fan (2009) and the references therein.

### 1.3.3 Twist Component of the Flux Tube

The TFT approximation does not consider the cross-sectional distortion during the emergence. That is, the cross-section of the flux tube is assumed to be perfectly circular, of which the radius is determined by mass and flux conservations. Parker (1979) insisted that, if the tube has its azimuthal component, i.e., if the tube is twisted, the cross-section keeps its rigidity. Tsinganos (1980) considered hydrodynamic instabilities at the interface between the flux tube and the surrounding plasma, and speculated that the twist reduces instabilities develop.

Longcope et al. (1996) returned to Schüssler (1979)’s situation and calculated the cross-sectional evolution of the rising flux tubes using Boussinesq magnetohydrodynamic (MHD) equations. He found that, when the tube has no or slight twist, it is fragmented into two counter-rotating elements moving apart horizontally from each other. Eventually, the tube stops rising. In Longcope & Klapper (1997), thin-flux-tube equations including twist component were introduced. Moreno-Insertis & Emonet (1996) and Emonet & Moreno-

Insertis (1998) confirmed that the azimuthal component of the flux tube keeps its shape, and the tube approaches the terminal velocity when the aerodynamic drag counteracts the buoyancy. They also investigated the parameter study on the twist strength: the tube becomes more fragmented as the twist decreases.

### 1.3.4 Emergence from the Surface to the Corona

As for the flux emergence above the surface, the pioneering work was done by Shibata et al. (1989), who performed two-dimensional magnetohydrodynamic (MHD) simulations of flux emergence through the undular mode of magnetic buoyancy instability ( $\mathbf{k} \parallel \mathbf{B}$ , where  $\mathbf{k}$  and  $\mathbf{B}$  denote the wavenumber and the initial magnetic field vector, respectively; the Parker instability) to reproduce some dynamical features such as the rise motion of an arch filament system and downflows along the magnetic field lines (see Figure 1.9). Since then, the evolution of an emerging flux and the interaction with pre-existing coronal fields have been studied by various two- and three-dimensional simulations. Nozawa et al. (1992) performed the emergence from the convectively unstable solar interior (the convective-Parker instability), while Yokoyama & Shibata (1995) studied the reconnection between the expanding loop and the pre-existing fields in the corona and the subsequent formation of X-ray jets. Three-dimensional calculations by Matsumoto & Shibata (1992) and Matsumoto et al. (1993) were performed for studies of the interchange ( $\mathbf{k} \perp \mathbf{B}$ ) and quasi-interchange ( $\mathbf{k} \parallel \mathbf{B}$  with  $kH_{\text{ph}} \ll 1$ , where  $H_{\text{ph}}$  is the photospheric pressure scale height) mode instabilities. Magara (2001) studied the emergence of the magnetic flux tube from the convection zone by means of 2.5-dimensional MHD simulations focused on the cross-section of the tube (see Figure 1.10). He found the deceleration of the rising flux tube due to the convectively stable photosphere and the subsequent horizontal outflow. To rise further above the surface, the tube requires a stronger field. Matsumoto et al. (1998) performed 3D simulations of the buoyant emergence of the strongly-twisted flux tube (see Figure 1.11). Because of the kink instability, the rising

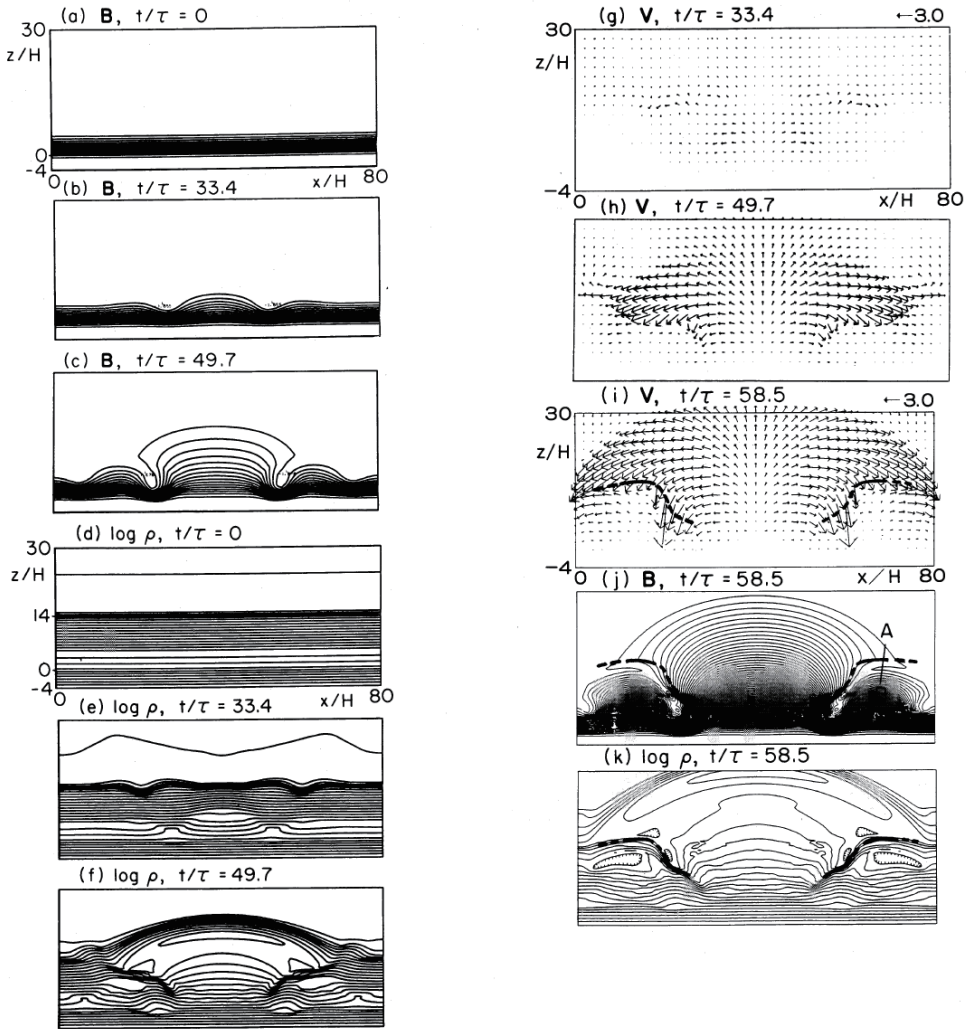


Figure 1.9: Time evolution of two-dimensional model of emerging magnetic flux from the photosphere due to the Parker instability (Shibata et al., 1989). Figures show magnetic field lines, density, and velocity fields. The isolated flux shows a self-similar expansion into the atmosphere, forming arch filament system with strong downdrafts near the photospheric pores.

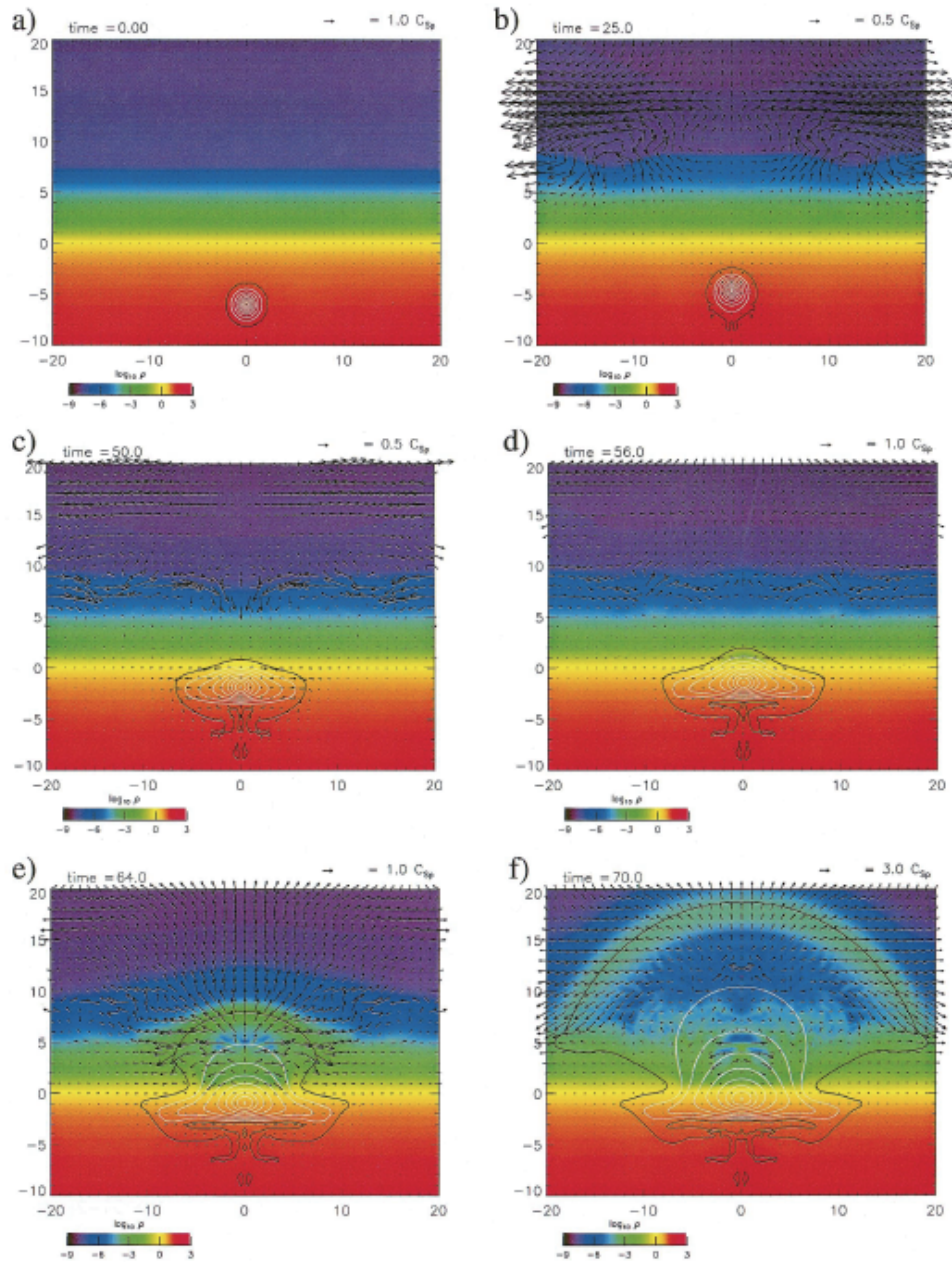


Figure 1.10: Numerical results by Magara (2001). Shown are the time-evolution of gas density (a color map), the magnetic field lines (white contours lines), the tube boundary (a black contour line), and the velocity field (arrows), respectively.

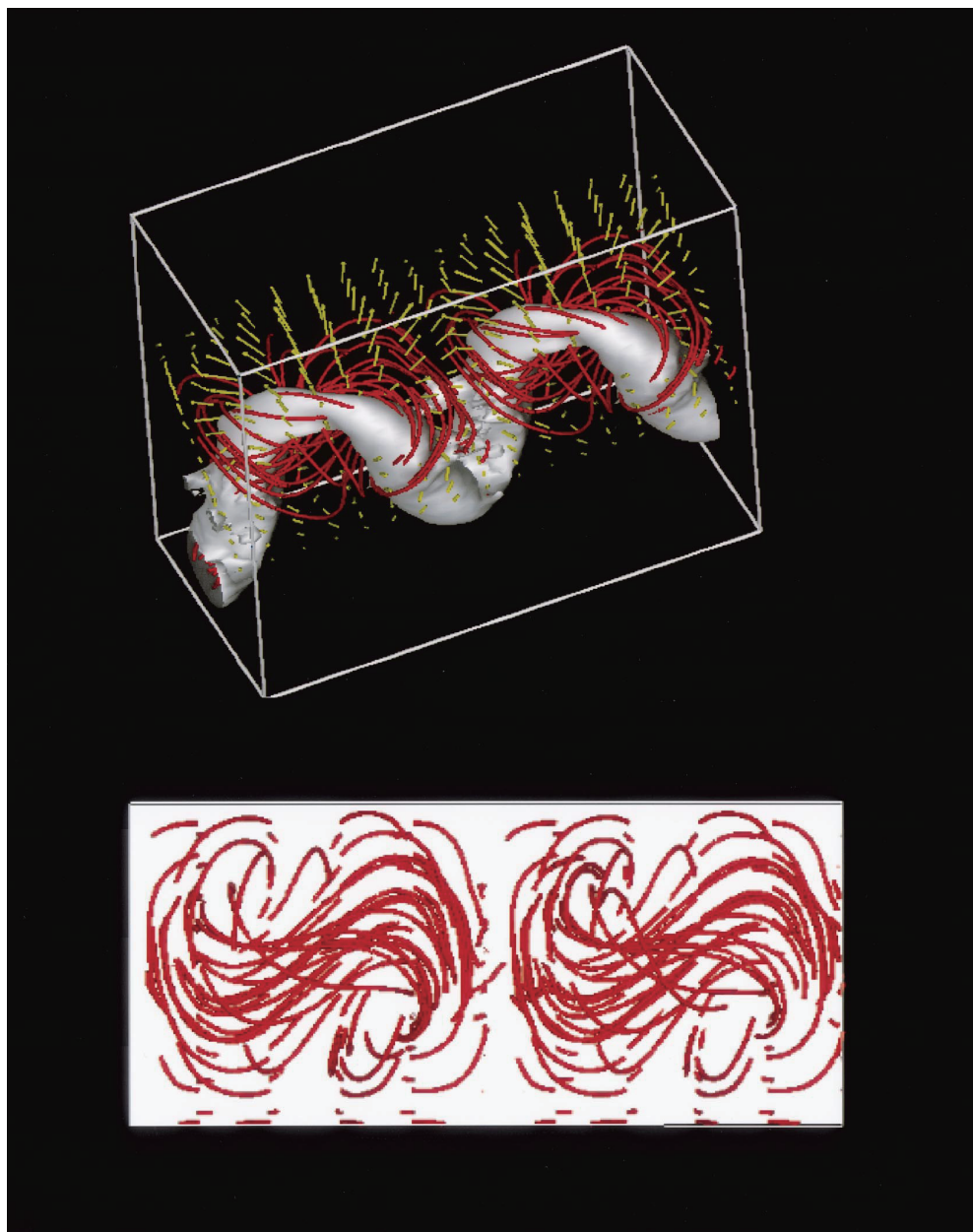


Figure 1.11: (*Top*) 3D view of the kink-unstable flux tube. Red curves show magnetic field lines, the gray surface shows isosurface of field strength, and green arrows are velocity vectors. (*Bottom*) The projection of field lines onto the horizontal plane. Both images are from Matsumoto et al. (1998)

portions of the tube become deformed into a helical shape and emerge into the corona. They suggested that an observed sequence of active regions is a result of emergence of such a twisted tube.

Fan (2001) compared her three-dimensional simulation results with observed features of a newly emerged active region by Strous et al. (1996). Figure 1.12 shows the numerical results of Fan (2001). Here, the initial flux tube embedded at the depth of  $-1500$  km

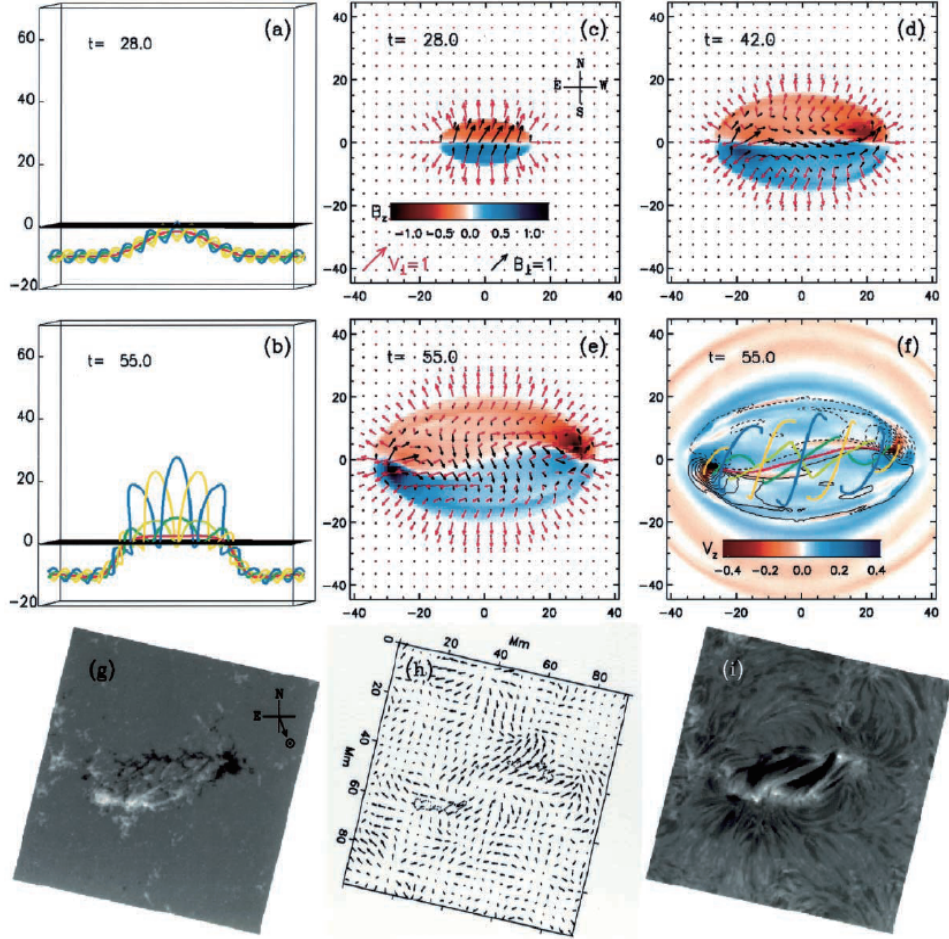


Figure 1.12: Numerical results by Fan (2001). (a,b) Snapshots of the evolution of selected field lines. (c-e) Evolution of the vertical magnetic field  $B_z$ , the horizontal (or transverse) field (black arrows), and the horizontal velocity field (red arrows) on the photosphere, respectively. (f) Same set of field lines as shown in (b), but projected onto the photosphere overlying the vertical velocity field  $V_z$ , and the contours of  $B_z$  (solid contours represent positive  $B_z$ ). (g-i) Line-of-sight magnetogram, the horizontal velocity field, and the H $\alpha$  image of NOAA AR 5617 (Strous et al., 1996), respectively.

emerges into the corona. The vertical magnetic field at the photosphere shows a pair of magnetic elements (Figures 1.12(c)-(e)). Figure 1.12(f) is the top-view of the selected field lines. These are well similar to the active region observation in Figures 1.12(g)-(i). Magara & Longcope (2001) reproduced a sigmoid structure of an emerging tube by conducting 3D experiment. Archontis et al. (2004) performed three-dimensional simulations using the criterion by Acheson (1979) to analyze the magnetic buoyancy instability within the photosphere/chromosphere, while Murray et al. (2006) did parameter studies on the dependence of the initial field strength of the tube and its twist, finding that the tube evolves in the self-similar way when varying the field strength, and that the magnetic buoyancy instability for further evolution do not occur when the field or the twist is too weak.

Linear stability analysis of magnetic buoyancy instabilities in a sheared magnetic layer was done by Hanawa et al. (1992), while the nonlinear process was studied in 2D simulation by Kusano et al. (1998) and in 3D by Nozawa (2005).

Isobe et al. (2007) studied the resistive process of magnetic flux emergence and its relation to Ellerman bombs, which is suggested by Pariat et al. (2004). Due to the Parker instability, the photospheric fields have an undulatory shape of the wave length  $10H_{\text{ph}} - 20H_{\text{ph}}$  and gradually reconnect with each other to make longer coronal fields. Archontis & Hood (2009) did three-dimensional calculation that the initial flux sheet makes “sea-serpent” fields.

Recently, interaction between flux emergence and the convection has been widely investigated. For instance, Cheung et al. (2008) found that the numerical modeling of emerging flux regions by three-dimensional radiative MHD simulations exhibits photospheric characteristics that are comparable with the observations from the *Hinode*/SOT. Cheung et al. (2010) modeled the rise of an axisymmetric, twisted flux tube with the shape of a semitorus and reproduced a pair of sunspots (Figure 1.13). In this calculation, the rising flux extends sideways beneath the photosphere to make a pancake-like structures. Also, convective flows were found to make undulating photospheric fields that eventually

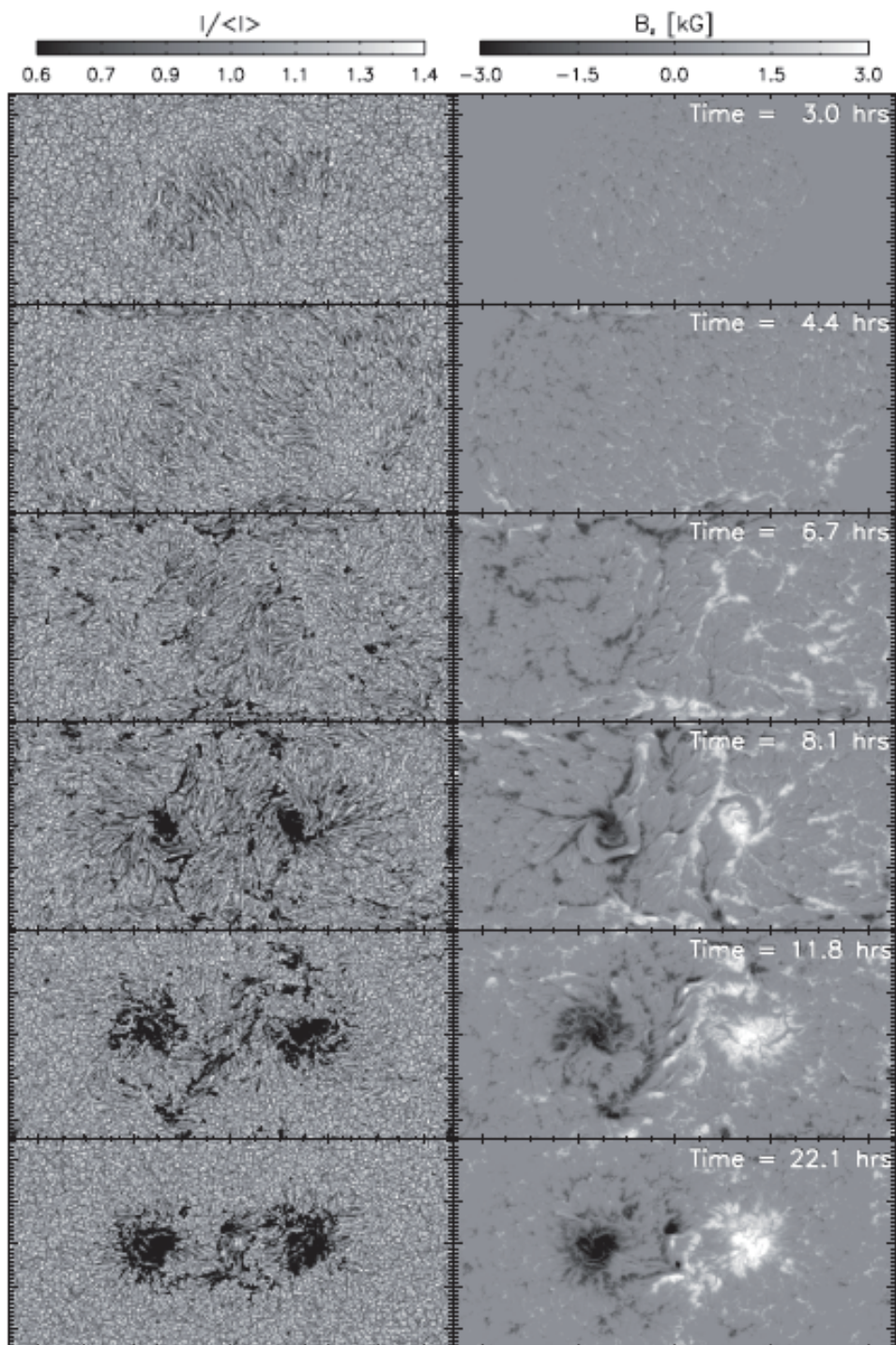


Figure 1.13: Time-evolution of the numerical results by Cheung et al. (2010). The continuum intensity at 500 nm (left) and synthetic longitudinal magnetograms (right). The full horizontal extent of the simulation domain ( $92 \text{ Mm} \times 49 \text{ Mm}$ ) is shown.

reconnect, which leads to the cancellation of opposite polarity fields at the surface (Iida et al., 2010).

### 1.3.5 Summary of this Section

Magnetic flux tube tends to rise through the solar convection zone by its magnetic buoyancy, feeling the aerodynamic drag. From the various thin-flux-tube studies, the tube of  $10^5$  G is required at the bottom of the convective layer in order to explain the emergence latitude, active region tilts, asymmetries of the two polarities, and the coherent emergence without “explosion”, etc. If the tube has no azimuthal component, it would be deformed into “umbrella shape” with counter-rotating two vortices moving apart from each other. Eventually, the flux tube stops rising.

A number of numerical calculations that the photospheric flux rises into the atmosphere due to the magnetic buoyancy instability well explain the observational characteristics such as the formation of AFS, strong downdrafts at the footpoints, and the resistive emergence process.

## 1.4 Purpose of the Thesis

As introduced above in Section 1.3, many authors have modeled the emergence of magnetic flux by using numerical calculations. However, the previous models have been separated into two groups. One is for the emergence within the interior such as thin-flux-tube (TFT) studies. However, the TFT approximation neglects the cross-sectional evolution and is not applicable at the top of the interior ( $\gtrsim (-20 \sim -30)$  Mm) because, in this area, the tube is no longer thin. The other group is related to the numerical studies from the surface to the upper atmosphere. For this, the initial flux is located just beneath the photosphere ( $\sim -2000$  km). So far as the author know, no previous study has investigated the emergence treating the convection zone the photosphere/chromosphere, and the corona as a consistent process. Abbott & Fisher (2003) calculated a flux emergence by

connecting the anelastic MHD convective layer and the fully compressible MHD solar atmosphere from the photosphere to the low corona. However, their full MHD atmosphere did not include the upper convection zone. To investigate the detailed behavior of the emerging flux from the convection zone to the atmosphere, especially on the dynamics near the surface, we have to deal with the full MHD numerical box including the convective layer, the photosphere/chromosphere, and the corona.

The aim of this Thesis is to study the flux emergence from much deeper interior, i.e., the emergence in a larger scale, and the resulting formation of active regions by means of two- and three-dimensional MHD calculations. In these experiments, we model the flux emergence from the interior at a depth of  $-20,000$  km, where the TFT and anelastic approximation becomes inappropriate. (The emergence from the base of the convective layer is beyond the computational ability; see Appendix B.1.) And we evaluate the physical quantities of the magnetic flux for creating actual active regions, such as the field strength, the total flux, and the twist strength at that depth. Also, we perform shallow 3D calculations to investigate the dependence of the magnetic energy of active regions on the twist intensity of the initial flux tubes.

The rest of the Thesis proceeds as follows. First, in Chapter 2, we show the basic equations of the magnetohydrodynamics (MHD) for the numerical calculations in this Thesis. We detail the two-dimensional calculations in Chapter 3 (undular evolution) and Chapter 4 (cross-sectional evolution), while, in Chapter 5, we mention the three-dimensional calculation. The shallow 3D experiments on the twist intensity are introduced in Chapter 6. Finally, in Chapter 7 and in Chapter 8, we will present summary and discussion, respectively.



# Chapter 2

## Basic Equations

In numerical simulations in this Thesis, we solve nonlinear, time-dependent, compressible MHD equations. We take a rectangular computation box with three-dimensional Cartesian coordinates  $(x, y, z)$ , where the  $z$ -coordinate increases upward. In Chapter 3 and Chapter 4, we use two-dimensional domains  $(x, z)$  and  $(y, z)$ , and the variation of the physical quantities is assumed constant along  $y$  and  $x$  axis, respectively.

The medium is assumed to be an inviscid perfect gas with a specific heat ratio  $\gamma = 5/3$ .

The basic equations in vector form are as follows:

$$\frac{\partial \rho}{\partial t} + \nabla \cdot (\rho \mathbf{V}) = 0, \quad (2.1)$$

$$\frac{\partial}{\partial t}(\rho \mathbf{V}) + \nabla \cdot \left( \rho \mathbf{V} \mathbf{V} + p \mathbf{I} - \frac{\mathbf{B} \mathbf{B}}{4\pi} + \frac{\mathbf{B}^2}{8\pi} \mathbf{I} \right) - \rho \mathbf{g} = 0, \quad (2.2)$$

$$\frac{\partial \mathbf{B}}{\partial t} = \nabla \times (\mathbf{V} \times \mathbf{B}), \quad (2.3)$$

$$\begin{aligned} & \frac{\partial}{\partial t} \left( \rho U + \frac{1}{2} \rho \mathbf{V}^2 + \frac{\mathbf{B}^2}{8\pi} \right) \\ & + \nabla \cdot \left[ \left( \rho U + p + \frac{1}{2} \rho \mathbf{V}^2 \right) \mathbf{V} + \frac{c}{4\pi} \mathbf{E} \times \mathbf{B} \right] - \rho \mathbf{g} \cdot \mathbf{V} = 0, \end{aligned} \quad (2.4)$$

and

$$U = \frac{1}{\gamma - 1} \frac{p}{\rho}, \quad (2.5)$$

$$\mathbf{E} = -\frac{1}{c} \mathbf{V} \times \mathbf{B}, \quad (2.6)$$

$$p = \frac{k_B}{m} \rho T, \quad (2.7)$$

where  $U$  is the internal energy per unit mass,  $\mathbf{I}$  the unit tensor,  $k_B$  the Boltzmann constant,  $m$  the mean molecular mass, and  $\mathbf{g} = (0, 0, -g_0)$  the uniform gravitational acceleration. Other symbols have their usual meanings:  $\rho$  is for density,  $\mathbf{V}$  velocity vector,  $p$  pressure,  $\mathbf{B}$  magnetic field,  $c$  speed of light,  $\mathbf{E}$  electric field, and  $T$  temperature. Here, the Coriolis effect is neglected (see Appendix B.2).

To make above equations dimensionless, we introduce normalizing units of length  $H_0$ , velocity  $C_{s0}$ , time  $\tau_0 \equiv H_0/C_{s0}$ , and density  $\rho_0$ , where  $H_0 = k_B T_0 / (mg_0)$  is the pressure scale height,  $C_{s0}$  the sound speed, and  $\rho_0$  the density at the photosphere, respectively. The gas pressure, temperature, and magnetic field strength, are normalized by the combinations of the units above, i.e.,  $p_0 = \rho_0 C_{s0}^2$ ,  $T_0 = m C_{s0}^2 / (\gamma k_B)$ , and  $B_0 = (\rho_0 C_{s0}^2)^{1/2}$ , respectively. The gravity is given as  $g_0 = C_{s0}^2 / (\gamma H_0)$  by definition. For comparison of numerical results with observations, we use  $H_0 = 200$  km,  $C_{s0} = 8$  km s<sup>-1</sup>,  $\tau_0 = H_0/C_{s0} = 25$  s, and  $\rho_0 = 1.4 \times 10^{-7}$  g cm<sup>-3</sup>, which are typical values for the solar photosphere. Then,  $p_0 = 9.0 \times 10^4$  dyn cm<sup>-2</sup>,  $T_0 = 4000$  K, and  $B_0 = 300$  G. Note that the normalizing units are arranged in Chapter 6.

For all calculations throughout the Thesis, we use the modified Lax-Wendroff scheme version of the CANS (Coordinated Astronomical Numerical Software) code maintained by Yokoyama et al.<sup>1</sup>

---

<sup>1</sup>CANS (Coordinated Astronomical Numerical Software) is available online at:  
<http://www-space.eps.s.u-tokyo.ac.jp/~yokoyama/etc/cans/>



# Chapter 3

## Two-dimensional Experiment: Undular Evolution

### 3.1 Introduction

One aim of the Thesis is to investigate the emergence of the magnetic flux tube from the deep convection zone ( $-20,000$  km). First, we perform two-dimensional calculations in this Chapter and in Chapter 4, in which two modes of the emergence are considered; one regards to the profile along the main axis of the tube (the undular evolution) and the other is the time-development of the cross-section (the cross-sectional evolution).

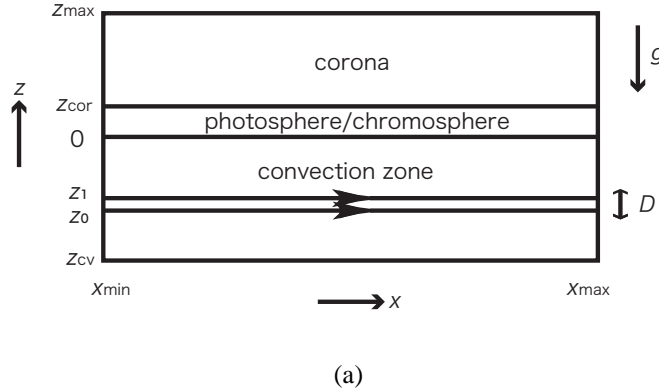
In this Chapter, we investigate the undulatory evolution that the initial flux undergoes the Parker instability (see Appendix A) within the adiabatically stratified convection zone and rise into the corona.

### 3.2 Numerical Model

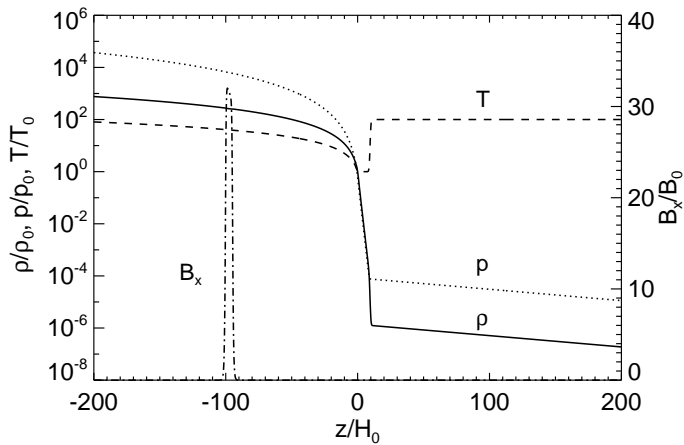
We consider an isolated magnetic flux sheet, located in a convectively marginally stable gas layer in a two-dimensional Cartesian coordinate system  $(x, z)$ , where the  $z$ -direction is antiparallel to the gravitational acceleration. We solve adiabatic two-dimensional ( $\partial/\partial y =$

$0, B_y = 0, V_y = 0$ ) MHD equations (see Chapter 2).

The initial hydrostatic gas layer is composed of three regions: hot and cold isothermal layers in upper and middle regions represent a simplified model of the solar corona and the photosphere/chromosphere, and a non-isothermal layer in the lower region models the convection zone (see Figure 3.1(a)). We take  $z = 0$  to be the base height of the



(a)



(b)

Figure 3.1: (a) Schematic illustration of the initial condition. (b) One-dimensional  $z$ -distributions of the initial density (solid line), pressure (dotted line), temperature (dashed line), and the field strength (dash-dotted line).

photosphere.

The initial temperature distribution of the photosphere/chromosphere and the corona

$(z \geq 0)$  is assumed to be

$$T(z) = T_{\text{ph}} + \frac{1}{2}(T_{\text{cor}} - T_{\text{ph}}) \{\tanh [(z - z_{\text{cor}})/w_{\text{tr}}] + 1\}, \quad (3.1)$$

where  $T_{\text{cor}}$  and  $T_{\text{ph}}$  are the respective temperatures in the corona and in the photosphere/chromosphere,  $z_{\text{cor}}$  the height of the base of the corona, and  $w_{\text{tr}}$  the temperature scale height of the transition region, respectively. We take  $T_{\text{cor}} = 100T_0$ ,  $T_{\text{ph}} = T_0$ ,  $z_{\text{cor}} = 10H_0$ , and  $w_{\text{tr}} = 0.5H_0$ . For the initial temperature distribution in the convective layer ( $z \leq 0$ ), we assume

$$T(z) = T_{\text{ph}} - \alpha z \left| \frac{dT}{dz} \right|_{\text{ad}}, \quad (3.2)$$

where

$$\left| \frac{dT}{dz} \right|_{\text{ad}} = \frac{\gamma - 1}{\gamma} \frac{mg_0}{k_B} \quad (3.3)$$

is the adiabatic temperature gradient, and  $\alpha$  is a parameter of the temperature gradient of the convection zone. In our calculations,  $\alpha$  is set to be unity, i.e., the initial temperature distribution in the interior is adiabatic.

The magnetic field is initially horizontal,  $\mathbf{B} = (B_x(z), 0, 0)$ , and is embedded in the convection zone. The distribution of magnetic field strength is given by

$$B_x(z) = [8\pi p(z)/\beta(z)]^{1/2}, \quad (3.4)$$

where

$$\beta(z) = \beta_*/f(z), \quad (3.5)$$

and

$$f(z) = \frac{1}{4} \left[ \tanh\left(\frac{z - z_0}{w_0}\right) + 1 \right] \left[ -\tanh\left(\frac{z - z_1}{w_1}\right) + 1 \right]. \quad (3.6)$$

Here,  $\beta_*$  is the ratio of gas pressure to magnetic pressure at the center of the magnetic flux sheet, and  $z_0$  and  $z_1 = z_0 + D$  are the heights of the lower and upper boundaries of the flux sheet, respectively, where  $D$  is the vertical thickness of the sheet. We use  $z_0 = -100H_0 \simeq -20,000$  km. In all of our calculations,  $w_0$  and  $w_1$  are set to be  $0.5H_0$ . We take  $\beta_* = 160$  and  $D = 5H_0 = 1000$  km for case 1 (the typical model), so as the initial magnetic field strength  $B_x$  to be  $10^4$  G and the total magnetic flux  $\Phi$  to be  $10^{21}$  Mx. To calculate the total magnetic flux, we regard the initial flux sheet as a rectangular prism with a base  $D$  (in the  $z$ -direction) by  $10D$  (in the  $y$ -direction).

On the basis of the initial plasma  $\beta$  distribution mentioned above, the initial density and pressure distribution are calculated numerically by using the equation of static pressure balance:

$$\frac{d}{dz} \left[ p + \frac{B_x^2}{8\pi} \right] + \rho g_0 = 0. \quad (3.7)$$

The initial temperature, density, pressure, and field strength distributions for the typical case are shown in Figure 3.1(b).

In order to trigger the Parker instability (Parker (1966), see also Appendix A) in the convection zone, small density perturbation of the form

$$\delta\rho = Af(z)\rho(x, z) \cos(2\pi x/\lambda) \quad (3.8)$$

is initially reduced from the magnetic flux sheet ( $z_0 \leq z \leq z_1$ ) within the finite horizontal domain ( $-3\lambda/4 < x < 3\lambda/4$ ), where  $\lambda (= 400H_0)$  is the perturbation wavelength, and  $A (= 0.01)$  is the maximum value of the initial density reduction.

The domain of the simulation box is ( $x_{\min} < x < x_{\max}$ ) and ( $z_{\min} < z < z_{\max}$ ), where

$x_{\min} = -400H_0$ ,  $x_{\max} = 400H_0$ ,  $z_{\min} = -200H_0$ ,  $z_{\max} = 200H_0$ , i.e., the total size of the box is  $160 \text{ Mm} \times 80 \text{ Mm}$ . This is much larger than those of the calculations focusing on the emergence from the uppermost convection zone to the corona (e.g. Shibata et al., 1989, etc.). Periodic boundaries are assumed for  $x = x_{\min}$  and  $x = x_{\max}$ , symmetric boundaries for  $z = z_{\min}$  and  $z = z_{\max}$ . A damping zone is attached near the top boundary to reduce the effects of reflected waves. For the typical model (case 1), the total number of grid points is  $(N_x \times N_z) = (1536 \times 1920)$ , and the mesh sizes are  $\Delta x = 0.52H_0$  and  $\Delta z = 0.21H_0$ , both of which are uniform.

For comparison, we also calculate other cases with different values of the parameters. We vary the values of the initial field strength  $B_x$  and of the total flux  $\Phi$  of the flux sheet by adjusting  $\beta_*$  and  $D$ . In these calculations, we set the total number of grid points  $(N_x \times N_z) = (1024 \times 1280)$ , and the uniform mesh sizes  $\Delta x = 0.78H_0$  and  $\Delta z = 0.31H_0$ . The cases we examine are summarized in Table 3.1.

Table 3.1: Summary of Cases

Case	$B_x$ (G) <sup>a</sup>	$\Phi$ (Mx) <sup>b</sup>	$\beta_*$ <sup>c</sup>	$D$ (km) <sup>d</sup>	$N_x \times N_z$ <sup>e</sup>
1	$1.0 \times 10^4$	$1.0 \times 10^{21}$	$1.6 \times 10^2$	1000	$1536 \times 1920$
2	$8.1 \times 10^4$	$9.8 \times 10^{23}$	$1.1 \times 10^{-1}$	11,000	$1024 \times 1280$
3	$1.0 \times 10^5$	$1.0 \times 10^{23}$	$2.0 \times 10^{-1}$	3000	$1024 \times 1280$
4	$1.1 \times 10^5$	$1.0 \times 10^{22}$	$2.0 \times 10^{-1}$	840	$1024 \times 1280$
5	$1.1 \times 10^5$	$1.1 \times 10^{21}$	$2.0 \times 10^{-1}$	200	$1024 \times 1280$
6	$1.1 \times 10^4$	$1.1 \times 10^{23}$	$2.2 \times 10^2$	11,400	$1024 \times 1280$
7	$1.0 \times 10^4$	$1.0 \times 10^{22}$	$1.6 \times 10^2$	3200	$1024 \times 1280$
8	$8.9 \times 10^3$	$1.0 \times 10^{20}$	$1.5 \times 10^2$	260	$1024 \times 1280$
9	$1.1 \times 10^3$	$1.0 \times 10^{21}$	$2.2 \times 10^4$	11,000	$1024 \times 1280$
10	$1.0 \times 10^3$	$1.0 \times 10^{21}$	$1.6 \times 10^4$	3200	$1024 \times 1280$
11	$9.9 \times 10^2$	$1.1 \times 10^{20}$	$1.5 \times 10^4$	1000	$1024 \times 1280$
12	$1.0 \times 10^2$	$1.0 \times 10^{21}$	$2.5 \times 10^6$	11,400	$1024 \times 1280$
13	$1.1 \times 10^2$	$1.0 \times 10^{20}$	$1.4 \times 10^6$	3200	$1024 \times 1280$
14	$1.0 \times 10^2$	$1.0 \times 10^{19}$	$1.4 \times 10^6$	960	$1024 \times 1280$

<sup>a</sup>Initial field strength.

<sup>b</sup>Total magnetic flux.

<sup>c</sup>Plasma beta at the sheet center.

<sup>d</sup>Width of the sheet.

<sup>e</sup>Total grid points.

### 3.3 General Evolution

In this Section, we show the numerical results of the typical case (case 1:  $B_x = 10^4$  G and  $\Phi = 10^{21}$  Mx); the results display the “two-step emergence.” Figure 3.2 illustrates the development of the density profile with magnetic field velocity vectors, while Figure 3.3 indicates the height of the apex of the magnetic field  $z_{\text{apex}}$  and its rise velocity  $V_{z\text{apex}}$ .

The time evolution can be divided into four stages according to the rise velocity at the apex of the emerging field. In the first stage ( $0 < t/\tau_0 < 700$ ), the magnetic flux begins an emergence in the convection zone due to the Parker instability driven by the magnetic buoyancy (Figure 3.2(b)). The rise velocity increases continuously in this stage (Figure 3.3). The second stage ( $700 < t/\tau_0 < 1900$ ) is characterized by a gradual deceleration (Figure 3.3) because the arch-like emerging field becomes deformed to horizontal so that the mass on the apex can no longer fall down along the field lines, and thus continues to pile up on the horizontal field. As a consequence, the emerging flux stretches around the solar surface (Figures 3.2(c) and (d)). In the third stage ( $1900 < t/\tau_0 < 2000$ ), the top part of the emerging magnetic flux almost stops at the surface while fluxes are still emerging from below, that is, the magnetic pressure gradient on the upper boundary of the flux sheet continues to enhance. When the magnetic pressure gradient gets steepened enough, the Parker instability sets in and drives the further evolution into the upper atmosphere (Figures 3.2(e) and (f)). In the final, fourth stage ( $t/\tau_0 > 2000$ ), the magnetic flux evolves to the corona due to magnetic pressure, which is consistent with the results of classical calculations (e.g. Shibata et al., 1989) (Figures 3.2(g) and (h)). In the following, we will discuss each stage in more detail, and examine the dynamical structure of the expanding loop and the related forces acting on the magnetic field.

#### 3.3.1 First Stage ( $0 < t/\tau_0 < 700$ )

The initial sinusoidal perturbation in the flux sheet triggers the Parker instability so that the flux sheet begins to rise through the convection zone by magnetic buoyancy (Figure

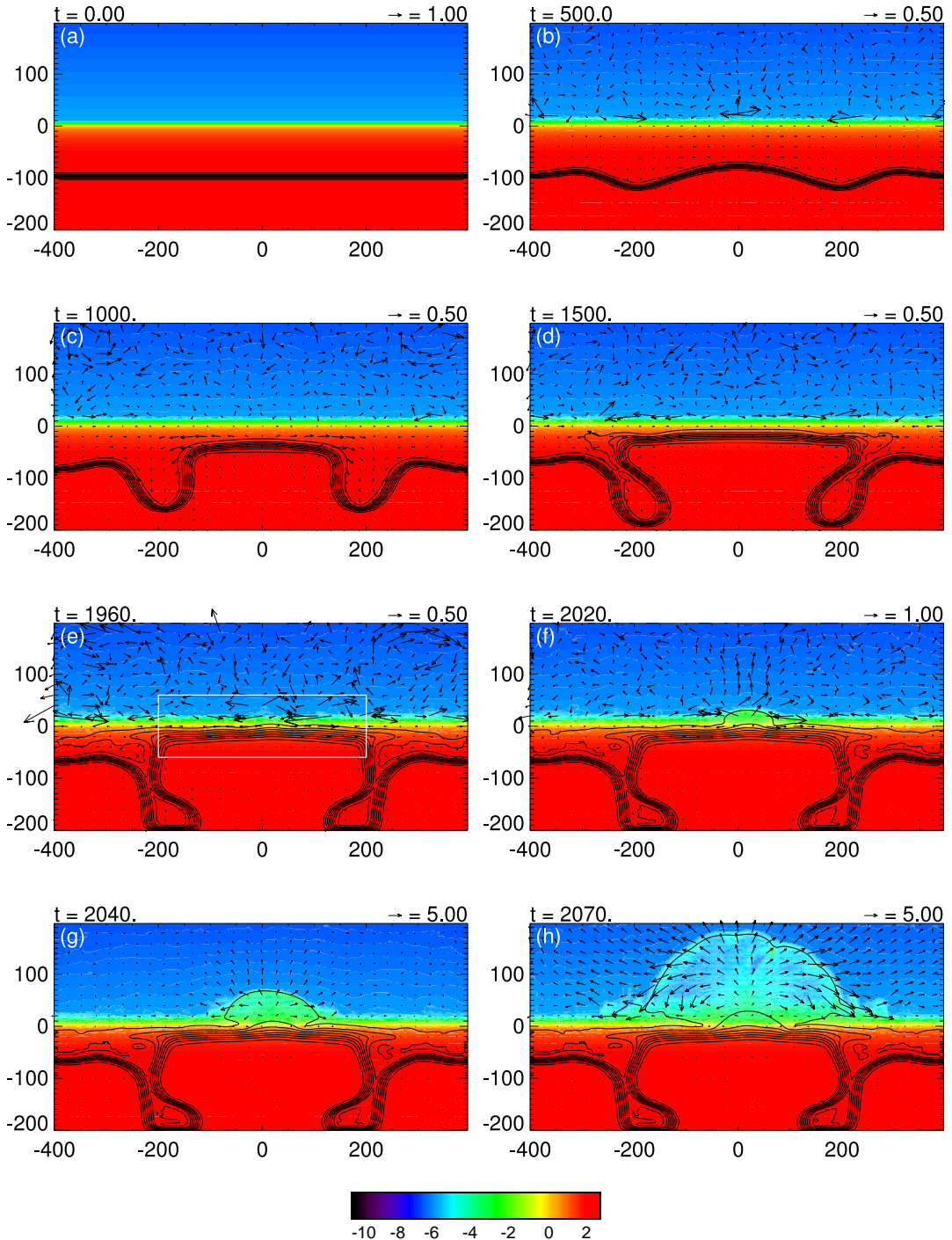


Figure 3.2: Time-evolution of the “two-step emergence” for case 1 (typical model). (a)  $t/\tau_0 = 0$ ; (b)  $t/\tau_0 = 500$ ; (c)  $t/\tau_0 = 1000$ ; (d)  $t/\tau_0 = 1500$ ; (e)  $t/\tau_0 = 1960$ ; (f)  $t/\tau_0 = 2020$ ; (g)  $t/\tau_0 = 2040$ ; (h)  $t/\tau_0 = 2070$ . Logarithmic density profiles ( $\log_{10}(\rho/\rho_0)$ ) are indicated by color contour, while magnetic field lines and velocity vectors are overplotted with black lines and arrows. The white box at  $t/\tau_0 = 1960$  shows the area we analyze the Parker instability (see Fig. 3.8).

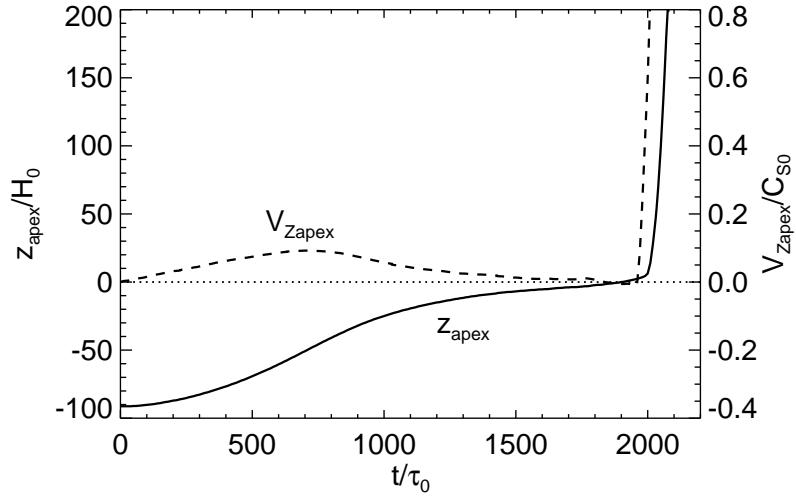


Figure 3.3: Time evolution of the apex of the flux sheet; solid line is a height of the apex, whose rise velocity is indicated with dashed line. Photospheric level ( $z/H_0 = 0$ ) is overplotted with dotted line.

3.2(b)). In this phase, the rise speed enhances continuously as the flux sheet emerges. The rising flux becomes arch-like shape owing to the stronger buoyancy of the loop center. The evacuation in the apex by the downflow along the field lines due to gravity leads to the acceleration of the loop until reaching the local Alfvén speed ( $C_A = B/\sqrt{4\pi\rho}$ ). Figure 3.4 is a close-up view of the evolution between  $t/\tau_0 = 400$  and  $t/\tau_0 = 600$  of Figure 3.3, where a dashed line indicates the rise velocity of the apex, while the local Alfvén speed is represented by a solid line. This figure shows that the rise velocity increases so as to get close to the local Alfvén speed.

### 3.3.2 Second Stage ( $700 < t/\tau_0 < 1900$ )

At around  $t/\tau_0 = 700$ , the rise velocity changes from acceleration to deceleration (Figure 3.3), and at  $t/\tau_0 = 1000$ , both legs of the loop become vertical (Figure 3.2(c)). The central part of the emerging loop flattens and expands horizontally along the surface. Drained gas from the apex flows down along the field lines to each trough, so that the both troughs sink into the deep convection zone.

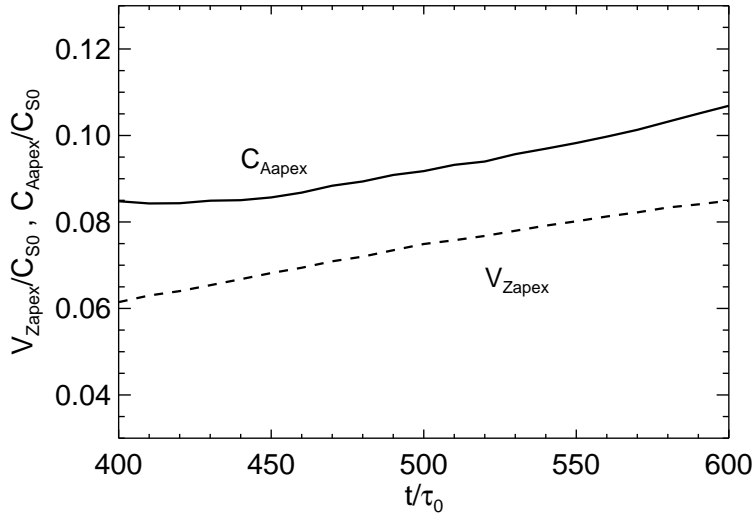


Figure 3.4: The close-up view of Figure 3.3. Upward velocity at the apex of the loop is plotted by a dashed line, while the local Alfvén speed is represented by a solid line.

In this stage, the rise motion turns into the deceleration as seen from Figure 3.3. Magara (2001) found that the tube reduces its rise speed and becomes flattened since the rise motion cannot persist through the convectively stable photosphere. Murray et al. (2006) explained that the deceleration process occurs because the downward pressure gradient exceeds the upward magnetic buoyancy when the emerging flux tube is close enough to the surface. In addition, Murray et al. (2006) found a period when the rise speed diminishes due to the aerodynamic drag exerted by the flows surrounding the tube while in the convection zone. In our case, however, the deceleration occurs at much deeper level ( $z \sim -50H_0 = -10,000$  km) than the previous studies ( $z \sim -850$  km). Moreover, our simulation is carried out in a two-dimensional scheme, while the previous studies were done in 2.5D or 3D, so that a three-dimensional force such as the aerodynamic drag does not exert on our emerging loop. Our results are explained by another mechanism as follows.

Figure 3.5 shows the distribution of the density difference from the initial state ( $\Delta\rho \equiv \rho(t) - \rho(0)$ ) and the horizontal component of the magnetic field ( $B_x$ ) along the  $z$ -axis at  $t/\tau_0 = 600$ ,  $t/\tau_0 = 1000$ , and  $t/\tau_0 = 1960$ . As can be seen in Figure 3.5, the mass

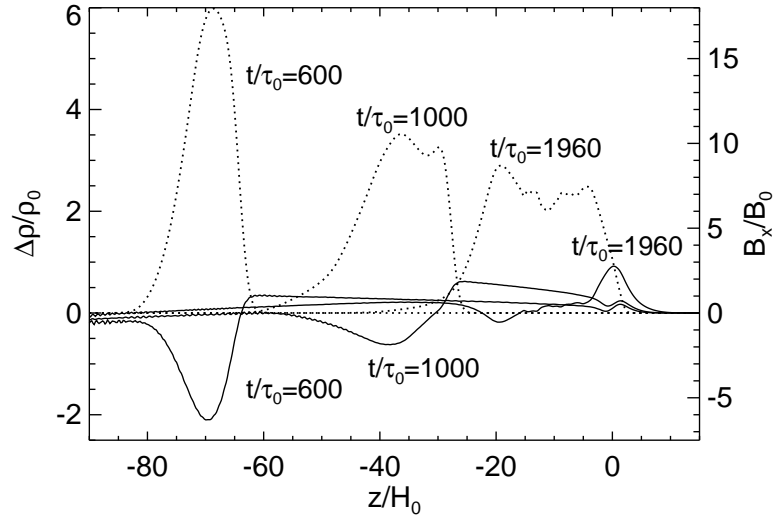


Figure 3.5: Density differences from the initial state ( $\Delta\rho \equiv \rho(t) - \rho(0)$ , solid lines) and horizontal field components ( $B_x$ , dotted lines) along the  $z$ -axis at the center of the simulation box ( $x/H_0 = 0$ ) at the three different times. As the magnetic flux rises, mass piles up on the loop. However, the mass cannot persist through the isothermal photosphere ( $0 < z/H_0 < 10$ ).

piled on the emerging loop cannot rise through the photosphere/chromosphere ranging from  $z/H_0 = 0$  to  $z/H_0 = 10$  because this isothermal (i.e. strongly sub-adiabatic) layer is convectively stable. Figure 3.6(a) shows the vertical component of the forces acting upon the apex of the loop. They are gas pressure gradient  $-\nabla p = -dp/dz$ , gravity  $\rho g_0$ , magnetic pressure gradient  $-\nabla p_{\text{mag}} = -d[B^2/(8\pi)]/dz$ , and magnetic tension  $t_{\text{mag}} = [(\mathbf{B} \cdot \nabla) \mathbf{B}]_z/(4\pi)$ . Figure 3.6(b) shows the acceleration calculated by dividing the total force with the gas density ( $F_z/\rho = (-\nabla p - \rho g_0 - \nabla p_{\text{mag}} - t_{\text{mag}})/\rho$ ). It should be noted that the total force  $F_z$  is much smaller than each force since the rising loop is almost in a mechanical equilibrium. Figure 3.6(b) indicates that the acceleration turns from positive to negative at around  $t/\tau_0 = 870$ , which means the rise velocity changes into deceleration phase at that time.

The deceleration of the crest and the continuous rise motion of the both sides cause the loop flattened, which, in turn, makes the mass left on the flattened loop. As a result, the rising flux decelerates and stretches horizontally beneath and around the surface. This

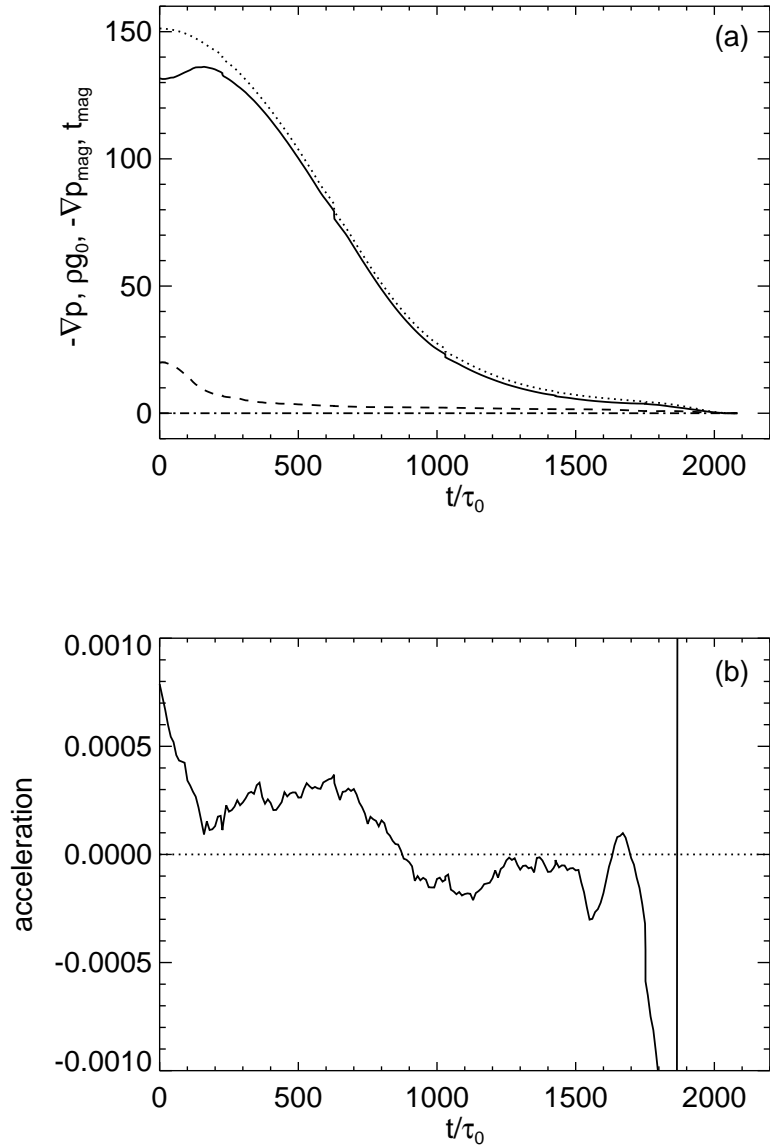


Figure 3.6: (a): Time evolution of the vertical components of the forces acting on the apex of the emerging loop: gas pressure gradient ( $-\nabla p = -dp/dz$ , solid line), gravity ( $\rho g_0$ , dotted line), magnetic pressure gradient ( $-\nabla p_{\text{mag}} = -d[B^2/(8\pi)]/dz$ , dashed line), and magnetic tension ( $t_{\text{mag}} = [(B \cdot \nabla)B]_z/(4\pi)$ , dashed-dotted line). (b): The same of the acceleration ( $F_z/\rho = (-\nabla p - \rho g_0 - \nabla p_{\text{mag}} - t_{\text{mag}})/\rho$ ). A dotted line shows that the acceleration equals zero.

process can possibly explain the formation of the ‘initial flux’ of the previous studies in much smaller scales (e.g. Shibata et al., 1989, etc.). We have to carry out three dimensional experiments because another effects such as the aerodynamic drag would act on the actual expanding loops. However, the above-mentioned scheme can explain the deceleration in the convection zone if the emerging field has a sheet-like shape rather than a tubular form.

### 3.3.3 Third Stage ( $1900 < t/\tau_0 < 2000$ )

The field is decelerated and flattened due to the isothermal (sub-adiabatic) stratification on the surface; meanwhile, the fluxes are continuously transported from beneath, that is, the magnetic pressure gradient keeps enhancing at the surface (Figure 3.2(e)). At the location where the magnetic pressure gradient gets steepened enough, the further evolution to the corona occurs on the basis of the Parker instability. At the point of the second-step emergence, a ‘pressure hill’ (Archontis et al., 2004; Magara, 2001) is formed, which indicates that the plasma in the photosphere drains out sideways and the magnetic field covers this area, i.e., the stratification is top-heavy (see Figure 3.7).

To confirm the onset of the Parker instability, we use the criterion obtained by Newcomb (1961). The criterion for the Parker instability is (Newcomb, 1961)

$$-\frac{d\rho}{dz} < \frac{\rho^2 g_0}{\gamma p}. \quad (3.9)$$

We plot the index

$$\psi \equiv -\frac{d\rho}{dz} - \frac{\rho^2 g_0}{\gamma p}, \quad (3.10)$$

that is, the area with negative  $\psi$  is subject to the instability. Figure 3.8 illustrates the  $\psi$  distribution with field lines just before the second-step emergence at  $t/\tau_0 = 1960$ . This figure indicates that the index  $\psi$  is negative at around the point of emergence; we can

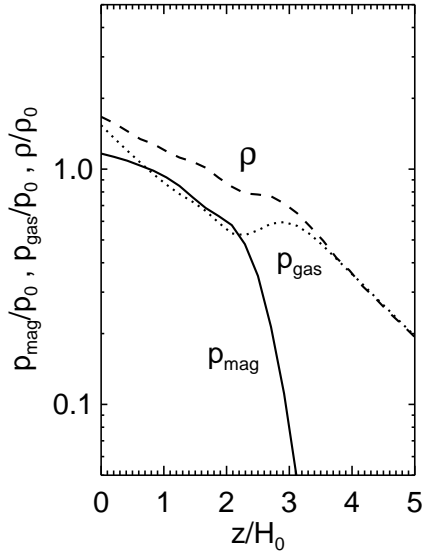


Figure 3.7: Vertical distributions of magnetic pressure (solid line), gas pressure (dotted line), and gas density (dashed line) along the axis  $x/H_0 = 20$  at  $t/\tau_0 = 1960$ , which is the central position of the second-step emergence.

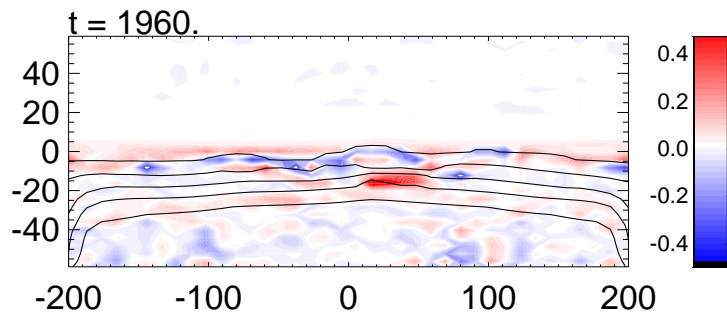


Figure 3.8: Spatial distribution of the index  $\psi \equiv -d\rho/dz - \rho^2 g_0/(\gamma p)$  at the location shown by the white box in Figure 3.2(e). Color contour indicates  $\psi$  (blue represents negative), while magnetic field lines are overplotted by solid lines. The aspect ratio is arranged. The index  $\psi$  is negative around the area of the further evolution ( $x/H_0 = 20, z/H_0 = 0$ ), indicating that this area is subject to the Parker instability.

conclude that the further evolution to the corona is ascribed by the Parker instability.

At  $t/\tau_0 = 1960$ , plasma  $\beta \equiv 8\pi p/B^2$  is order of unity ( $\sim 2$ ) and the magnetic field strength is about 700 G at the low photosphere within the emergent area, which are consistent with observations (e.g. Watanabe et al., 2008).

### 3.3.4 Fourth Stage ( $t/\tau_0 > 2000$ )

In this final phase, the magnetic flux emerging within the photosphere begins to expand to the solar corona by the magnetic pressure on the condition that the gas pressure acting on the surface of the flux is weak enough (Figures 3.2(f)-(h)). The expanding loop finally forms a large coronal loop. This process is similar to that of the results of classical calculations (e.g. Shibata et al., 1989, etc.).

The characteristics of this nonlinear phase is a self-similar evolution. Figures 3.9(a)-(c) indicate the distributions of the vertical component of velocity, gas density, and horizontal magnetic field strength along the axis  $x/H_0 = 20$ , where the apex of the loop is located (see Figures 3.2(g) and (h)), at  $t/\tau_0 = 2000, 2020$ , and  $2040$ . According to Shibata et al. (1989), the expansion law is written as

$$V_z/C_{s0} = a z/H_0, \quad (3.11a)$$

$$\rho \propto z^{-4}, \quad (3.11b)$$

$$B_x \propto z^{-1}, \quad (3.11c)$$

where  $a = 0.05\text{--}0.07$  is about half the non-dimensional linear growth rate for plasma  $\beta = 0.5\text{--}2.0$  of the flux sheet. In our study, plasma  $\beta$  of the magnetic field has been calculated to be 2 at  $t/\tau_0 = 1960$  before the further evolution begins (see Section 3.3.3), which suggests that the velocity-height relation is

$$V_z/C_{s0} \sim 0.05 z/H_0. \quad (3.12)$$

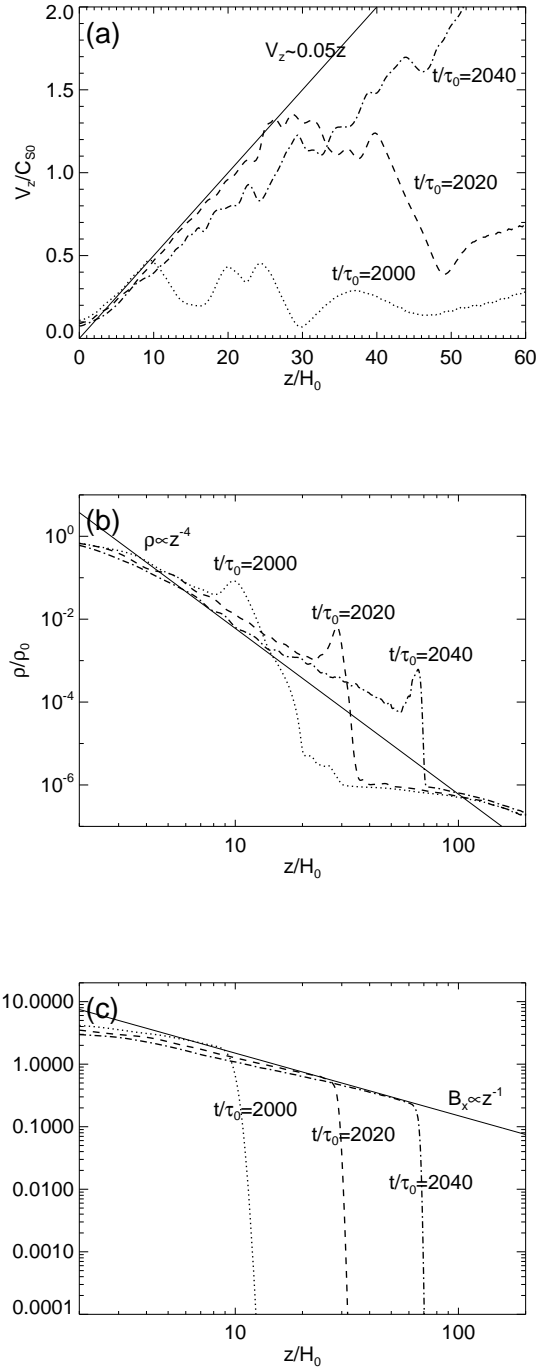


Figure 3.9: (a): Distribution of the upward velocity along the vertical axis  $x/H_0 = 20$ . Dotted, dashed, and dash-dotted lines indicate the distribution at  $t/\tau_0 = 2000$ ,  $t/\tau_0 = 2020$ , and  $t/\tau_0 = 2040$ , respectively. A solid line shows the theoretical velocity-height relation according to Shibata et al. (1989). (b): Distribution of the gas density along the axis  $x/H_0 = 20$ . The notation of lines is the same as in (a). (c): Distribution of the horizontal component of the magnetic field along the axis  $x/H_0 = 20$ . The notation of lines is the same as in (a).

This relation is overplotted in Figure 3.9(a) with a solid line. The other relations given by equations (3.11b) and (3.11c) are also overplotted in Figures 3.9(b) and (c) with solid lines. As seen from Figure 3.9, the nonlinear growth to the solar corona is consistent with that of Shibata et al. (1989).

The size of the coronal loop at  $t/\tau_0 = 2070$  is found to be of  $400H_0 = 80,000$  km width and  $200H_0 = 40,000$  km height, while, at the surface, plasma  $\beta$  is of the order of unity and the field strength is about  $4B_0 (= 1200$  G).

## 3.4 Parameter Survey and Discussion

We carry out a parameter survey by changing the values of the initial field strength  $B_x$  and the total magnetic flux  $\Phi$  of the emerging flux sheet to investigate the condition of the sheet's behavior. A summary of the values of  $B_x$  and  $\Phi$  under consideration is given in Table 3.1. Figure 3.10 shows the results of the parameter survey, where diamonds, asterisks, and X's represent ‘two-step,’ ‘direct,’ and ‘failed’ evolution, respectively. Fluxes belong to the direct emergence group do evolve into the corona, however, they do not reveal the deceleration, unlike fluxes of the two-step emergence, while those of the failed emergence fragment within the convection zone or cannot pass through the photosphere. Figure 3.11 indicates height-time relations of the fluxes along the axis  $x/H_0 = 0$ . In this Section, we will discuss each group in detail.

### 3.4.1 Direct emergence

In cases 2 and 3, the fluxes show the emergence to the corona without any deceleration at the surface. In other words, they ‘directly’ emerge to the corona. As shown in Figure 3.11(a), the height-time curves of cases 2 and 3 do not have an inflection point. We name them the ‘direct emergence’ group. The absence of an inflection implies that their evolutions are not affected by the isothermal photosphere/chromosphere at all since they have extremely strong field (note that these cases can be found in the upper right of Figure

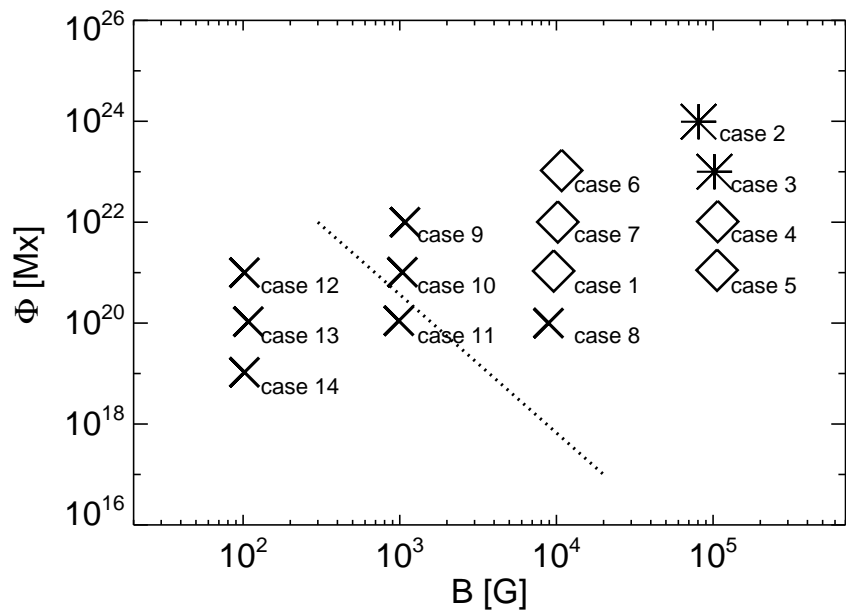


Figure 3.10: Results of the parameter survey. Diamonds, asterisks, and X's represent two-step emergence, direct emergence, and failed emergence, respectively. Case numbers are plotted on the lower right of each symbol. Criteria for the ‘explosion’ of the emerging flux obtained by thin-flux-tube approximation simulations (Moreno-Insertis et al., 1995) is overplotted with a dotted line.

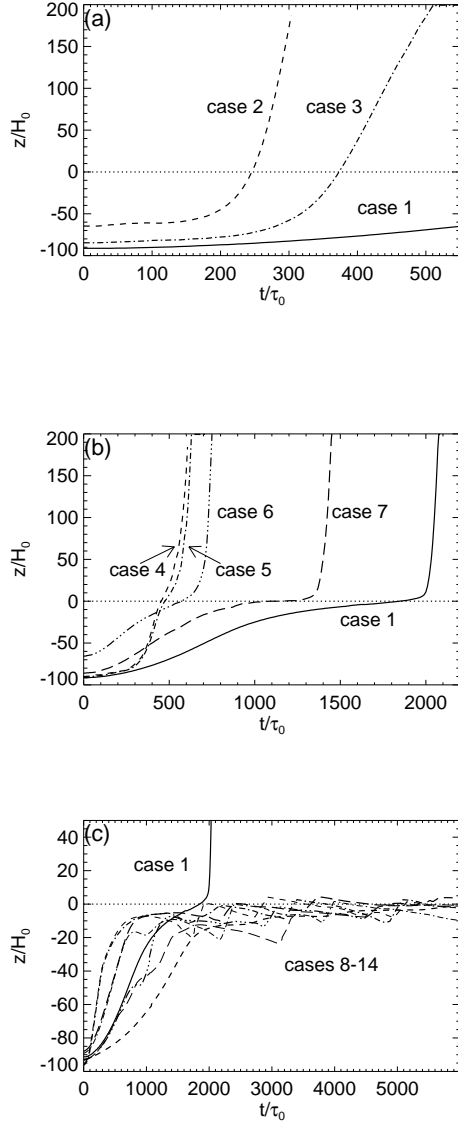


Figure 3.11: (a): Time evolution of the height of the flux sheet along the axis  $x/H_0 = 0$  for ‘direct emergence’ (cases 2 and 3). Dashed and dashed-dotted lines represent evolutions of cases 2 and 3, respectively, while solid line is the height-time relation of case 1 (typical model). (b): Same for ‘two-step emergence’ (cases 1 and 4-7). Solid, dashed, dashed-dotted, dashed-triple-dotted, and long-dashed lines represent evolutions of cases 1, 4, 5, 6, and 7, respectively. (c): Same for ‘failed emergence’ (cases 8-14). Dashed (thick), dash-dotted (thick), long-dashed (thick), dashed-triple-dotted, dashed (thin), and dash-dotted (thin), long-dashed (thin) lines represent evolutions of cases 8, 9, 10, 11, 12, 13, and 14, respectively, while solid line is the height-time relation of case 1 (typical model). In each panel, dotted line is overlaid to show the surface level ( $z/H_0 = 0$ ).

3.10).

Figure 3.12 shows the time evolution of the density profile, magnetic field lines, and velocity vectors for case 2. Color contour is the same as that of Figure 3.2. Each flux of this group exhibits field strength  $B \sim 10^4$  G and plasma  $\beta \sim 0.1$  at the surface after the emergence, which is not consistent with observations. Therefore, ‘direct emergence’ model is not suited for the formation model of active regions.

### 3.4.2 Two-step emergence

Cases 4–7 show the ‘two-step emergence’ to the corona as well as case 1 (typical model). Height-time relations of this group are shown in Figure 3.11(b). Each line of this group has an inflection point beneath the surface ( $z/H_0 = 0$ ), that is, rise velocity of the emerging flux turns from acceleration to deceleration phase within the convection zone due to the isothermal photosphere/chromosphere. As the figure indicates, the temporal length of the rising stage decreases with increasing initial field strength and total flux.

Among these five cases, cases 4, 5, and 6 show unrealistically strong flux densities  $B \sim 10^4$  G (plasma  $\beta \sim 0.1$ ) at the photosphere after the coronal loops are built up. The realistic models of the formation of active regions are cases 1 and 7 ( $\Phi = (10^{21}–10^{22})$  Mx with  $B_x = 10^4$  G at  $z = -20,000$  km). This result gives an important suggestion that the fluxes which form active regions are likely to have experienced the ‘two-step emergence.’

Our numerical results agree with recent satellite data. Otsuji et al. (2010) found the deceleration and the horizontal spreading of an emerging flux within the solar chromosphere by using *Hinode*/SOT. This observation supports the concept of the ‘two-step emergence’ model. At the same time, there is a difference between our results and the observation. The deceleration occurs in the chromosphere, not beneath the surface. The difference may partly come from the structure of the emerging loop. The numerical flux considered here has a sheet-like structure, on which the plasma piles continuously during its evolution (see Section 3.3). If the emerging loop is part of a (twisted) flux tube, the plasma

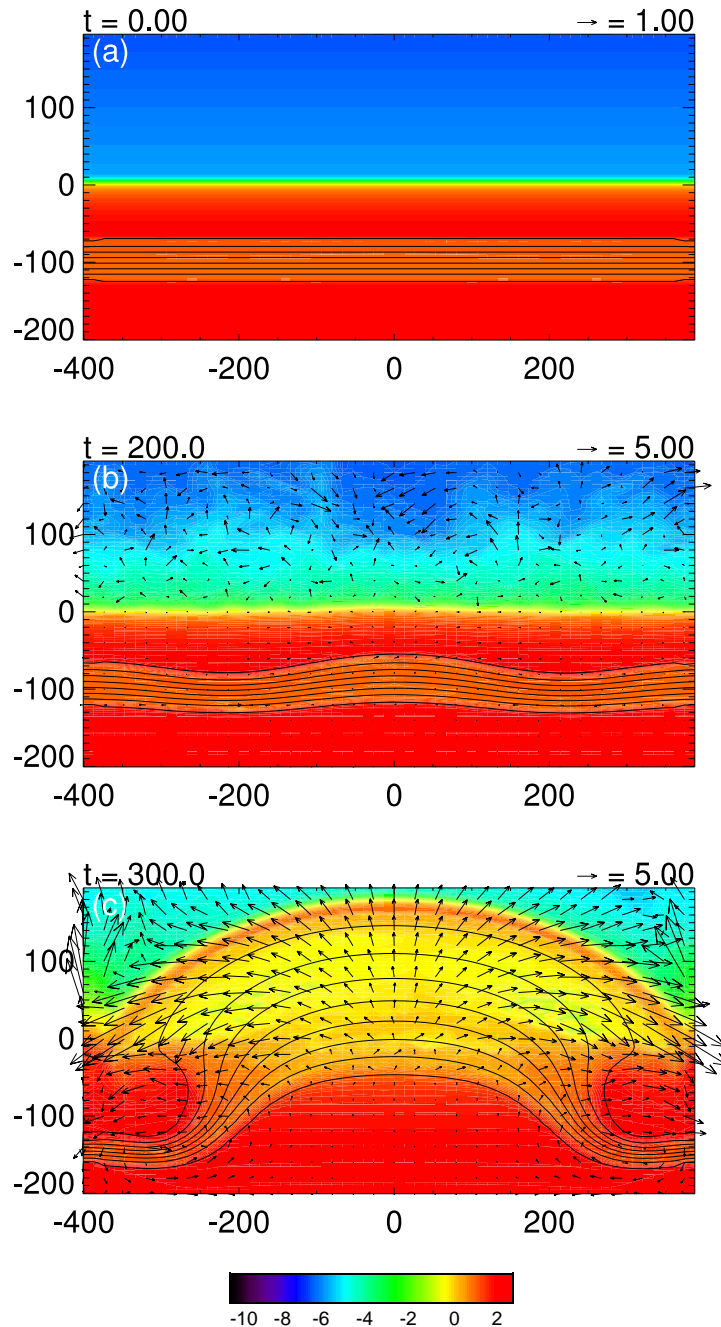


Figure 3.12: Time-evolution of the ‘direct emergence’ for case 2. (a)  $t/\tau_0 = 0$ ; (b)  $t/\tau_0 = 200$ ; (c)  $t/\tau_0 = 300$ . Logarithmic density profiles ( $\log_{10}(\rho/\rho_0)$ ) are indicated by color contour, while magnetic field lines and velocity vectors are overplotted with black lines and arrows.

on the loop can drain around the cross-section of the tube. Therefore, the emerging flux tube may rise through the convection zone faster than the sheet-like flux, and the tube may suffer a deceleration at a higher altitude when the tube itself passes through the convectively stable layers. On the other hand, Magara (2001) reported that even in case with an initial twisted tube, there is a deceleration close to the photosphere. The attribution of the deceleration altitude to the structure of the magnetic flux is still oversimplified at this moment. More quantitative study by three-dimensional simulations concerning with this issue is necessary.

It is possible that the emerging flux suffers a deceleration beneath the surface and exhibits the ‘two-step’ evolution, or, in some cases, fluxes show the ‘multi-step’ emergence since the structure of the rising loop in the convection zone cannot be achieved by the optical observations. To know the structure and the behavior of the flux emergence below the photosphere, advanced local helioseismology is needed (e.g. Sekii et al., 2007).

### 3.4.3 Failed emergence

Cases given in Figure 3.10 with X’s belong to the ‘failed emergence’ group (cases 8–14). Fluxes of cases 9–14 suffer a fragmentation due to the continuous motion within the convection zone, so that further emergence does not occur (see Figure 3.13). It is because the fluxes have weak fields compared to the local kinetic energy density of flow motion induced by the initial perturbation. Figure 3.14 shows the ratio of the magnetic energy density  $E_{\text{mag}}$  to the local kinetic energy density  $E_{\text{kin}}$  of case 14 along  $x/H_0 = 0$  at  $t/\tau_0 = 4000$  (Figure 3.13(e)), where  $E_{\text{mag}} = B^2/(8\pi)$  and  $E_{\text{kin}} = \rho v^2/2$ , respectively. It reveals that the magnetic energy is weaker than the kinetic energy all over the convective layer. Height-time relations of these fluxes are presented in Figure 3.11(c). As the figure shows, each line of this group reveals a continuous fluctuation and remains around the surface, indicating that the continuous motion repeats within the solar interior. On the other hand, flux of case 8 do not show the secondary emergence because the flux fails

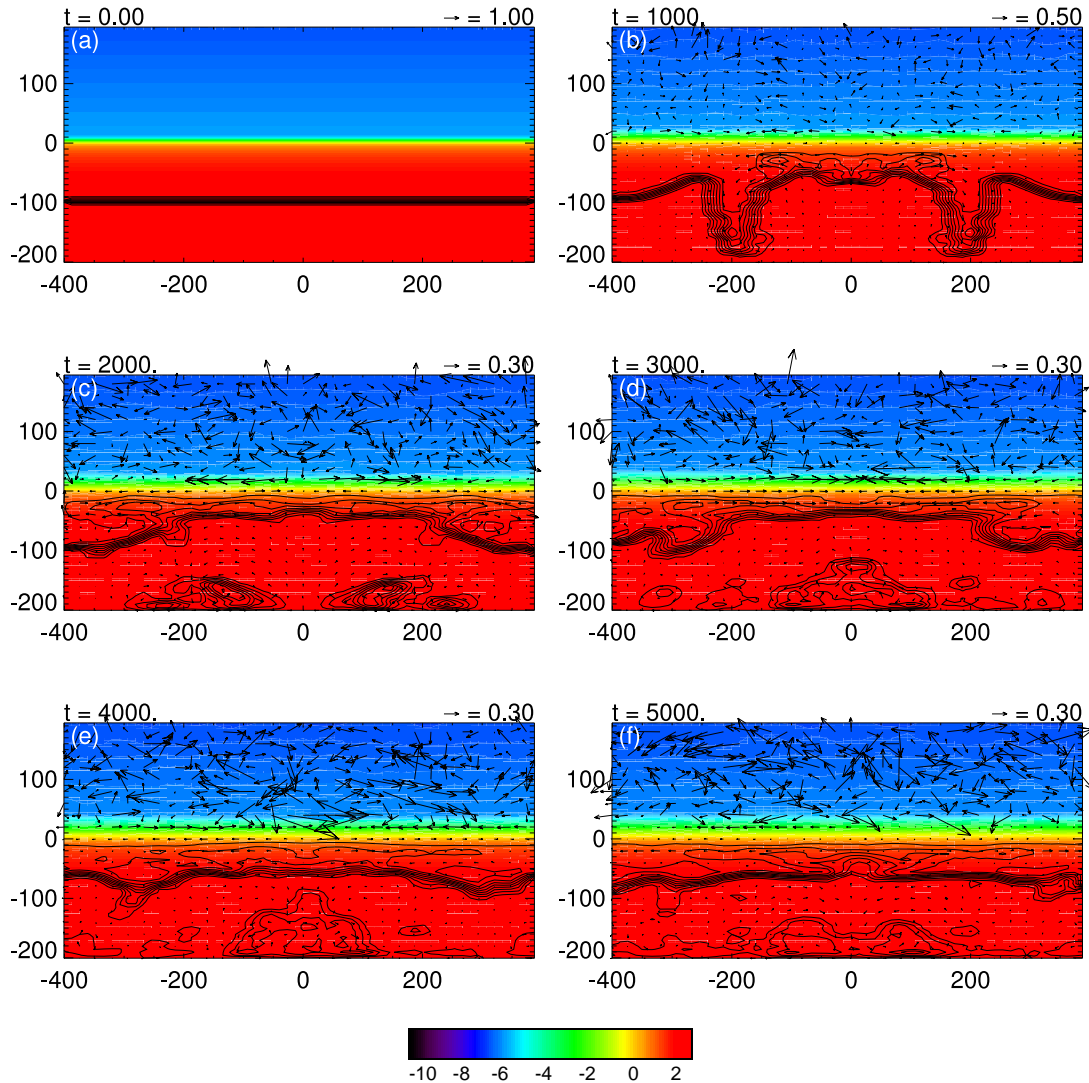


Figure 3.13: Time-evolution of the ‘failed emergence’ for case 14. (a)  $t/\tau_0 = 0$ ; (b)  $t/\tau_0 = 1000$ ; (c)  $t/\tau_0 = 2000$ ; (d)  $t/\tau_0 = 3000$ ; (e)  $t/\tau_0 = 4000$ ; (f)  $t/\tau_0 = 5000$ . Logarithmic density profiles ( $\log_{10}(\rho/\rho_0)$ ) are indicated by color contour, while magnetic field lines and velocity vectors are overplotted with black lines and arrows.

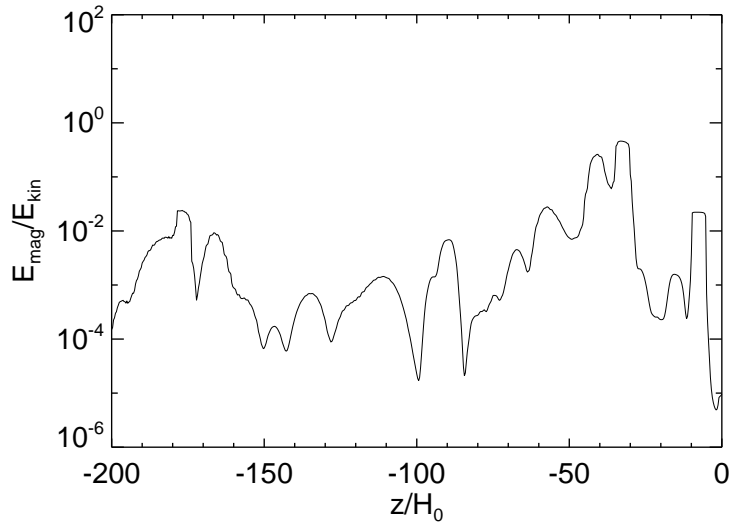


Figure 3.14: The ratio of  $E_{\text{mag}} = B^2/(8\pi)$  to  $E_{\text{kin}} = \rho v^2/2$  of case 14 along  $x/H_0 = 0$  at  $t/\tau_0 = 4000$ .

to enhance the magnetic pressure gradient while crossing the surface. This flux keeps its coherency all the while since the field strength is almost in the same range as the local kinetic energy density (see Figure 3.15).

Dotted line in Figure 3.10 indicates the criteria for the ‘explosion’ of the emerging flux obtained by thin-flux-tube (TFT) approximation (Moreno-Insertis et al., 1995). They found that the rising tubes with a small amount of flux cannot reach the surface due to the ‘explosion’: if the tube rises sufficiently slowly, the stratification inside the tube gets close to a hydrostatic equilibrium along the field lines while the stratification outside is super-adiabatic. When the pressure difference between inside and outside the tube is small enough at the base of the convection zone, the difference decreases as the tube rises because the pressure gradient inside the tube is less steeper than that outside, so that the magnetic field at the apex can no longer be confined at a certain ‘explosion’ depth. According to their calculations, the tubes with the initial field strength and magnetic flux ( $10^4$  G,  $10^{22}$  Mx) and ( $10^5$  G,  $10^{17}$  Mx) at the base of the convection zone can reach close to the surface. Their field strength at  $r/R_\odot = 0.97$  ( $z = -20,000$  km, i.e., the depth of our initial fluxes) are  $3 \times 10^2$  G and  $2 \times 10^4$  G, respectively (see Moreno-

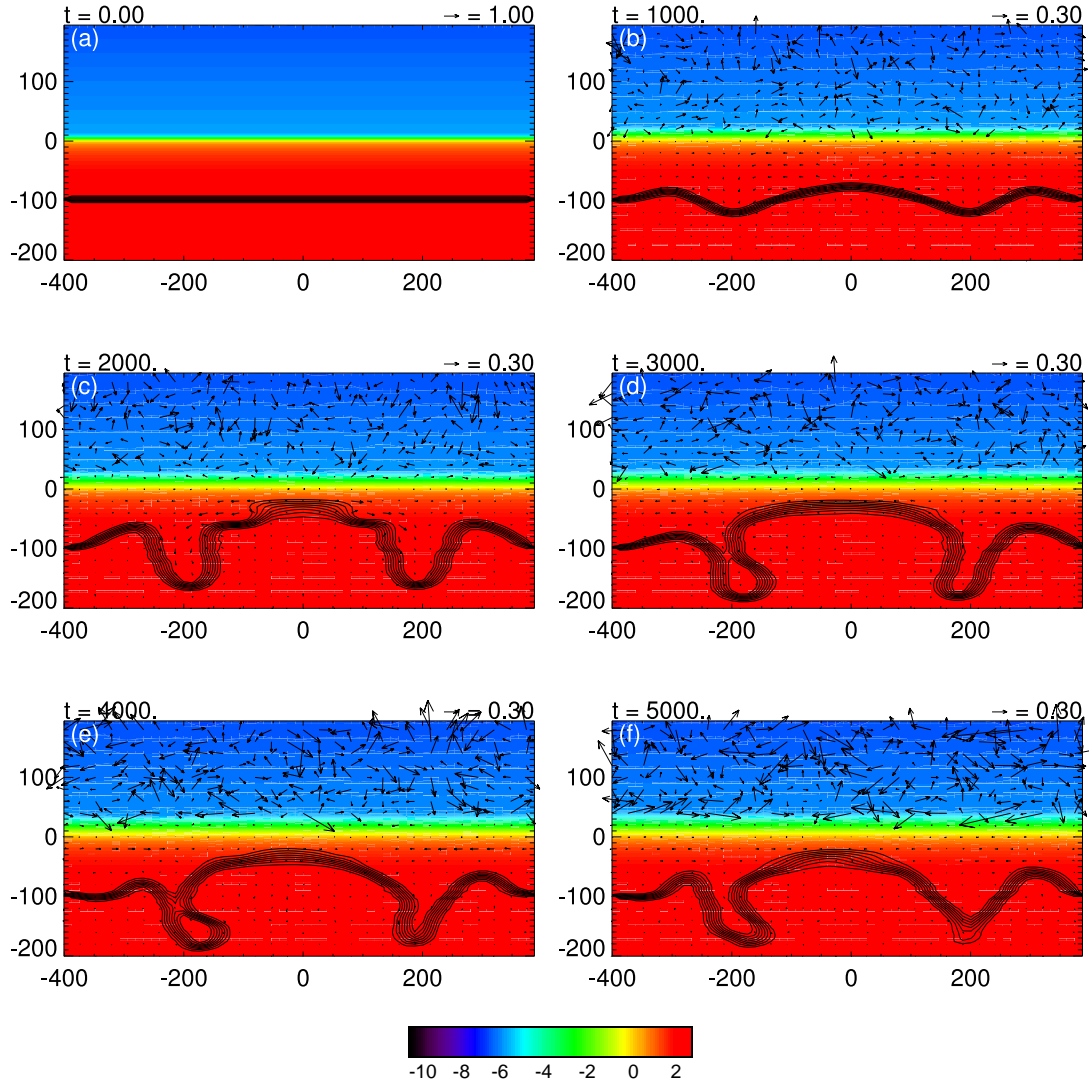


Figure 3.15: Time-evolution of the ‘failed emergence’ for case 8. (a)  $t/\tau_0 = 0$ ; (b)  $t/\tau_0 = 1000$ ; (c)  $t/\tau_0 = 2000$ ; (d)  $t/\tau_0 = 3000$ ; (e)  $t/\tau_0 = 4000$ ; (f)  $t/\tau_0 = 5000$ . Logarithmic density profiles ( $\log_{10}(\rho/\rho_0)$ ) are indicated by color contour, while magnetic field lines and velocity vectors are overplotted with black lines and arrows.

Insertis et al., 1995, Figure 1). We adopt them as criteria for the ‘non-explosion’. The majority of the fluxes with parameters in the range where they could not have reached at  $z = -20,000$  km according to the TFT model (left to the dotted line) also ceases emergence even in our MHD model.

There are, however, some cases in which, although the fluxes are expected to reach at  $z = -20,000$  km level by the TFT model, they fail to evolve further (cases 8, 9 and 10). Especially, case 8 ( $10^4$  G with  $10^{20}$  Mx at  $z = -20,000$  km) reveals the photospheric field strength  $B \sim 1$  G, indicating it could be the source of the magnetic fields in the quiet sun if the fields are enhanced, e.g., by the flux expulsion due to the magneto-convection at the surface. Interestingly, this flux maintains its coherency all the while and remains floating around beneath the surface after it fails the further evolution to the corona because it has a strong field that is in equipartition with the kinetic energy density (Figure 3.15). This suggests that the flux of case 8 can be the origin of the ephemeral regions. Flux 8 has  $10^{20}$  Mx, consistent with the flux of mid-sized ephemeral regions (Hagenaar, 2001).

### 3.5 Conclusions

We perform the nonlinear two-dimensional simulations to investigate the behavior of emerging flux from moderately deep convection zone ( $z = -20,000$  km). We set a much wider numerical box ( $160$  Mm  $\times$   $80$  Mm) than those of the previous experiments on the Parker instability (e.g. Shibata et al., 1989).

In the typical case ( $B = 10^4$  G with  $\Phi = 10^{21}$  Mx at  $z = -20,000$  km), the results show the ‘two-step emergence’. In the middle of the way of the first emergence to the solar surface, the flux loop turns from an acceleration phase to deceleration when approaching the (sub-adiabatically stratified, i.e., convectively stable) photosphere/chromosphere. The emerging flux has a sheet-like shape, thus it is difficult for the mass on the loop to escape from the area between the loop and the convectively stable surface. This mass pile-up causes the loop decelerate. The deceleration of the apex of the expanding flux and the

continuous rising of the hillsides make loop flattened, which results in the plasma kept on the flux. This deceleration mechanism is another new one and different from those of the preceding studies (Magara, 2001; Archontis et al., 2004; Murray et al., 2006) with magnetic flux tubes in much smaller regions. However, our result predicts the behavior of a flux within the convection zone, provided the flux has a sheet-like structure . As a result of the deceleration and the flattening, the flux spreads sideways just beneath the surface, at which point the rise velocity of the crest of the loop is almost zero. Meanwhile, the flux is continuously transported from below, then the magnetic pressure gradient enhances locally in the photosphere. We found that the further evolution to the corona occurs on the basis of the Parker instability. At the point of the instability, plasma  $\beta$  is calculated to be order of unity ( $\sim 2$ ) and the magnetic field strength is about 700 G. In the final stage, the flux shows the nonlinear evolution to the corona, which resembles the classical experiments (e.g. Shibata et al., 1989, etc.). The second-step evolution is described clearly by the expansion law by Shibata et al. (1989). We find that the coronal loop exhibits 80,000 km width with 40,000 km height, while the field strength of each footpoint at the surface is about 1200 G.

We perform parameter runs by changing the initial field strength  $B_x$  and the total flux  $\Phi$  to investigate the condition of the ‘two-step emergence’. The results of the runs under considerations can be divided into three groups: ‘direct’, ‘two-step’, and ‘failed’ emergence. In case of the ‘direct emergence’, the flux do evolve to the corona, but they do not show the deceleration by the isothermal surface due to their strong initial magnetic fields (( $10^{23}$ – $10^{24}$ ) Mx with 10<sup>5</sup> G at  $z = -20,000$  km). The coronal loops present irregularly strong flux densities at the footpoints; thus, we conclude that they are not suitable for the formation models of active regions. As for the cases showing the ‘two-step emergence’, two out of five exhibit the favorable values of the photospheric field strength and plasma  $\beta$ . The others have so large values that they cannot be regarded as realistic models of active regions. We can say that active regions on the sun are likely to have undergone the deceleration and likely to show the ‘two-step emergence’ mentioned

above. The condition for this ‘two-step’ active region is ranging from  $10^{21}$  to  $10^{22}$  Mx with  $10^4$  G at  $z = -20,000$  km in the convection zone. Some recent observations support this two-step model. The cases with  $B \lesssim 10^4$  G reveal ‘failed’ evolutions; they fragment within the convection zone or cannot have sufficient magnetic pressure gradient to trigger the instability that the second-step emergence do not occur although the flux maintains its coherency. We have some discussions in connection with the results of the thin-flux-tube (TFT) model by Moreno-Insertis et al. (1995). The cases which are found to have ‘exploded’ in the deeper point in the TFT scheme also do not show further evolutions in our MHD scheme. However, there are some cases which escape the ‘explosion’ fail the second-step evolutions, one of which is possibly the source of the magnetic field in the quiet sun.

The present calculations are in a two-dimensional scheme solving simplified equations. Thus we have to demonstrate the more realistic experiments in 3D. At the same time, advanced observations by helioseismological technique are needed to reveal the detail of the emerging flux in the convection zone.



# Chapter 4

## Two-dimensional Experiment: Cross-sectional Evolution

### 4.1 Introduction

In this Chapter, we show the cross-sectional calculation of the rising flux tube from the deep convection zone ( $\sim 20,000$  km). As the initial condition (the field strength and the total flux), we adopt the similar values as obtained from the undular mode emergence in Chapter 3. That is, the field strength of the order of  $10^4$  G and the flux of  $\sim 10^{21}$  Mx.

We also study the parametric surveys on and the twist intensity and the field strength. The twist of the tube is needed to keep the tube's coherency during its ascent in the interior (see Section 1.3). Here, the twist intensity is indicated by the parameter  $q$ . For a uniformly twisted flux tube,  $B_\phi(r) = qrB_x(r)$ , where  $B_\phi(r)$  is the azimuthal field,  $B_x(r)$  the axial field, and  $r$  the radial distance to the tube axis. To keep the tube coherent, the restoring inward magnetic tension exerted by the azimuthal component should overcome the the magnetic buoyancy, namely,

$$\frac{B_\phi^2}{4\pi R_{\text{tube}}} > \frac{B_x^2 + B_\phi^2}{8\pi H_p}, \quad (4.1)$$

where  $R_{\text{tube}}$  is the tube radius and  $H_p$  the local pressure scale height. Assuming  $R_{\text{tube}} \ll$

$H_p$ , one can get the condition (Longcope et al., 1999)

$$q \gtrsim \left( \frac{1}{H_p R_{\text{tube}}} \right)^{1/2}. \quad (4.2)$$

If we use the values  $R_{\text{tube}} = 5H_0$  and  $H_p = 40H_0$  at a depth of 20,000 km, the twist intensity required is of order

$$q \gtrsim 0.07 \frac{1}{H_0}, \quad (4.3)$$

which is well accorded with the numerical results (see Section 4.4).

## 4.2 Numerical Model

We consider the buoyant rise of an isolated magnetic flux tube in the stratified ideal gas layers in the  $(y, z)$ -plane, where the  $z$ -coordinate increases upward. We solve the standard set of ideal MHD equations including constant gravitational acceleration  $\mathbf{g} = (0, 0, -g_0)$ . The basic equations are shown in Chapter 2. In this study, we carry out so-called 2.5-dimensional numerical simulation, that is, all the physical quantities are independent of  $x$  while the  $x$ -component of vector quantities (i.e., velocity  $\mathbf{V}$  and magnetic field  $\mathbf{B}$ ) is taken into account.

The initial background stratification consists of three regions: an adiabatically stratified convection zone, a cool isothermal photosphere/chromosphere, and a hot isothermal solar corona. We take  $z = 0$  to be the base height of the photosphere, and the initial temperature distribution of the photosphere/chromosphere and the corona ( $z \geq 0$ ) is assumed to be

$$T = T_s(z) \equiv T_{\text{ph}} + \frac{1}{2}(T_{\text{cor}} - T_{\text{ph}})\{\tanh[(z - z_{\text{cor}})/w_{\text{tr}}] + 1\}, \quad (4.4)$$

where  $T_{\text{ph}} = T_0$  and  $T_{\text{cor}} = 100T_0$  are the respective temperatures in the photosphere/chromosphere

and the corona,  $z_{\text{cor}} = 10H_0$  is the base of the corona, and  $w_{\text{tr}} = 0.5H_0$  is the temperature scale height of the transition region. The initial temperature distribution in the convection zone ( $z \leq 0$ ) is described as

$$T = T_s(z) \equiv T_{\text{ph}} - z \left| \frac{dT}{dz} \right|_{\text{ad}}, \quad (4.5)$$

where

$$\left| \frac{dT}{dz} \right|_{\text{ad}} = \frac{\gamma - 1}{\gamma} \frac{mg_0}{k_B} \quad (4.6)$$

is the adiabatic temperature gradient, i.e., the initial temperature distribution in the convection zone is adiabatic. On the basis of the temperature distribution above, the initial pressure and density profiles are defined by the equation of static pressure balance:

$$\frac{dp_s(z)}{dz} + \rho_s(z)g_0 = 0. \quad (4.7)$$

The initial magnetic flux tube is embedded in the solar interior at  $z = -100H_0 = -20,000$  km. The longitudinal and azimuthal components of the flux tube are described as follows (see Fan, 2001; Archontis et al., 2004; Murray et al., 2006): for  $r \equiv [(y - y_{\text{tube}})^2 + (z - z_{\text{tube}})^2]^{1/2}$ ,

$$B_x(r) = B_{\text{tube}} \exp \left( -\frac{r^2}{R_{\text{tube}}^2} \right), \quad (4.8)$$

and

$$B_\phi(r) = qrB_x(r), \quad (4.9)$$

where  $(y_{\text{tube}}, z_{\text{tube}}) = (0, -100H_0)$  is the tube center,  $R_{\text{tube}}$  is the tube radius,  $q$  is the twist parameter denoting the angular rate of field lines rotating around the tube's axis

per unit length, and  $B_{\text{tube}}$  is the field strength at the center. The horizontal and vertical components of the azimuthal field are defined as

$$B_y(y, z) = -B_\phi(r) \frac{z - z_{\text{tube}}}{r}, \quad (4.10)$$

and

$$B_z(y, z) = B_\phi(r) \frac{y - y_{\text{tube}}}{r}, \quad (4.11)$$

respectively. We use  $R_{\text{tube}} = 5H_0 = 1000$  km throughout the Chapter. For the typical case (case 1), we take  $B_{\text{tube}} = 50B_0 = 1.5 \times 10^4$  G, so that the total longitudinal magnetic flux is  $\Phi_x = 4.7 \times 10^{20}$  Mx. The twist parameter is  $q = 0.1/H_0$  for case 1. The pressure inside the tube is defined as

$$p_i(y, z) = p_s(z) + \delta p_{\text{exc}}(r), \quad (4.12)$$

where  $\delta p_{\text{exc}}(< 0)$  is the pressure excess described as

$$\delta p_{\text{exc}}(r) = \frac{B_x^2(r)}{8\pi} \left[ q^2 \left( \frac{R_{\text{tube}}^2}{2} - r^2 \right) - 1 \right], \quad (4.13)$$

for the pressure balance. The temperature is kept unchanged, i.e., thermal balance is sustained,  $T_i(z) = T_s(z)$ . Since the density inside the tube is smaller than that outside, the flux tube will buoyantly rise through the convection zone. The initial temperature, density, and pressure profiles of the background stratification, and the total field strength  $B = [B_x^2 + B_\phi^2]^{1/2} = [B_x^2 + B_y^2 + B_z^2]^{1/2}$  of case 1 along  $y = 0$  are shown in Figure 4.1.

The domain of the simulation box is  $(y_{\min} < y < y_{\max})$  and  $(z_{\min} < z < z_{\max})$ , where  $y_{\min} = -400H_0$ ,  $y_{\max} = 400H_0$ ,  $z_{\min} = -150H_0$ , and  $z_{\max} = 250H_0$ . The total size of the simulation box is 160 Mm  $\times$  80 Mm. Periodic boundaries are assumed for  $y = y_{\min}$  and  $y = y_{\max}$ , symmetric boundaries for  $z = z_{\min}$  and  $z = z_{\max}$ . A wave-

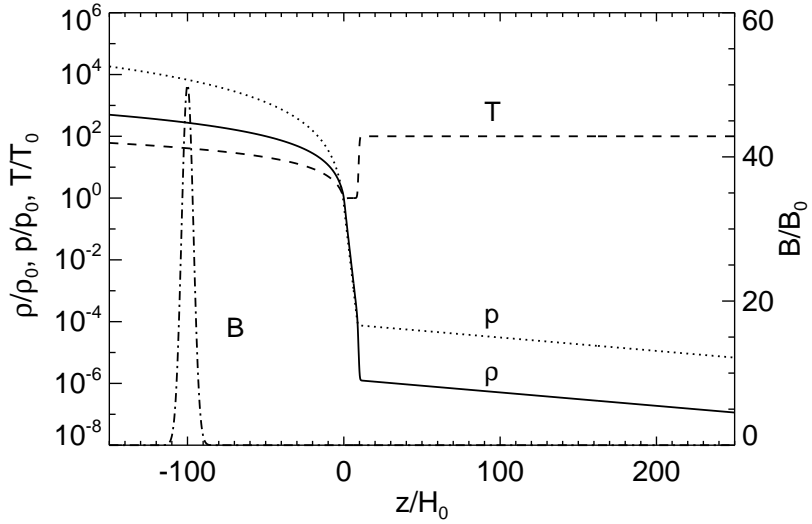


Figure 4.1: One-dimensional ( $z$ -)distributions of the initial background density (solid line), pressure (dotted line), and temperature (dashed line). The total magnetic field strength  $B = [B_x^2 + B_\phi^2]^{1/2}$  of case 1 along the vertical axis  $y = 0$  is overplotted with a dashed-dotted line.

damping region is attached near the top boundary. The total number of grid points is  $(N_y \times N_z) = (1536 \times 1920)$ , and the mesh sizes are  $\Delta y = 0.52H_0$  and  $\Delta z = 0.21H_0$ , both of which are uniform. To study the dependence on the twist and the field strength of the flux tube, we change the values for the twist parameter  $q$  or the axial field strength  $B_{\text{tube}}$ . The cases we use in this study are summarized in Table 4.1.

### 4.3 Results

Here, we show the results of the typical model (case 1) in which the initial twisted flux tube with  $q = 0.1/H_0$  rises through the convection zone to the corona. The evolution within the interior resembles the studies by Moreno-Insertis & Emonet (1996) and Emonet & Moreno-Insertis (1998), and the evolution to the upper atmosphere is similar to Magara (2001). However, the present result is not a simple sum of them; the rising tube decelerates within the interior far below the surface to build a widely flattened magnetic structure. The mechanism of the deceleration seems not to be the same as reported in Magara (2001),

since the deceleration depth is ten times deeper ( $-5000$  km in our case).

Figure 4.2 displays the evolution of the density profile (color contour) in a vertical plane normal to the tube axis, while the solid lines and arrows indicate the magnetic field lines and the velocity vectors, respectively. Figure 4.2(a) presents the initial state; the flux tube is located at  $z/H_0 = -100$  with a circular shape, and begins to emerge because of the buoyancy due to its smaller density relative to the surroundings. Figure 4.3(a) shows the height-time relations at the top (solid line), the center (dotted line), and the bottom (dashed line) of the emerging tube, while the velocities at these points are presented in Figure 4.3(b). In the initial phase ( $0 < t/\tau_0 < 100$ ), the flux tube rises due to magnetic buoyancy and the tube's cross-section almost keeps its original circular shape. Thus, the tube moves up with a constant acceleration rate. In the next phase ( $100 < t/\tau_0 < 500$ ), the aerodynamic drag grows to counteract buoyancy, since the external flow around the tube's cross-section develops a wake behind the main tube (Figure 4.2(c)), and the acceleration of the rise velocity is reduced. The azimuthal field of the flux tube resists this deformation and prevents the tube from fragmenting into a counter-rotating vortex pair (the so-called “umbrella shape” in Schüssler (1979)). During the emergence in the convection zone, the rise velocity of the tube center fluctuates due to the internal torsional oscillation (Figure 4.3(b); see §4.3.1). As the flux tube reaches close to the photosphere, it expands horizontally (Figure 4.2(e)) and its rise speed decreases after  $t/\tau_0 = 500$ . Eventually, the subsurface flux extends widely in the range of  $-100 < y/H_0 < 100$  at  $t/\tau_0 = 800$  (Figure 4.2(f)). When the top of the subphotospheric flux becomes unstable to the magnetic buoyancy instability, further evolution to the corona breaks out (Figures 4.2(f)-(i); see §4.3.3). The consequent coronal loop at the time  $t/\tau_0 = 980$  has its width  $\sim 400H_0 = 80,000$  km and height  $\sim 200H_0 = 40,000$  km. The picture of this evolution resembles our previous “two-step emergence” model (Chapter 3). In the following Sections, we will describe some more detailed results, especially on the magnetic and the flow field within the convection zone, the comparison with the analytic model, and the second-step evolution starting at the photosphere.

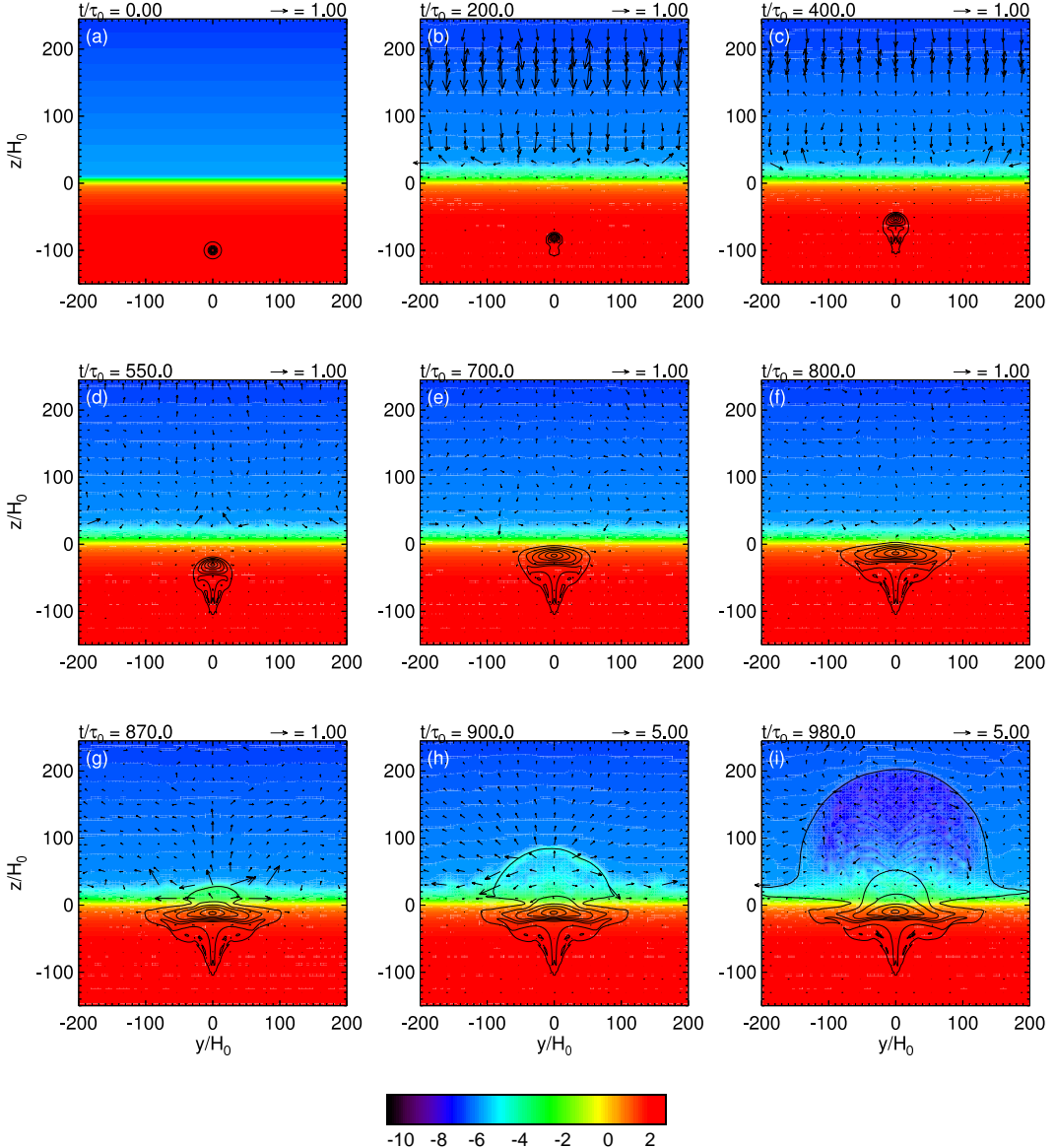


Figure 4.2: Time-evolution of the “two-step emergence” of the twisted flux tube (typical model). (a)  $t/\tau_0 = 0$ ; (b)  $t/\tau_0 = 200$ ; (c)  $t/\tau_0 = 400$ ; (d)  $t/\tau_0 = 550$ ; (e)  $t/\tau_0 = 700$ ; (f)  $t/\tau_0 = 800$ ; (g)  $t/\tau_0 = 870$ ; (h)  $t/\tau_0 = 900$ ; (i)  $t/\tau_0 = 980$ . Logarithmic density profiles ( $\log_{10}(\rho/\rho_0)$ ) are indicated by color contours, while magnetic field lines and velocity vectors are overplotted with black lines and arrows, respectively.

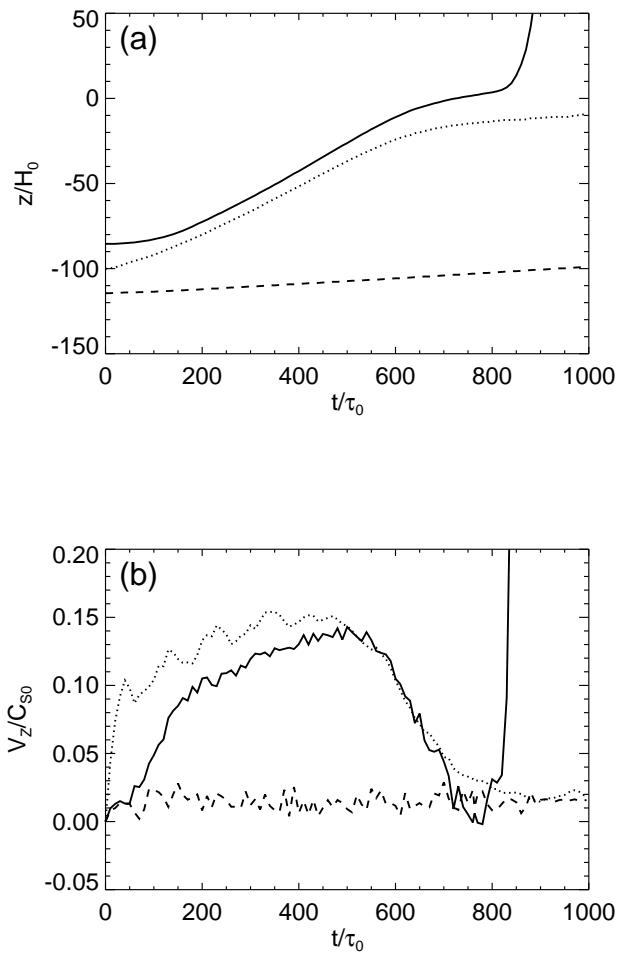


Figure 4.3: (a): Height-time relations at the top (solid line), the center (dotted line), and the bottom (dashed line) of the flux tube. (b): Gas velocities at these three points.

### 4.3.1 Magnetic Fields and Vorticity

To study the flux tube's emergence in the solar interior, we show the variation of the field configuration with time in Figure 4.4. The color contour indicates the distribution of the longitudinal field ( $B_x$ ) while the strength of the azimuthal field ( $B_\phi$ ) is overplotted with solid lines. In Figure 4.5, we plot the  $x$ -component of the vorticity vector ( $\omega_x$ ), where

$$\omega_x = \frac{\partial V_z}{\partial y} - \frac{\partial V_y}{\partial z}, \quad (4.14)$$

and white and black colors indicate positive (counter-clockwise) and negative vorticity (clockwise), respectively. These figures (Figure 4.4 and 4.5) look similar to those of previous experiments within the convection zone (Moreno-Insertis & Emonet, 1996; Emonet & Moreno-Insertis, 1998). Figures 4.4(a) and 4.5(a) present the initial state: the flux tube has a circular shape and there is no vorticity within the domain. As the tube begins to emerge, the field strength reduces and the tube expands, since the background density decreases with height (Figures 4.4(b)-(d)). Also, the external flow from the apex to the flanks of the tube creates negative and positive vortex sheets in the right and left side of the main tube, respectively (Figures 4.5(b)-(d)). Therefore, the tube is deformed and the wake behind the main tube grows with a pair of counter-rotating vortex rolls. Because of the azimuthal fields, however, the tube is not entirely fragmented into an “umbrella shape.” As a consequence, the rising tube feels aerodynamic drag, and, thus, the rise velocity levels off at this time. The longitudinal field component keeps its strength in the core of the vortex rolls as well as in the main tube (see Figure 4.4(e)). Behind the main tube, in  $-100 < z/H_0 < -60$  in Figure 4.4(f), there is a weakly magnetized tail with non-zero vorticity (Figure 4.5(f)).

During this phase, the rise speed of the tube center reveals oscillation as seen in Figure 4.3(b). This is a result of torsional oscillation due to the differential buoyancy caused by the magnetic field distribution (e.g. Moreno-Insertis & Emonet, 1996). Initially, the flux tube has its maximum field strength at the center so that the central region rises

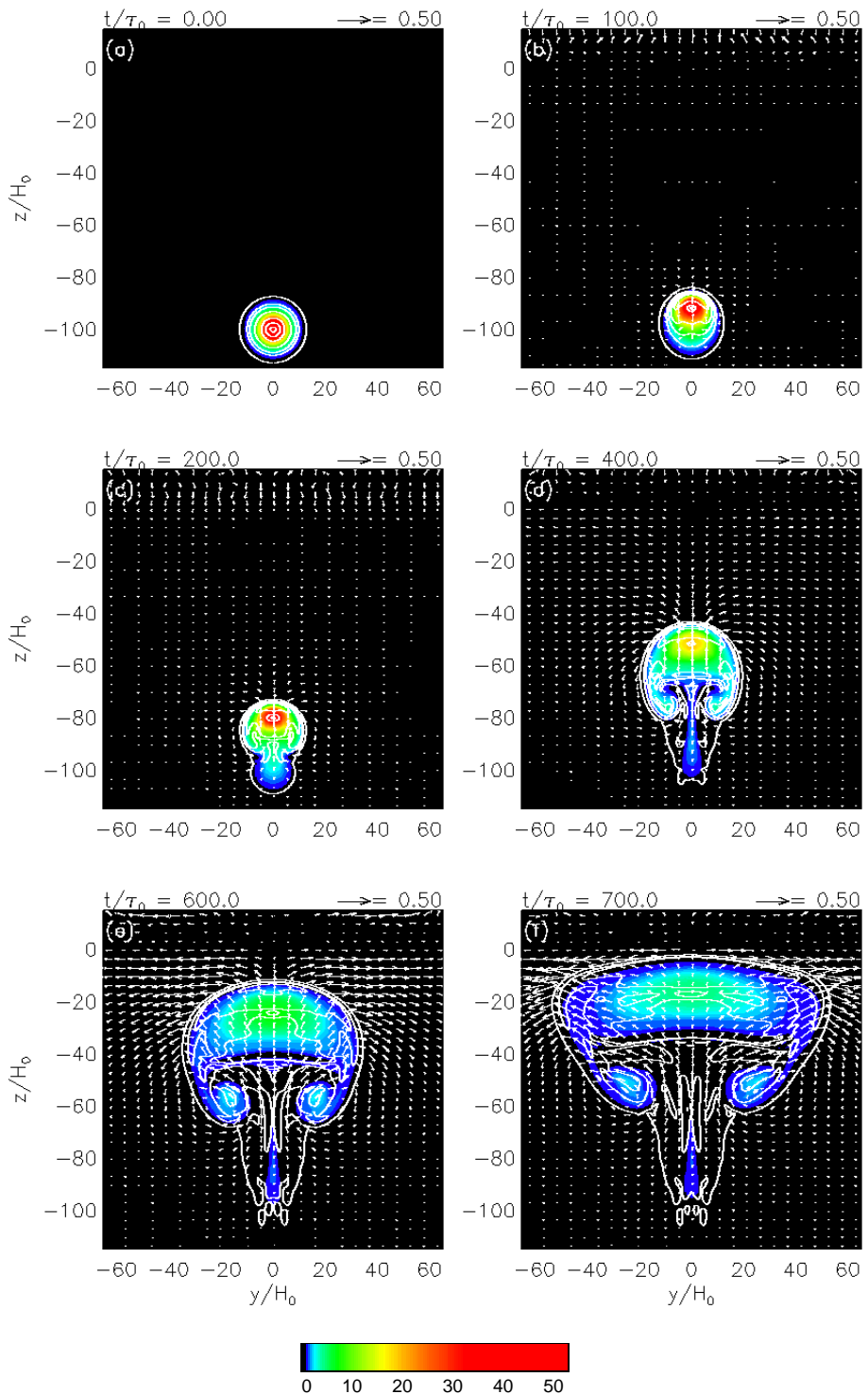


Figure 4.4: Time-evolution of the magnetic fields from  $t/\tau_0 = 0$  to  $t/\tau_0 = 700$ . Color contour displays the longitudinal component  $B_x/B_0$ , while the azimuthal component  $B_\phi/B_0$  is overplotted with solid lines.

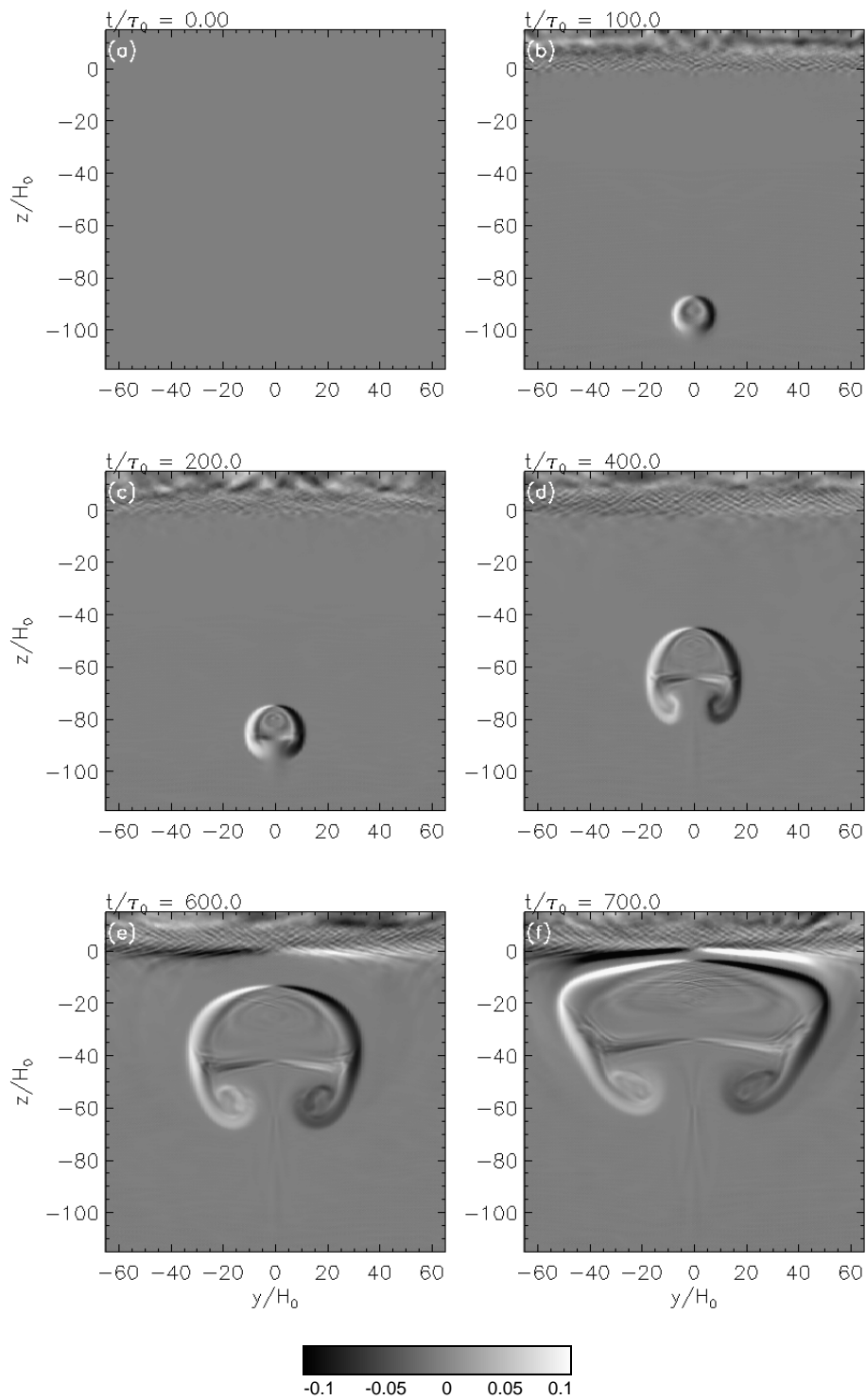


Figure 4.5: Same as Figure 4.4, but for the  $x$ -component of the vorticity. White indicates positive (counter-clockwise) vorticity, while black is negative (clockwise).

faster than the periphery. Therefore, the azimuthal field around the apex is compressed and strengthened to fortify the magnetic tension force, which inhibits the tube from a distortion into vortex rolls. The tension force decelerates the center of the tube and, as a result, induces the internal torsional oscillation. The period of this oscillation is observed to be consistent with the time of the azimuthal Alfvén speed traveling across the tube's diameter.

At around  $t/\tau_0 = 500$ , the rise motion begins to decelerate and the front of the tube expands horizontally, since the tube is close enough to the surface. The plasma above the rising tube cannot move through the isothermal (i.e., convectively stable) photosphere so that the fluid is compressed and piles up between the front of the tube and the photosphere. The fluid between them suppresses the rising motion of the flux below, and thus, the flux extends sideways. The horizontal expansion caused by the photosphere was previously reported by Magara (2001). His flux tube was not so deformed as to develop a wake including vortex rolls and directly entered the photosphere mostly keeping its original cylindrical shape, because the initial tube was located just beneath the surface ( $z_{\text{tube}} = -1800$  km) with a strong field strength ( $B_{\text{tube}} = 7760$  G). In our case, the initial tube was embedded so deep in the convection zone ( $z_{\text{tube}} = -20,000$  km) that the wake behind the main tube was formed and the drag force became more effective. The velocity shear between the horizontal flow above the tube and the photosphere forms vortex sheets at around  $z/H_0 \sim 0$  (Figure 4.5(e); the positive sheet in the right half, and the negative in the left). Finally, at  $t/\tau_0 = 700$ , the flux tube has a  $\nabla$ -shaped structure and the magnetic field extends widely beneath the surface (Figure 4.4(f)). The vortex sheet at the tube front collides against the subphotospheric sheet (Figure 4.5(f)). In this stage, the azimuthal field beneath the surface is much stronger than the longitudinal field because of the radial expansion of the flux tube (Parker, 1974, 1979).

### 4.3.2 Comparison with an Analytic Model

Fan et al. (1998) compared their numerical results of the emerging twisted flux tube obtained by 2.5D anelastic MHD experiments with those of the thin-flux-tube model. According to Fan et al. (1998), the motion of the cylindrical flux tube rising by its magnetic buoyancy is described as

$$I\rho \frac{dV_z}{dt} = -\Delta\rho g - C_D \frac{\rho|V_z|V_z}{\pi R}, \quad (4.15)$$

where  $I$  is the enhanced inertia factor ( $\sim 2$ ),  $C_D$  is the drag co-efficient of order unity, and  $\Delta\rho = \rho_i - \rho$  is the density difference between the flux tube ( $\rho_i$ ) and the external medium ( $\rho$ ). From Equation (4.15), one can calculate the rising velocity of the tube  $V_z(t)$  and the height of the tube center  $z(t)$ . We consider the effect of the mass pile-up between the flux tube and the photosphere and replace  $\Delta\rho$  with an additional effect as

$$\begin{aligned} \Delta\rho' &= \Delta\rho + F\Delta\rho_{\text{acm}} \\ &= \rho_i - \rho + F [\bar{\rho}_{\text{acm}}(0) - \bar{\rho}_{\text{acm}}(t)]. \end{aligned} \quad (4.16)$$

Here,

$$\bar{\rho}_{\text{acm}}(0) = \frac{1}{z_{\text{ph}} - z(0)} \int_{z(0)}^{z_{\text{ph}}} \rho_s(\zeta) d\zeta \quad (4.17)$$

is the plasma on the flux tube in the initial state ( $z_{\text{ph}} = 0$ ,  $z(0) = z_{\text{tube}} = -100H_0$ , and  $\rho_s(z)$  is given by Equation (4.7)), and

$$\bar{\rho}_{\text{acm}}(t) = \frac{1}{z_{\text{ph}} - z(t)} \int_{z(t)}^{z_{\text{ph}}} \rho_s(\zeta) d\zeta \quad (4.18)$$

is the background plasma at a given time. That is,  $\Delta\rho_{\text{acm}} = \bar{\rho}_{\text{acm}}(0) - \bar{\rho}_{\text{acm}}(t)$  corresponds to a density that would have been accumulated by an ideal rising sheet extending horizontally. To consider the effect of the tube's shape and the draining of the plasma

from the apex, we multiply it by a factor  $F (< 1)$ , which depends on the field geometry and its initial depth from the surface ( $R_{\text{tube}}$  and  $z_{\text{tube}}$ ). In the present study, we vary  $F$  to fit the analytic model to the obtained data and assume it as a constant. Defining the relation between  $F$  and  $R_{\text{tube}}$  and  $z_{\text{tube}}$  requires much work, which we shall leave for future research. Applying  $\Delta\rho'$  and dividing Equation (4.15) by  $\rho$ , we get

$$I \frac{dV_z}{dt} = -\frac{\Delta\rho'}{\rho} g - \frac{C_D}{\pi R} |V_z| V_z . \quad (4.19)$$

If pressure balance, mass and flux conservation, and adiabatic evolution are assumed, the buoyancy and the radius of the model tube can be defined as

$$-\frac{\Delta\rho'}{\rho} g = \left( -\frac{\Delta\rho}{\rho} g \right)_{z=z_{\text{tube}}} \left[ \frac{(\Gamma + 1) - z/H_0}{(\Gamma + 1) - z_{\text{tube}}/H_0} \right]^{\Gamma-1} + F \frac{\Delta\rho_{\text{acm}}}{\rho} , \quad (4.20)$$

$$R(z) = R(z = z_{\text{tube}}) \left[ \frac{(\Gamma + 1) - z/H_0}{(\Gamma + 1) - z_{\text{tube}}/H_0} \right]^{\Gamma/2} , \quad (4.21)$$

where  $\Gamma = 1/(\gamma - 1)$ . Here we use their initial values obtained as

$$\left( -\frac{\Delta\rho}{\rho} g \right)_{z=z_{\text{tube}}} = \frac{\iint (-\Delta\rho/\rho) g B_x dy dz}{\iint B_x dy dz} , \quad (4.22)$$

and

$$R(z = z_{\text{tube}}) = \left[ \frac{\iint [(y - y_{\text{tube}})^2 + (z - z_{\text{tube}})^2] B_x dy dz}{\iint B_x dy dz} \right]^{1/2} \quad (4.23)$$

(see Fan et al., 1998). We can calculate the time evolution of the model tube by integrating Equation (4.19).

In Figure 4.6(a), the variation of the rise speed at the tube center is presented in comparison with the analytic model (the dotted line is for the model by Fan et al. (1998) using  $\Delta\rho$  and the solid line for our model using  $\Delta\rho'$ ), while the heights of the tube centers of

the numerical and the analytic model are indicated in Figure 4.6(b). We use  $C_D = 2.0$  and  $F = 0.001$ . In Figure 4.6(a), the solid curve levels off after  $t/\tau_0 = 100$ . This means that the wake develops from this time and the drag force becomes more efficient. Parker (1975) analytically calculated the terminal velocity of the rising. Considering Equation (4.15) = 0 and using Equations (4.22) and (4.23), the terminal velocity can be obtained as

$$V_{z\text{ term}} = \left[ -\frac{\Delta\rho}{\rho} g \frac{\pi R}{C_D} \right]^{1/2} = 0.14 C_{s0}, \quad (4.24)$$

which is rather a good estimation. In the earlier phase ( $t/\tau_0 < 400$ ), the torsional oscillation due to the differential buoyancy is seen in Figure 4.6(a), which was mentioned in §4.3.1.

After  $t/\tau_0 = 500$ , the rising flux tube decelerates as the mass on the tube is compressed and piles up, since the mass cannot persist through the convectively stable surface. This deceleration indicates that, before  $t/\tau_0 = 500$ , the cross-sectional evolution as a whole can be regarded as radial, although the tube suffers aerodynamic deformation; after that time, however, the mass pile-up becomes much more efficient so that the tube decelerates and the apex expands horizontally to become  $\nabla$ -shaped (see the solid and the dotted line in Figure 4.6(a)).

Figure 4.7 shows the density accumulation  $[\rho(t) - \rho_s]/\rho_0$ , where  $\rho_s$  is the initial background density profile (see Equation (4.7)), and the field lines with velocity vectors at the time  $t/\tau_0 = 600$ . It reveals that, because of the relative mass draining from the apex of the tube to the flanks, the density piles up only at a stagnation point in front of the rising tube around  $(y/H_0, z/H_0) = (0, -12)$ . The thickness of the stagnation is  $\delta \sim 2H_0$ . In the imaginary sheet case, however, the fluid would pile up on the rising sheet as a boundary layer with an infinite width, since there is no draining (see Chapter 3). Therefore, the factor  $F$  (the ratio of the actual accumulation to the imaginary one) becomes relatively small.

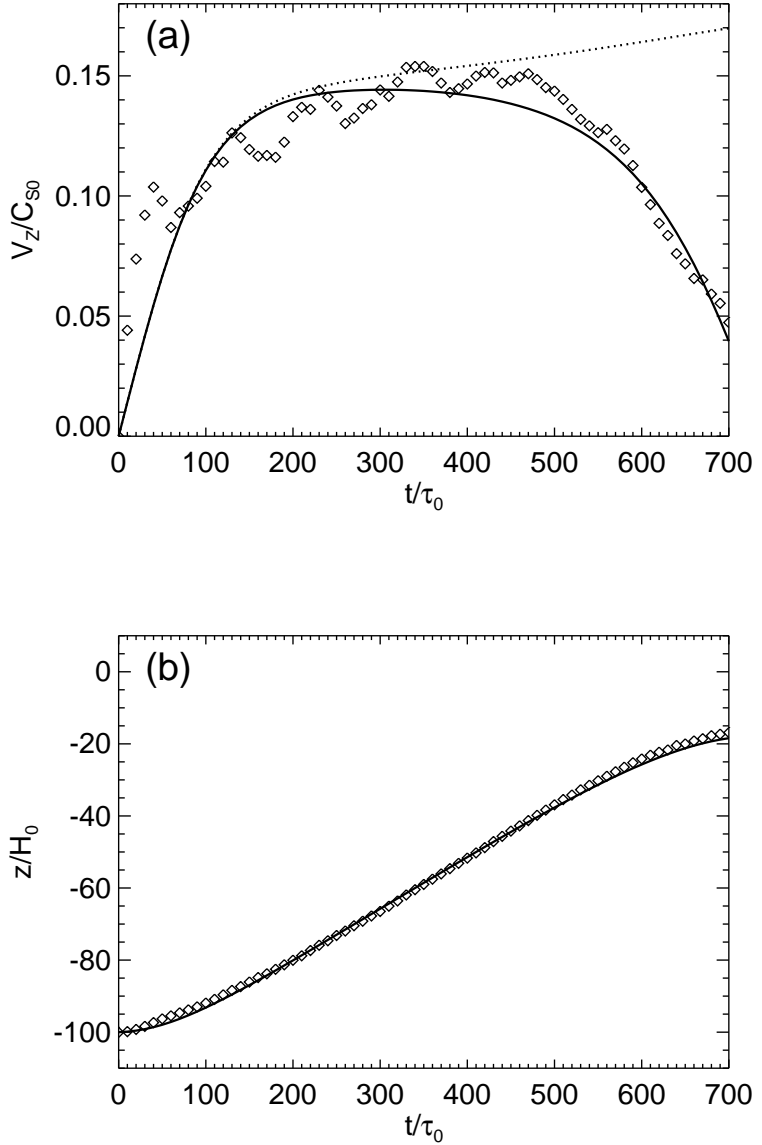


Figure 4.6: (a): The variation of rise velocity of the rising flux tube with time. Diamonds indicate the result of the numerical simulation. Solid line shows our analytic model, while dotted line represents the model by Fan et al. (1998). (b): Height-time relation of the numerical results (diamonds) and the analytic model (solid line). We use  $C_D = 2.0$  and  $F = 0.001$ .

Table 4.1: Summary of Cases

Case	$B_{\text{tube}}$ (300 G) <sup>a</sup>	$R_{\text{tube}}$ (200 km) <sup>b</sup>	$q$ (0.005 km <sup>-1</sup> ) <sup>c</sup>
1	50	5	0.10
2	50	5	0.20
3	50	5	0.05
4	50	5	0.01
5	67	5	0.10
6	33	5	0.10

<sup>a</sup>Magnetic field strength at the tube center.

<sup>b</sup>Tube radius.

<sup>c</sup>Plasma beta at the sheet center.

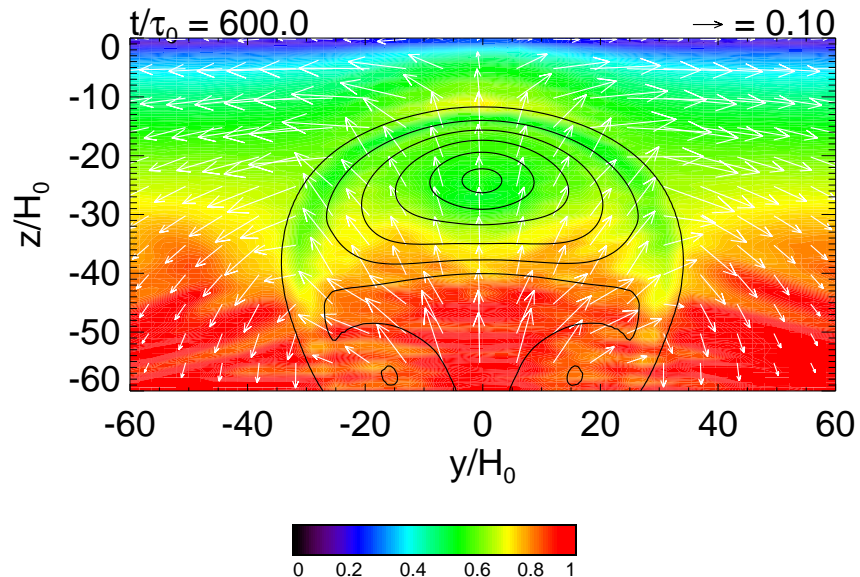


Figure 4.7: The density accumulation  $[\rho(t) - \rho_s]/\rho_0$ , where  $\rho_s$  is the background density profile, and the field lines (contours) with velocity vectors (white arrows) at the time  $t/\tau_0 = 600$  are shown. As the tube rises, the mass piles up in front of the flux tube  $(y/H_0, z/H_0) = (0, -12)$ .

From Figure 4.7, we can estimate the order of  $F$ . The actual mass pile-up along the symmetric axis  $y/H_0 = 0$  is

$$\begin{aligned}\Delta\rho_{\text{sim}} &= \frac{1}{z_{\text{ph}} - z_{\text{apex}}(600\tau_0)} \int_{z_{\text{apex}}(600\tau_0)}^{z_{\text{ph}}} [\rho(600\tau_0) - \rho_s] d\zeta \\ &= 0.73\rho_0,\end{aligned}\quad (4.25)$$

where  $z_{\text{apex}}(600\tau_0) = -12H_0$  is the height of the apex of the tube at  $t = 600\tau_0$  (see Figure 4.7). On the other hand, the density enhancement in front of the imaginary emerging sheet at this time can be estimated from the background profile  $\rho_s(z)$  as

$$\begin{aligned}\Delta\rho_{\text{acm}} &= \bar{\rho}_{\text{acm}}(0) - \bar{\rho}_{\text{acm}}(600\tau_0) \\ &= \frac{1}{z_{\text{ph}} - z(0)} \int_{z(0)}^{z_{\text{ph}}} \rho_s(\zeta) d\zeta - \frac{1}{z_{\text{ph}} - z(600\tau_0)} \int_{z(600\tau_0)}^{z_{\text{ph}}} \rho_s(\zeta) d\zeta \\ &= 96.1\rho_0,\end{aligned}\quad (4.26)$$

where  $z(600\tau_0) = -25H_0$  is the height of the tube's center at  $t = 600\tau_0$  (see Figure 4.6(b)). Therefore, we can see that the order of the factor  $F$  is

$$F = \frac{\Delta\rho_{\text{sim}}}{\Delta\rho_{\text{acm}}} = \frac{0.73\rho_0}{96.1\rho_0} = 0.007 = O(10^{-2}).\quad (4.27)$$

Here, we consider the density accumulation only along the axis  $y/H_0 = 0$  in Equation (4.25). The factor  $F$  would be of the order  $10^{-3}$  if we take it into account that the accumulation in the neighboring region is less than that along  $y/H_0 = 0$  due to mass draining.

The effective Reynolds number of the present calculation can be obtained from Figure 4.7 as

$$\text{Re} = \left(\frac{L}{\delta}\right)^2 = \left(\frac{30H_0}{2H_0}\right)^2 \sim 200,\quad (4.28)$$

where  $L$  is the tube's scale (i.e. radius) and  $\delta$  is the thickness of the mass pile-up near the apex  $(y/H_0, z/H_0) = (0, -12)$ . The expected Reynolds number based on the turbulent

convection in the Sun is

$$\text{Re} = \frac{UL}{\nu} = \frac{1 \text{ km s}^{-1} \times 1000 \text{ km}}{10^{12} \text{ cm}^2 \text{ s}^{-1}} = 10, \quad (4.29)$$

where  $U$  and  $L$  is the rising speed and the radius of the tube, respectively, and  $\nu \sim 10^{12} \text{ cm}^2 \text{ s}^{-1}$  is eddy viscosity (Miesch, 2005). That is, the density accumulation and the consequent deceleration of the rising flux tube may occur in the actual solar interior.

By varying  $F$  to fit the analytic model to the obtained data and plotting the density pile-up in the interior, we can conclude that the deceleration of the tube is caused by the accumulation of the plasma ahead of the tube. Fan et al. (1998) and Cheung et al. (2006) also reported this deceleration. However, their calculations did not include the convectively stable photosphere but assumed the non-penetrating or closed top boundaries, which are reasonable approximations for the photosphere compared to our simulation.

### 4.3.3 Further Evolution to the Corona

After  $t/\tau_0 = 800$ , the second-step emergence from the surface to the corona occurs due to the magnetic buoyancy instability (Figures 4.2(f)-(i)). Figure 4.8(a) shows the vertical distribution of magnetic and gas pressure, and density along the symmetric axis  $y/H_0 = 0$  at  $t/\tau_0 = 800$ , i.e., just before the secondary evolution starts. As can be seen from this figure, the site of the second-step evolution has a top heavy structure, and there is a relative “pressure hill,” which is consistent with preceding studies (Magara, 2001; Archontis et al., 2004).

To confirm that further evolution is caused by the magnetic buoyancy instability, we conduct the criterion by Acheson (1979) for magnetic buoyancy instability of a flat magnetized atmosphere (Archontis et al., 2004; Murray et al., 2006; Moreno-Insertis, 2006):

$$-H_0 \frac{\partial}{\partial z} (\log B) > -\frac{\gamma}{2} \beta \delta + (k_{\parallel} H_0)^2 \left( 1 + \frac{k_{\perp}^2}{k_z^2} \right), \quad (4.30)$$

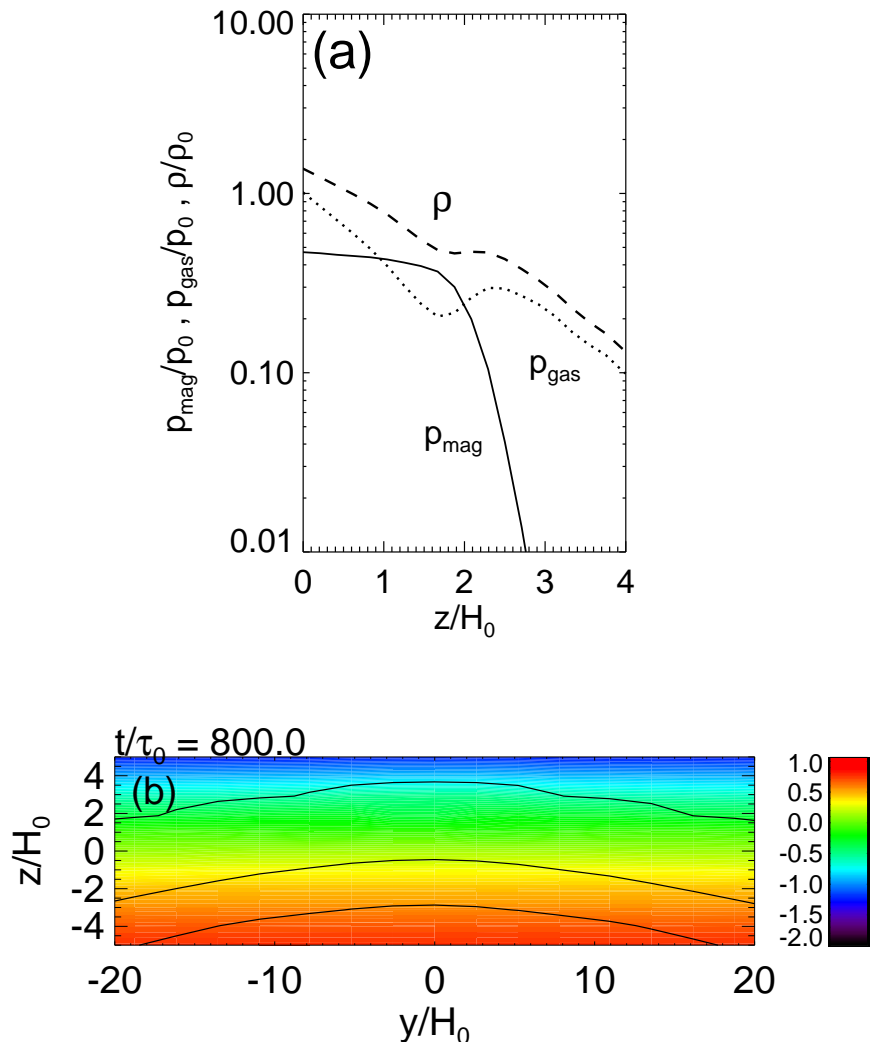


Figure 4.8: (a): Vertical distributions of the magnetic pressure (solid line), gas pressure (dotted line), and gas density (dashed line) along the axis  $y/H_0 = 0$  at  $t/\tau_0 = 800$ . (b): An expanded view of Figure 4.2(f). Density  $\log_{10}(\rho/\rho_0)$  and the azimuthal field lines around  $y/H_0 = z/H_0 = 0$  are indicated.

where  $\delta = \nabla - \nabla_{\text{ad}}$  is the superadiabaticity,  $\nabla$  the logarithmic temperature gradient and  $\nabla_{\text{ad}}$  its adiabatic value, and  $k_{\parallel}$  and  $k_{\perp}$  are the wavenumbers of the perturbation in the two horizontal directions parallel and perpendicular to the magnetic field, respectively. Here,  $k_{\perp} = 0$ , because  $B_x \ll B_y$  near the surface. Now the condition for the magnetic buoyancy instability is

$$(k_{\parallel} H_0)^2 < -H_0 \frac{\partial}{\partial z} (\log B) + \frac{\gamma}{2} \beta \delta . \quad (4.31)$$

From the data obtained by the simulation, we get the condition for  $k_{\parallel}$ :

$$k_{\parallel} < 0.855/H_0 \equiv k_{\parallel\max} . \quad (4.32)$$

Figure 4.8(b) shows the expanded view of field lines and the density field near the surface at  $t/\tau_0 = 800$ . As can be seen from this figure, the wavelength of the perturbation is  $\lambda_{\parallel} \simeq 20H_0$ . That is, the wavenumber  $k_{\parallel} = 2\pi/\lambda_{\parallel} \simeq 0.314/H_0$  is less than  $k_{\parallel\max}$ . Thus, we can conclude that the plasma around the surface is magnetic buoyancy-unstable. At this site, the magnetic field intensity amounts to  $\sim 1$  kG, and the plasma beta is  $\beta \sim 2$ .

In the upper atmosphere above the surface, the azimuthal component of the magnetic field is very dominant. The second-step nonlinear evolution develops in a self-similar way; the expansion law was given by Shibata et al. (1989). It can be described as follows:

$$V_z/C_{s0} = az/H_0 , \quad (4.33)$$

$$\rho \propto z^{-4} , \quad (4.34)$$

and

$$|B_y| \propto z^{-1} , \quad (4.35)$$

where  $a \sim 0.05$  when plasma- $\beta$  is 0.5–2.0. The above relations are plotted in Figure 4.9 for  $t/\tau_0 = 850, 870$ , and  $890$ . In Figure 4.9(a), we use  $a = 0.04$ , which is appropriate because plasma- $\beta$  was  $\sim 2$  at the point of the further evolution ( $z \sim 0$  at the time  $t/\tau_0 = 800$ ).

In the final phase, at  $t/\tau_0 = 980$ , the coronal loop is formed with  $400H_0 = 80,000$  km in width and  $200H_0 = 40,000$  km in height (see Figure 4.2(i)). The size of the loop is similar to that of the case with a flux sheet (Chapter 3). The photospheric field strength is (400–700) G at this time.

## 4.4 Dependence on the Initial Twist and the Field Strength

We carry out five additional calculations to investigate the dependence of the tube's evolution on the twist and the field strength. These runs are summarized in Table 4.1. Parametric surveys on the twist and the field strength have been done by Moreno-Insertis & Emonet (1996), Emonet & Moreno-Insertis (1998), Magara (2001), Murray et al. (2006), and Murray & Hood (2008). They found that the tube rises faster as the twist and the field become stronger.

Figure 4.10 shows the result of the parameter survey on the tube twist. In this figure, height-time relations of the tube tops are shown. In cases of a weaker twist ( $q = 0.01/H_0$  and  $0.05/H_0$ ), the flux tube shows “failed emergence.” That is, the rising flux cannot pass through the photosphere. The criterion for this failure is  $q \lesssim 0.05/H_0$ . In Chapter 3, we found that, when the initial field strength or the total magnetic flux is too weak, the resulting development also reveals “failed” evolution. Figure 4.11 shows the flux tubes with different initial twist when each tube center reaches  $z/H_0 = -50$ . From left to right, the twist parameter decreases. The upper panels present the flow field relative to the tube apex,  $\mathbf{V}_{\text{rel}} = \mathbf{V} - \mathbf{V}_{\text{apex}}$ , and the corresponding equipartition line. The equipartition

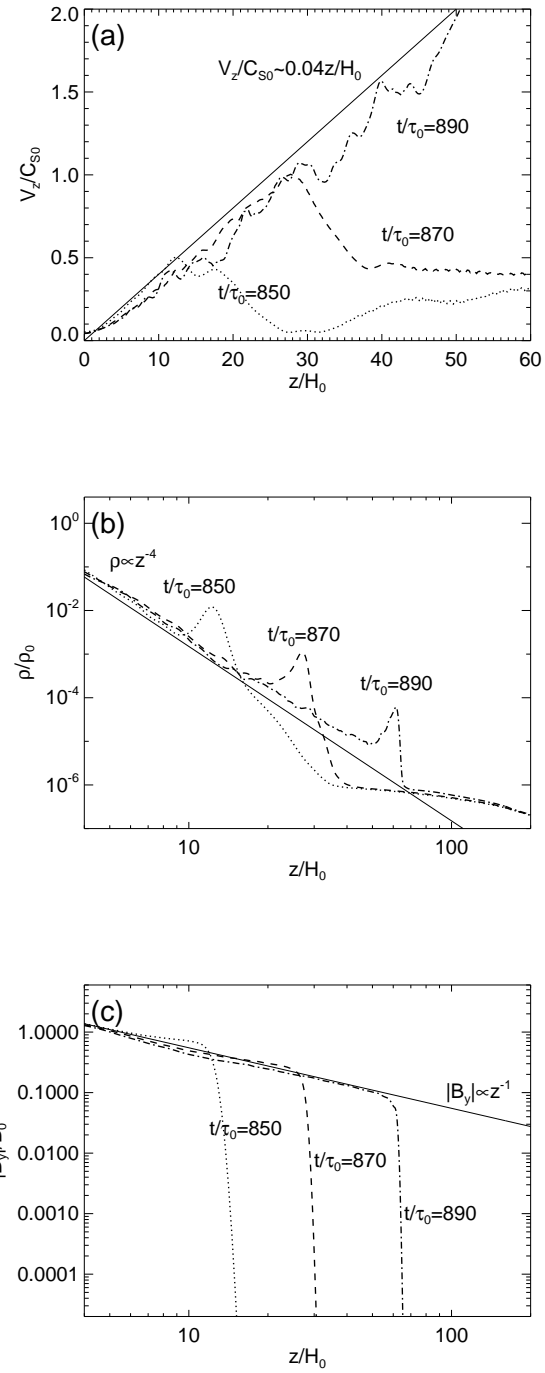


Figure 4.9: (a): Distribution of the upward velocity along the vertical axis  $y/H_0 = 0$ . Dotted, dashed, and dash-dotted lines indicate the distribution at  $t/\tau_0 = 850, 870$ , and  $890$ , respectively. The solid line shows the theoretical velocity-height relation according to Shibata et al. (1989). (b): Distribution of the gas density. (c): Distribution of the horizontal component of the magnetic field.

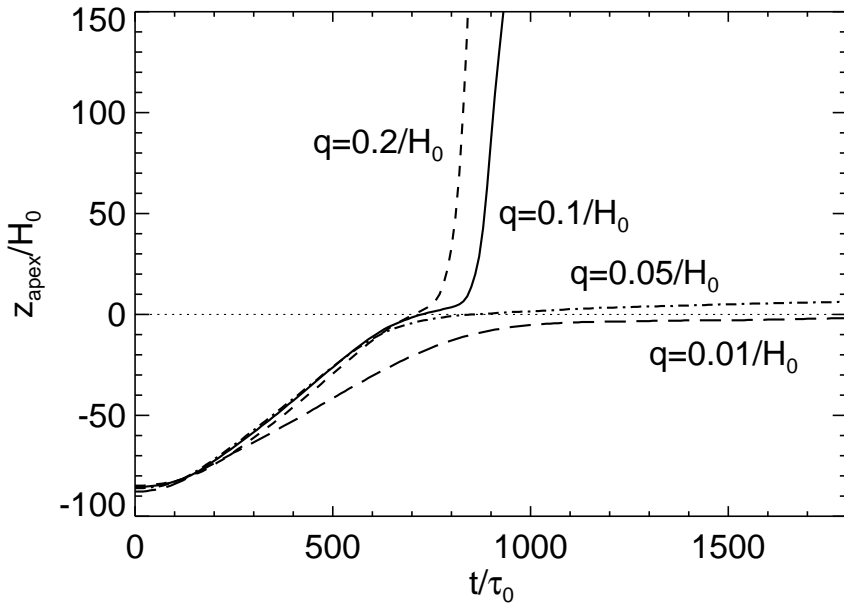


Figure 4.10: Height-time relation of the top of the flux tube. Dashed, solid, dash-dotted, and long dashed lines represent cases for  $q = 0.2/H_0$ ,  $0.1/H_0$ ,  $0.05/H_0$ , and  $0.01/H_0$ , respectively. Dotted line indicates the photospheric level.

line indicates the tube boundary where the kinetic energy density of the relative flow  $e_{\text{kin}} = \rho V_{\text{rel}}^2/2$  equals the energy density of the azimuthal field  $e_{\text{mag}} = B_\phi^2/(8\pi)$ . The lower panels show the longitudinal field strength  $B_x$  and the flow field  $\mathbf{V}$ . As can be seen from Figure 4.11, with a decreasing twist, the main tube is deformed by the external flow and the wake develops. In cases of a weaker twist, the counter-rotating vortices contain a large portion of the magnetic flux. Thus, when the tube reaches the surface, the apex of the tube cannot hold sufficient flux for the further evolution, which leads to “failed emergence.” The situation can also be explained as follows; when the initial twist is weak, the flux tube expands and extends very widely beneath the surface. Thus, the magnetic buoyancy falls short of compressing the flux to satisfy the criterion (4.30) for the second-step emergence. In Figure 4.12, we show the distribution near the surface for the case  $q = 0.05/H_0$  at the time  $t/\tau_0 = 1000$ . Figure 4.12(a) plots the magnetic pressure, the gas pressure, and the density along the symmetric axis  $y/H_0 = 0$ . The subsurface magnetic field is not fortified enough so that the magnetic pressure is much

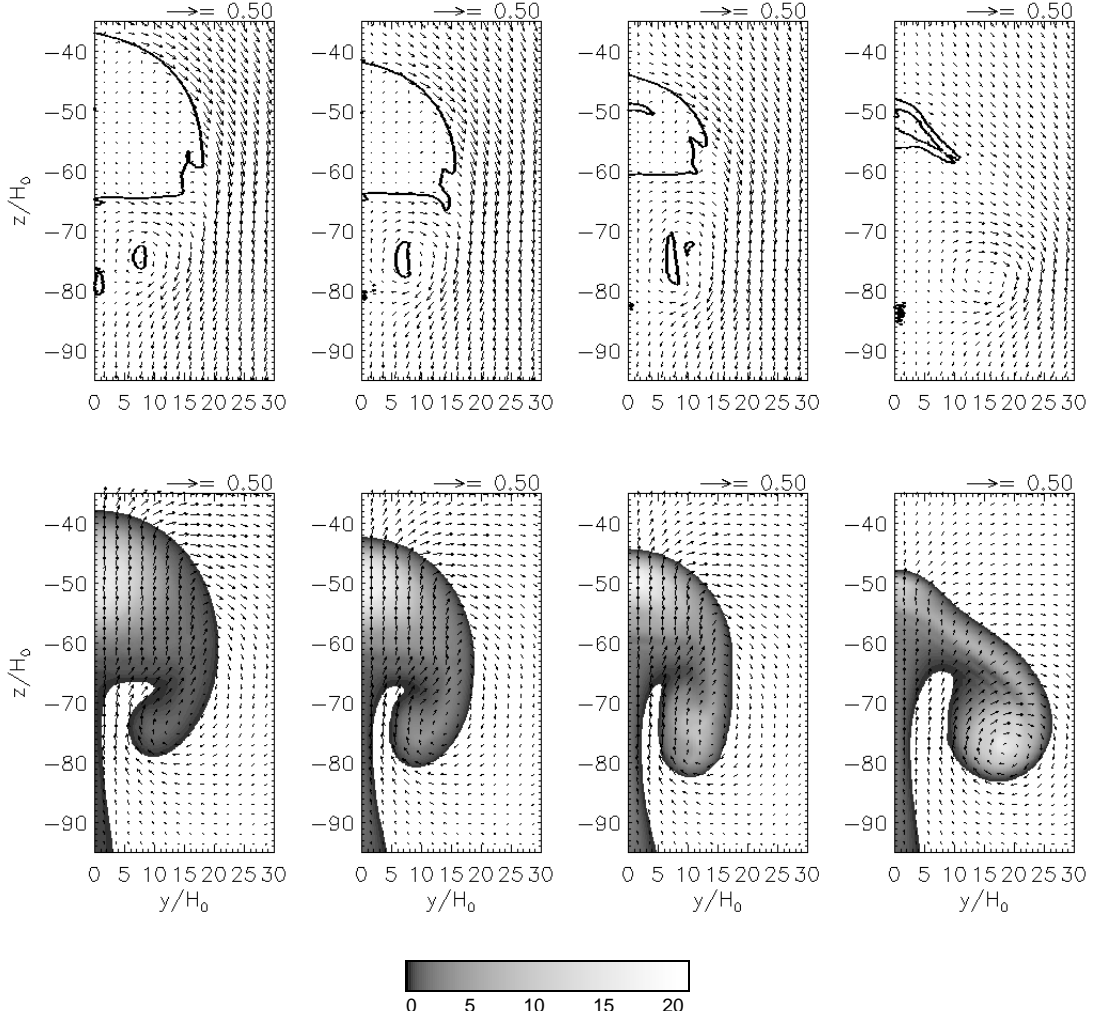


Figure 4.11: Cross-section of the flux tubes with different initial twist when their centers are at  $z/H_0 = -50$ . From left to right, the twist parameters and their corresponding times are  $q = 0.2/H_0, 0.1/H_0, 0.05/H_0$ , and  $0.01/H_0$ , and  $t/\tau_0 = 460, 410, 390$ , and  $450$ , respectively. *Top:* The velocity relative to the apex of the tube and the equipartition line (see text for details). *Bottom:* The longitudinal magnetic field strength and the flow fields.

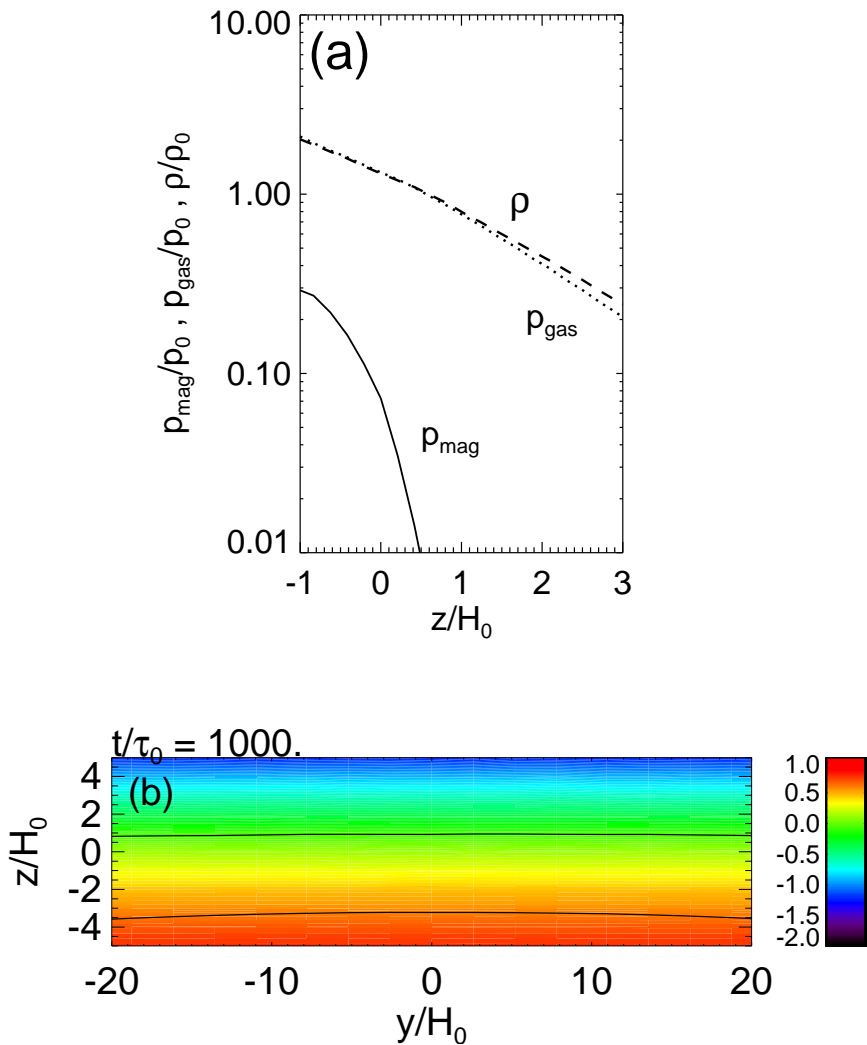


Figure 4.12: The plots for the case with  $q = 0.05/H_0$  at  $t/\tau_0 = 1000$ . (a): Vertical distributions of the magnetic pressure (solid line), gas pressure (dotted line), and gas density (dashed line) along the axis  $y/H_0 = 0$ . (b): Density  $\log_{10}(\rho/\rho_0)$  and the field lines near the surface.

smaller than the plasma pressure. Figure 4.12(b) shows the field lines and the density near the surface. The wavelength of the perturbation is  $\lambda_{\parallel} \rightarrow \infty$ , i.e., the wavenumber ( $k_{\parallel} \rightarrow 0$ ) does not satisfy the criterion (4.32). It means that the further evolution to the solar corona due to the magnetic buoyancy instability does not take place in this weaker twist case.

Figure 4.13 shows the height-time relations for the cases with  $B_{\text{tube}} = 67B_0$ ,  $50B_0$ , and  $33B_0$ , which are indicated with dashed, solid, and dash-dotted lines. We can conclude

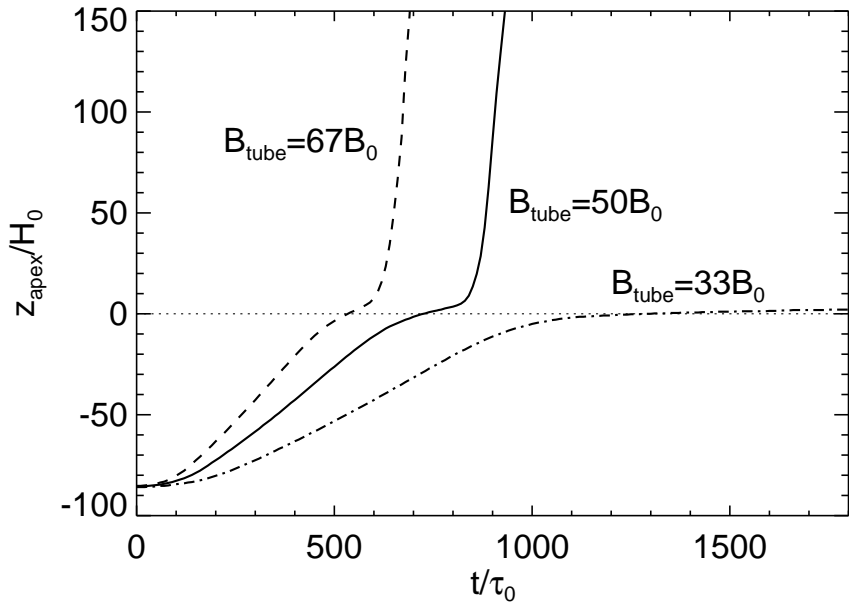


Figure 4.13: Height-time relation of the top of the flux tube. Dashed, solid, and dash-dotted lines represent cases for  $B_{\text{tube}} = 67B_0$ ,  $50B_0$ , and  $33B_0$ , respectively. Dotted line indicates the photospheric level.

from this figure that the rise speed is faster with the stronger field. As is the case with the dependence on the twist, we can say that, if the initial field is too weak, the rise speed is slower and the flux tube cannot pass through the surface to rise further into the corona. The general tendency of the parametric studies varying the tube's twist and the strength is consistent with previous two- and three-dimensional experiments (Moreno-Insertis & Emonet, 1996; Emonet & Moreno-Insertis, 1998; Magara, 2001; Murray et al., 2006;

Murray & Hood, 2008).

## 4.5 Summary and Discussion

The numerical experiments studied in this Chapter are on the cross-sectional evolution of the emerging twisted flux tube. In this Section, we summarize the calculations presented above and discuss the results. The discussions are mainly in connection with Chapter 3. We can predict the conditions for three-dimensional experiments by considering the results of the present and previous two-dimensional studies. So, in this Section, we discuss the two-dimensional results in connection with our future three-dimensional experiments.

In this Chapter, we have studied the dynamical evolution of the twisted flux tube that emerged from the deep convection zone. For the typical case, the initial flux tube is located at  $z = -100H_0 = -20,000$  km with the axial field strength  $B_{\text{tube}} = 50B_0 = 1.5 \times 10^4$  G, the tube radius  $R_{\text{tube}} = 5H_0 = 1000$  km, and the total magnetic flux  $\Phi = 4.7 \times 10^{20}$  Mx. The tube is initially buoyant and, thus, begins to rise through the convection zone. Halfway to the surface, after  $t = 100\tau_0 = 2500$  s, the periphery of the tube is peeled away to develop a wake, composed of vortex rolls and a long-drawn tail, due to the external flow from the apex to the flanks. As a result, the aerodynamic drag becomes more effective. However, the azimuthal field prevents the flux tube from being fragmented into a pair of counter-rotating vortices moving away from each other, so that the expansion as a whole can be said to be radial. The picture of the emergence within the convective layer is similar to previous papers (e.g. Moreno-Insertis & Emonet, 1996).

The essential difference from these preceding studies is the effect of the convectively stable photosphere; the apex of the tube expanding horizontally and the rising motion turning into the deceleration after  $t = 500\tau_0 = 1.3 \times 10^4$  s, because the rising tube comes close to the photosphere. The deceleration occurs at a depth ten times deeper than previously reported by Magara (2001); the deceleration depth is  $\sim -500$  km in Magara's case, while it is  $\sim -5000$  km in our case, which shows that the flux tube slows down

before the tube itself reaches the surface. It also indicates that there is another mechanism that accounts for the slowdown other than the tube itself entering the photosphere. The plasma on the flux tube piles up between the flux and the convectively stable surface, and depresses the flux below. We confirmed this effect by comparing the numerical result with an extended analytic model (see Section 4.3.2). As a result, the  $\nabla$ -shaped emerging flux extends widely beneath the surface ( $\sim 40,000$  km in width). In this stage, the azimuthal field component is dominant, since the twist of the flux tube increases as the tube rises. When the horizontal flux at the photosphere becomes unstable to the magnetic buoyancy instability at  $t = 800\tau_0 = 2.0 \times 10^4$  s, the second-step emergence to the corona takes place (“two-step emergence”). The evolution above the surface is similar to that of Magara (2001). The nonlinear evolution is well described by the expansion law given by Shibata et al. (1989). The consequent coronal loop at  $t = 980\tau_0 = 2.5 \times 10^4$  s has its width  $\sim 400H_0 = 80,000$  km and height  $\sim 200H_0 = 40,000$  km, and the photospheric field is  $(1.3\text{--}2.3)B_0 = (400\text{--}700)$  G.

By performing parameter studies, we found that the initial twist necessary for the further evolution is  $q > 0.05/H_0 = 2.5 \times 10^{-4}$  km $^{-1}$  when the axial field  $B_{\text{tube}} = 50B_0 = 1.5 \times 10^4$  G. If  $q$  is less than this value, the emerging tube remains within the convection zone (“failed emergence”). We also found that the flux with a weaker field strength shows the failed emergence. When the tube twist is  $q = 0.1/H_0 = 5.0 \times 10^{-4}$  km $^{-1}$ , the flux with  $B_{\text{tube}} = 33B_0 = 1.0 \times 10^4$  G cannot rise further above the surface.

In Chapter 3, we carried out numerical experiments on the two-dimensional undular evolution of the flux sheet from the deep convection zone ( $z = -20,000$  km). We found that the emerging flux sheet also decelerates in the convection zone. However, deceleration depth is deeper than that of the present study. Table 4.2 summarizes the characteristic values of both types of emergence. As seen from Table 4.2, the initial conditions (the field strength, the total magnetic flux, the sheet thickness and the tube radius, and the depth) are similar to each other, while the obtained values concerning the evolutions in the convection zone (the arrival time at the photosphere and the deceleration depth) are different.

Table 4.2: Comparison of the Two Types of the Flux Emergence

Characteristic Variables	Undular Emergence of Flux Sheet <sup>a</sup>	Non-equilibrium Emergence of Twisted Flux Tube <sup>b</sup>
Initial Field Strength	$1.0 \times 10^4$ G	$1.5 \times 10^4$ G
Total Magnetic Flux	$1.0 \times 10^{21}$ Mx	$4.7 \times 10^{20}$ Mx
Sheet Thickness/Tube Radius	100 km	1000 km
Initial Depth	-20,000 km	-20,000 km
Arrival Time at the Surface	$4.9 \times 10^4$ s	$2.0 \times 10^4$ s
Deceleration Depth	-10,000 km	-5000 km

<sup>a</sup>Typical case of Chapter 3.

<sup>b</sup>Typical case of this Chapter (twist  $qH_0 = 0.1$ ).

That is, the twisted flux tube rises faster than the flux sheet and the deceleration occurs at a higher altitude. The difference between the two cases comes from the geometry of the emerging fluxes, i.e., a sheet or a tube. The plasma on the emerging flux tube can flow around the tube's cross-section so that the tube rises faster. The fluid on the flux sheet, however, drains only along the magnetic field lines to both troughs, so that the plasma suppresses and slows down the rising sheet below halfway to the surface. As for the twisted flux tube, the deceleration occurs in the later phase when the tube itself approaches the surface and begins to expand horizontally (see §4.3.1 and §4.3.2). It should be noted that, in the initial state, the flux sheet is in hydrostatic equilibrium while the flux tube is in mechanically non-equilibrium. In addition, the mass draining along the longitudinal field line is not considered in the present tube calculation. Three-dimensional experiments are required to investigate these effects.

By conducting the parameter survey, we found that the emerging flux tube cannot rise further if the initial twist is too weak (“failed” case), because the weak azimuthal field cannot hold the tube's coherency and thus cannot hold the field intensity necessary for the second-step emergence. Such a flux remains below the surface and floats around the solar interior. The condition for the “two-step emerging” flux tube that yields a realistic active region at the surface is  $B_{\text{tube}} \gtrsim 50B_0 = 1.5 \times 10^4$  G with  $q \gtrsim 0.1/H_0 = 5.0 \times 10^{-4} \text{ km}^{-1}$

at  $z = -100H_0 = -20,000$  km. In Chapter 3, it was also found that there is a threshold of the flux sheet strength and the total flux for further emergence. That is to say, the emerging flux with a weak twist also shows “failed emergence” as well as the flux with a weak field strength and an insufficient total flux. If we put these results obtained from the two experiments together, the preferable initial conditions for the three-dimensional calculation using the twisted flux tube from the same depth ( $z = -20,000$  km) are the field strength  $\sim$  a few  $10^4$  G, the total magnetic flux of  $\sim (10^{21}-10^{22})$  Mx, and sufficient twist ( $q > 0.05/H_0 = 2.5 \times 10^{-4}$  km $^{-1}$ ). In future three-dimensional simulations, we will take into account the above mentioned conditions.

The comparison with the results by thin-flux-tube experiments (see §1.3) has been discussed in Chapter 3. In Figure 3.10, the typical case of the present calculation (Case 1 with  $1.5 \times 10^4$  G and  $4.7 \times 10^{20}$  Mx) locates in the middle of the area for the two-step emergence. Moreno-Insertis et al. (1995) found that the magnetic flux tube with weaker field “explodes” within the interior and never reaches the surface; when the pressure gap between inside and outside the initial flux tube is too small, i.e., when the initial magnetic field is too weak, the tube will collapse at a certain height, since the pressure gap decreases. In Chapter 3, we found that the cases showing two-step emergence would have survived the “explosion” during their ascents through the interior. Therefore, we can see that the typical tube (the present Case 1) also would have emerged through the convection zone without “exploding.”



# Chapter 5

## Three-dimensional Experiment

### 5.1 Introduction

In this Chapter, we show a three-dimensional calculation of flux tube emergence from below the photosphere by 20,000 km. In numerical experiments, the multi-dimensionality may cause important effects on the simulation results. In other words, we have neglected some aspects in the previous 2D calculations. In the undular mode evolution (Chapter 3), the initial flux is thought as a horizontal flux sheet extending infinitely. Thus, there is no draining of plasma around the cross-section perpendicular to the field lines, and the plasma easily piles up on the rising flux sheet. As for the cross-sectional evolution (Chapter 4), the tube never bend in the axial direction. Thus, the horizontal tube rises as a whole without the plasma draining downward along the field lines to the both troughs, which makes the tube more buoyant. Also, the restoring magnetic curvature force does not pull down the rising tube. Therefore, as a next step of our study, we have to do a 3D work, which includes all the effects above.

However, the three-dimensional calculation is difficult because of the computational ability. In the previous calculations, both the horizontal and vertical axes took grid points of order 1000, i.e., the total grid was  $\sim 10^6$ . If we take 1000 for each axis of the 3D computational box, the total grid number will be  $\sim 10^9$ . In a large computation, we

also have a problem of analyzing the numerical results. Thus, in order to reduce the grid points, we adopt a nonuniform grid spacing.

As a result of the two-dimensional experiments, we found the condition of the flux tube that yields a realistic active region: the magnetic field strength  $B_{\text{tube}} \gtrsim 50B_0 = 1.5 \times 10^4$  G, the total flux  $\Phi \sim (10^{21}-10^{22})$  Mx, and the twist  $q > 0.05/H_0 = 2.5 \times 10^{-4}$  km<sup>-1</sup> at a depth of 20,000 km. In this calculation, we adopt these values as an initial condition.

The rest of the Chapter proceeds as follows. Section 5.2 shows the numerical setup and Section 5.3 details the results of the calculation. Section 5.4 and Section 5.5 are devoted to discussion and conclusions, respectively.

## 5.2 Numerical Setup

The basic MHD equations used in this Chapter are the same as those in Chapter 2. We take a rectangular computation domain with 3D Cartesian coordinates  $(x, y, z)$ , where  $z$  increases upward.

The initial background atmosphere consists of three gas layers. The bottom layer is an adiabatically stratified convection zone. The middle and the top layers are a cool isothermal photosphere/chromosphere (hereafter, we simply call it photosphere) and the hot isothermal corona, respectively. The two layers are jointed through the transition region with a steep temperature gradient. We take  $z/H_0 = 0$  to be the base of the photosphere, and the initial temperature distribution in the photosphere and the corona ( $z/H_0 \geq 0$ ) is described as

$$T = T_s(z) = T_{\text{ph}} + \frac{1}{2}(T_{\text{cor}} - T_{\text{ph}}) \{\tanh [(z - z_{\text{cor}})/w_{\text{tr}}] + 1\}, \quad (5.1)$$

where  $T_{\text{ph}} = T_0$  and  $T_{\text{cor}} = 100T_0$  are the temperatures in the photosphere and in the corona, respectively, and  $z_{\text{cor}} = 10H_0$  is the base height of the corona, and  $w_{\text{tr}} = 0.5H_0$  is the temperature scale height of the transition region. The initial temperature distribution

in the interior ( $z/H_0 \leq 0$ ) is

$$T = T_s = T_{\text{ph}} - z \left| \frac{dT}{dz} \right|_{\text{ad}}, \quad (5.2)$$

where

$$\left| \frac{dT}{dz} \right|_{\text{ad}} = \frac{\gamma - 1}{\gamma} \frac{mg_0}{k_B} \quad (5.3)$$

is the adiabatic temperature gradient. Here, the subscript “s” represents the surrounding distribution. The initial gas pressure and density profiles are defined by solving one-dimensional hydrostatic equation

$$\frac{d}{dz} p_s(z) + \rho_s g_0 = 0 \quad (5.4)$$

and the equation of state

$$p_s(z) = \frac{k_B}{m} \rho_s(z) T_s(z) \quad (5.5)$$

on the basis of the temperature distribution above.

The initial magnetic flux tube is embedded at  $z_{\text{tube}} = -100H_0 = -20,000$  km. The longitudinal and azimuthal component of the tube is described as, for a radial distance from the axis  $r = [(y - y_{\text{tube}})^2 + (z - z_{\text{tube}})^2]^{1/2}$ ,

$$B_x(r) = B_{\text{tube}} \exp \left( -\frac{r^2}{R_{\text{tube}}^2} \right), \quad (5.6)$$

and

$$B_\phi(r) = qr B_x(r), \quad (5.7)$$

where  $(y_{\text{tube}}, z_{\text{tube}}) = (0, -100H_0)$  is the tube center,  $B_{\text{tube}}$  the field strength at the axis,

$R_{\text{tube}}$  the radius,  $q$  the twist intensity. We take  $B_{\text{tube}} = 67B_0 = 2.0 \times 10^4$  G,  $R_{\text{tube}} = 5H_0 = 1000$  km, and  $q = 0.1/H_0 = 5.0 \times 10^{-4}$  km $^{-1}$  (right-handed), respectively. These values are the same as those of Case 5 in the previous cross-sectional experiment in Chapter 4. Initially, the tube is stable for the kink instability (Linton et al., 1996). The total flux of the axial component is  $\Phi = 6.3 \times 10^{20}$  Mx. For pressure balance between the flux tube and the surrounding medium, the pressure inside the tube is  $p_i = p_s + \delta p_{\text{exc}}$ , where

$$\delta p_{\text{exc}} = \frac{B_x^2(r)}{8\pi} \left[ q^2 \left( \frac{R_{\text{tube}}^2}{2} - r^2 \right) - 1 \right]. \quad (5.8)$$

The density inside is also defined as  $\rho_i = \rho_s + \delta\rho_{\text{exc}}$ , where

$$\delta\rho_{\text{exc}} = \frac{\delta p_{\text{exc}}}{p_s} \rho_s \exp\left(-\frac{x^2}{\lambda^2}\right), \quad (5.9)$$

and  $\lambda/H_0 = 400$ . That is, the flux tube is most buoyant at the middle of the tube ( $x/H_0 = 0$ ), and the buoyancy diminishes as  $|x|$  increases. The initial background distribution of gas pressure, density, and temperature, and the magnetic pressure along the central vertical axis  $x/H_0 = y/H_0 = 0$  are indicated in Figure 5.1. The plasma  $\beta$  at the tube center  $(x, y, z) = (0, 0, -100H_0)$  is  $\sim 38$ .

The simulation domain is taken as  $(-400, -200, -200) \leq (x/H_0, y/H_0, z/H_0) \leq (400, 200, 250)$ . To reduce the total grid point, we adopt nonuniform spacings for each coordinate. The total grid number is  $512 \times 256 \times 1024$ , i.e., of the order of  $10^8$ . The grid spacings for  $x$ ,  $y$ , and  $z$  directions are  $\Delta x/H_0 = \Delta y/H_0 = 0.5$  for  $(-64, -32) \leq (x/H_0, y/H_0) \leq (64, 32)$ , and  $\Delta z/H_0 = 0.2$  for  $-120 \leq z/H_0 \leq 20$ , respectively. Outside this range, the mesh sizes gradually increase. We assume periodic boundaries for both horizontal directions and symmetric for vertical. A wave-damping region is attached near the top boundary.

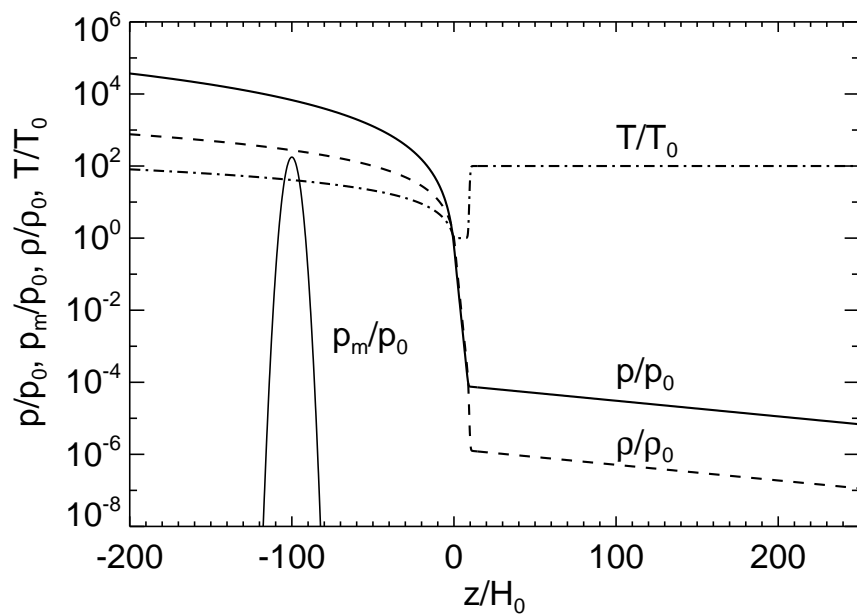


Figure 5.1: One-dimensional ( $z$ -)distributions of the initial background gas pressure (thick solid line), density (dashed line), and temperature (dash-dotted line). The magnetic pressure  $p_m = B^2/(8\pi)$  along the vertical axis  $x/H_0 = y/H_0 = 0$  is overplotted with a thin solid line.

## 5.3 Results

### 5.3.1 General Evolution

Figure 5.2 shows the perspective view of the emerging flux tube. Initially at  $t/\tau_0 = 0$ , the tube is embedded at  $-20,000$  km (Figure 5.2(a)). As the tube rises through the convection zone due to its buoyancy (Figures 5.2(b) and (c)), the cross-section of the tube shows a vortex structure, which is similar to the previous cross-sectional experiment in Chapter 4. On the other hand, the  $(x, z)$ -section shows an arched structure, which is contrary to the trapezoidal structure in the undular evolution of a flux sheet in Chapter 3. It is because the present flux has a tubular form rather than a sheet-like structure. Figure 5.3 shows the height-time relation of the highest part of the flux tube  $z_{\text{apex}}/H_0$ , while the rising velocity  $V_{z_{\text{apex}}}/C_{s0}$  is overplotted. The rising speed increases during the initial phase ( $t/\tau_0 \lesssim 200$ ), and levels off after  $t/\tau_0 = 200$ . As the tube reaches the surface, the rising speed slows down after  $t/\tau_0 = 400$ , and the tube expands sideways in the  $y$ -direction to make a flattened structure beneath the surface. Its apex reveals a wrinkled shape that is caused by the interchange mode instability of the outermost field lines (Figure 5.2(d)). As time goes on, however, the sunk parts of the wrinkled shape become filled with magnetic fields, and eventually this wrinkled shape vanishes (Figure 5.2(e)). It is because the photosphere is convectively stable and the rising tube cannot pass through it.

As the surface field satisfies the criterion for the magnetic buoyancy instability after  $t/\tau_0 = 600$ , the field gradually starts rising again into the upper atmosphere (Figure 5.2(f)). From this figure, we can observe several ( $\sim 4$ ) emerging magnetic domes aligned in the  $x$ -direction, each being directed in the  $y$ -direction. The domes continue growing and merge with each other in the corona (Figure 5.2(g)). After  $t/\tau_0 = 800$ , the rising speed levels off again, and finally the emerging tube reaches  $z/H_0 \sim 40$  at  $t/\tau_0 = 850$ .

The whole evolution can be considered as a “two-step emergence,” which was seen in both undular and cross-sectional evolutions (Chapters 3 and 4).

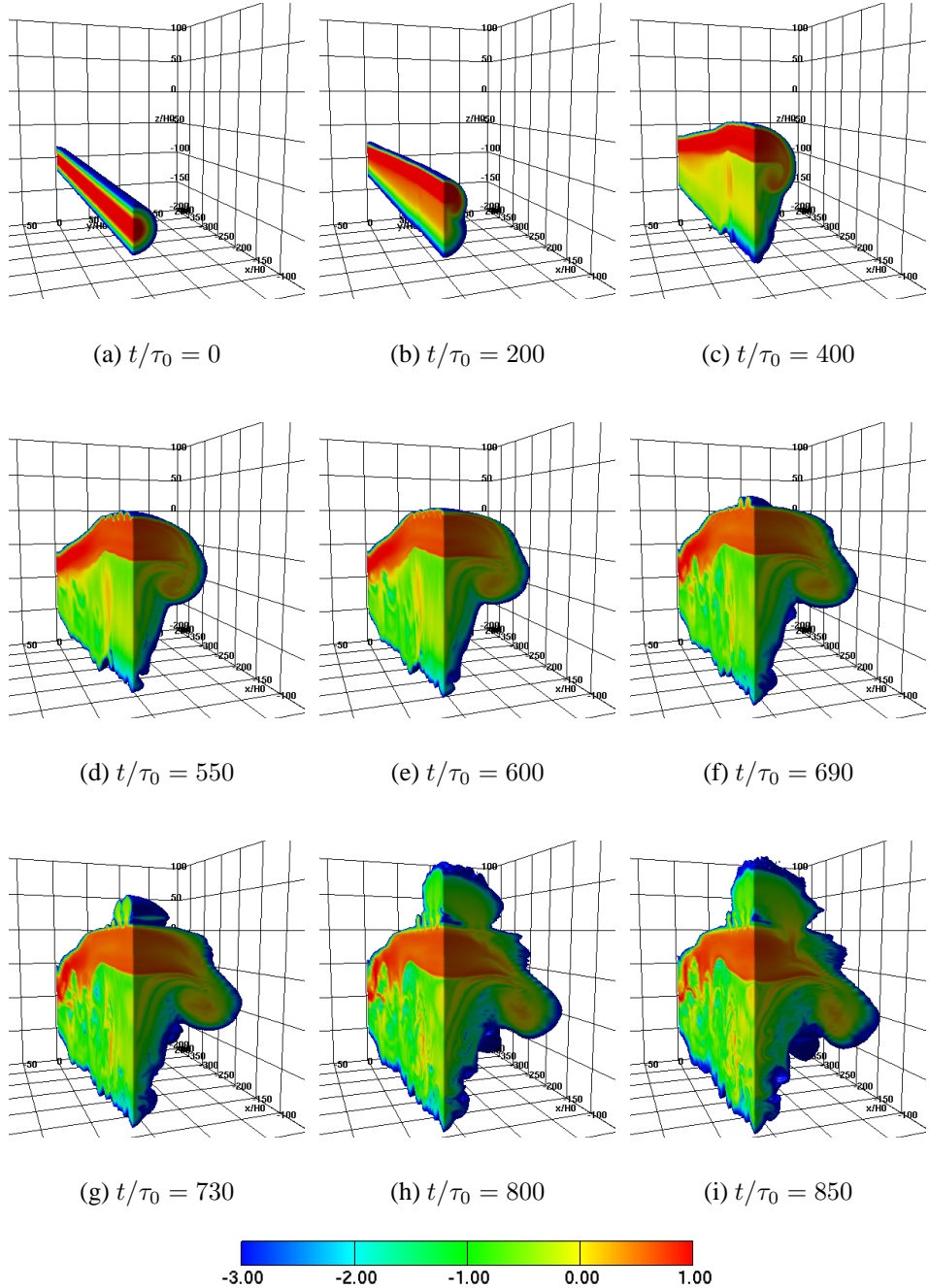


Figure 5.2: Time-evolution of the emerging flux tube. Logarithmic field strength  $\log(|B|/B_0)$  in a limited region ( $x/H_0 \leq 0, y/H_0 \geq 0$ ) is shown.

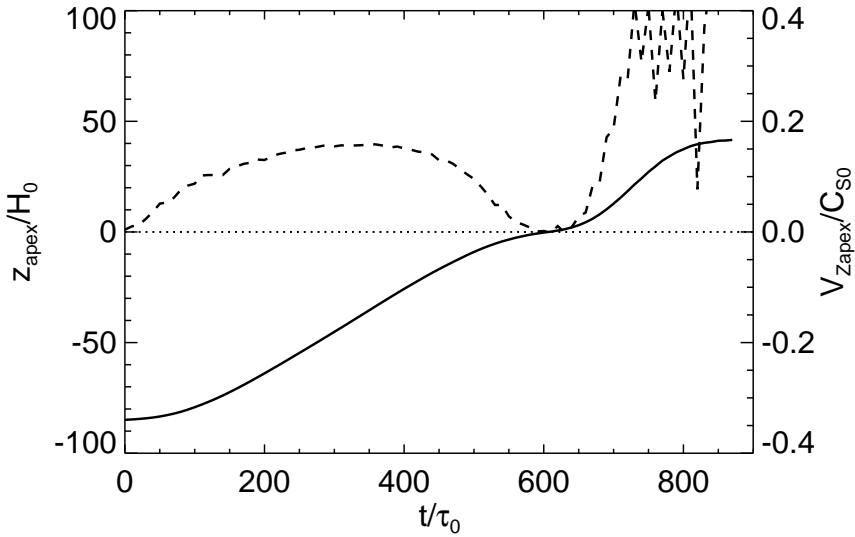


Figure 5.3: The solid line indicates the height-time relation of the apex of the flux tube ( $z_{\text{apex}}/H_0$ ), while its rising speed ( $V_{z_{\text{apex}}}/C_{s0}$ ) is overplotted with the dashed line.

### 5.3.2 Magnetic Structure in the Convection Zone

Figure 5.4 shows the time-evolution of cross-section at  $y/H_0 = 0$ , while Figure 5.5 is the cross-section at  $x/H_0 = 0$ . The  $(x, z)$ -section (Figure 5.4) reveals a symmetrical arched structure rather than a trapezoid of the undular evolution in Chapter 3 (see Figure 3.2). It is because the present flux has a tubular shape instead of a sheet-like structure. In a tube case, the fluid on the rising tube can drain around the cross-section from the apex to the flanks, while the fluid on the horizontal sheet tends to pile up on the rising sheet. Because of this relative draining of the surrounding plasma, the cross-section at  $x/H_0 = 0$  shows a pair of vortex rolls behind the main tube (Figure 5.5). Also, behind the main tube, there is an elongated magnetic tail. These features are similar to those of the cross-sectional evolution in Chapter 4 (see Figure 4.4).

As the tube reaches the surface, the apex becomes fluted due to the interchange instability of the outermost field lines (Figure 5.4(g)). However, this structure vanishes in Figure 5.4(h). Since the photosphere is isothermal, i.e., convectively stable against the

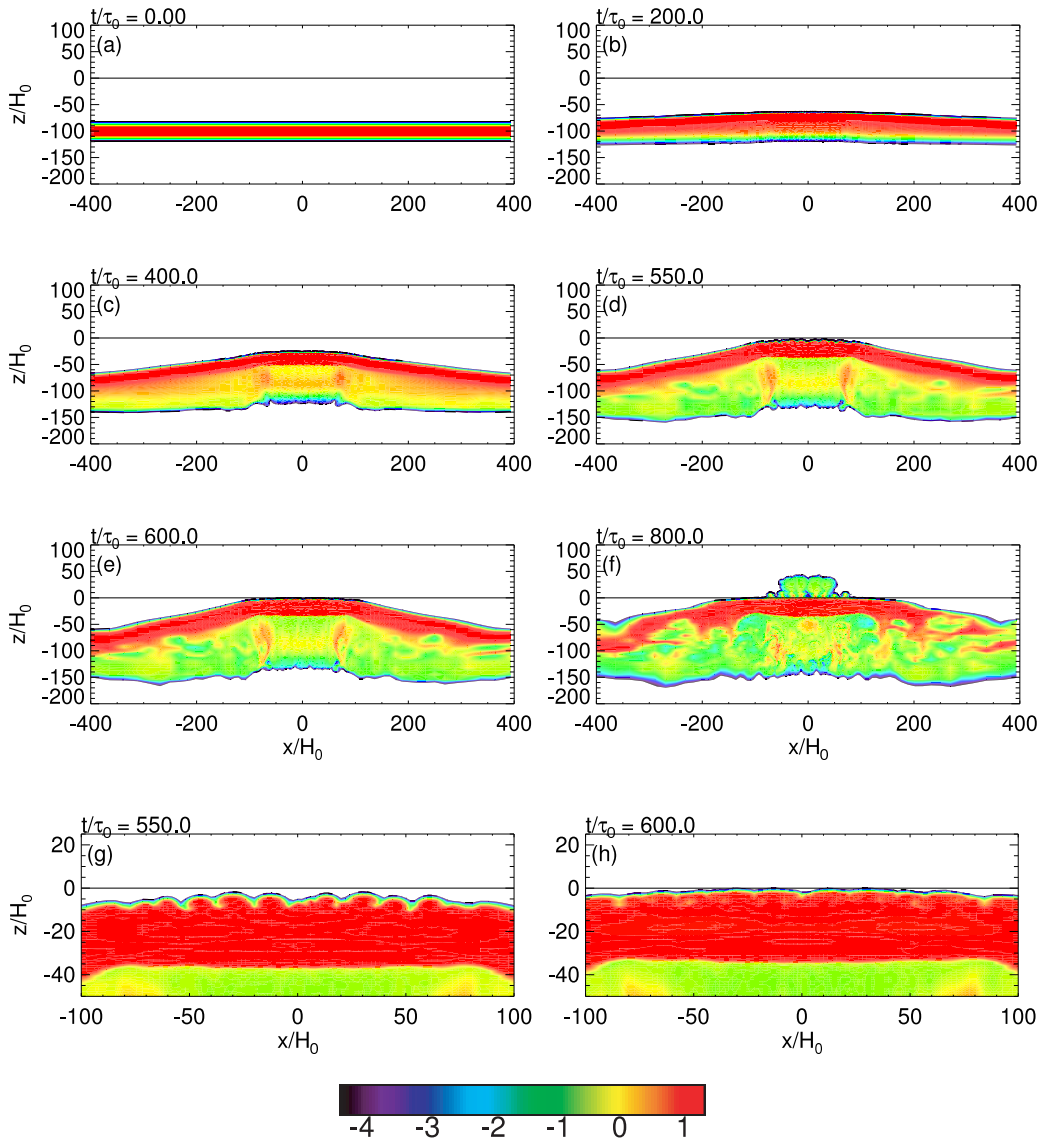


Figure 5.4: Time-evolution of cross-section at  $y/H_0 = 0$ . Logarithmic field strength  $\log(|B|/B_0)$  is plotted, while the photospheric height  $z/H_0 = 0$  is indicated with a solid line. (g) and (h) are the closeups of (d) and (e), respectively.

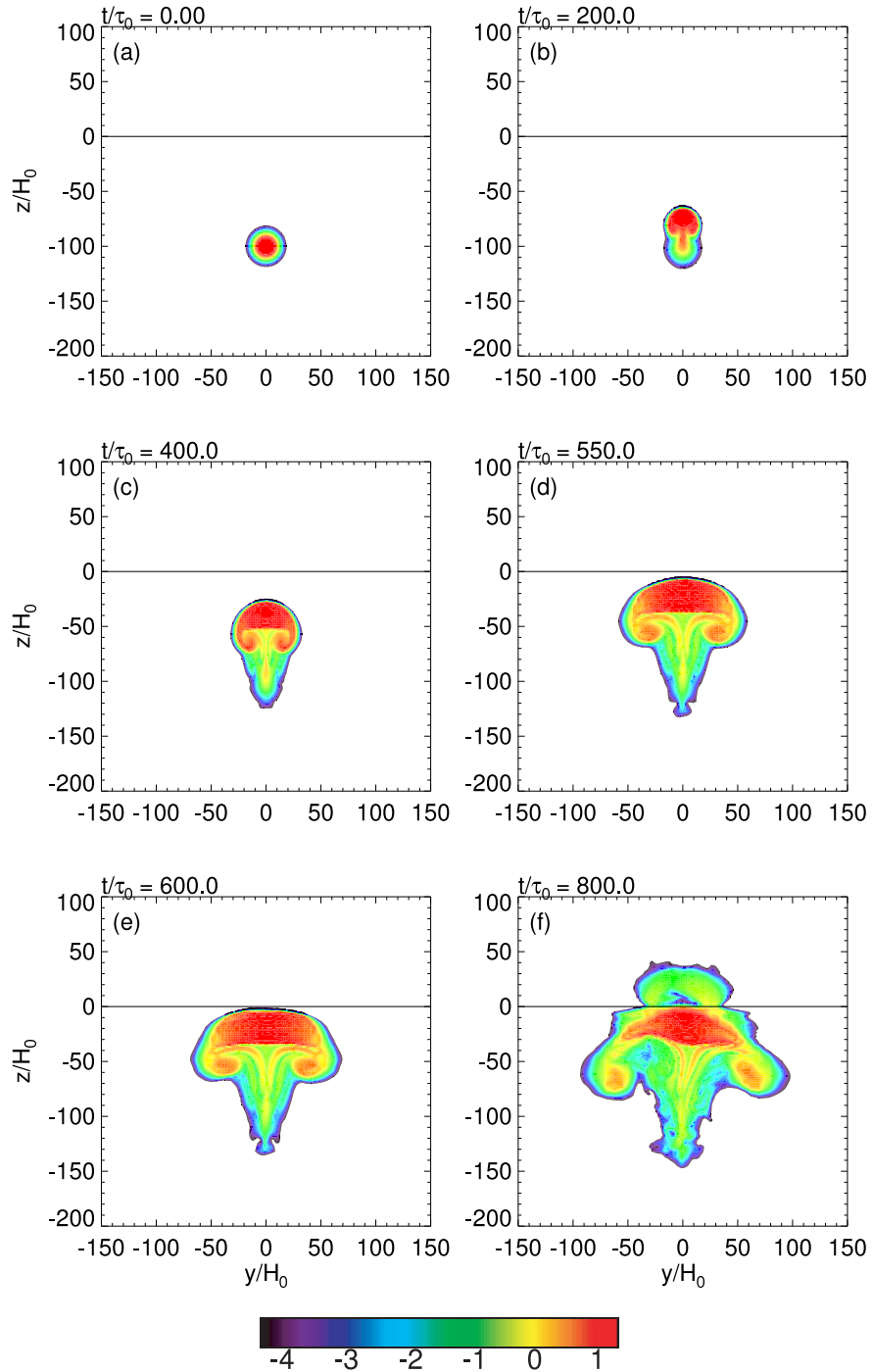


Figure 5.5: Time-evolution of cross-section at  $x/H_0 = 0$ . Logarithmic field strength  $\log(|B|/B_0)$  is plotted, while the photospheric height  $z/H_0 = 0$  is indicated with a solid line.

upward motion, the top of the fluted structure cannot pass through the surface, and, as a result, the dipped parts become filled with magnetic fields. At  $t/\tau_0 = 600$ , the subphotospheric magnetic field has a sheet-like structure extending  $-100 < x/H_0 < 100$  and  $-50 < y/H_0 < 50$ .

After the secondary emergence starts, the tube continues to extend in  $x$ -direction (Figure 5.4(f)), while the middle part sinks slightly (Figure 5.5(f)). Here, the  $(y, z)$ -section reveals asymmetric shape, i.e., the tube has a chirality. It is due to the azimuthal component of the field lines (the twist of a flux tube). At  $t/\tau_0 = 800$ , the subsurface structure extends  $-200 < x/H_0 < 200$  and  $-40 < y/H_0 < 40$ . In the outer region where  $|x|$  or  $|y|$  is large, the magnetic field is deformed. This is an appearance of numerical diffusion due to large grid spacings there.

### 5.3.3 Magnetic Buoyancy Instability at the Surface

As the magnetic flux around the surface satisfies the criterion for the magnetic buoyancy instability, the tube rises again into the corona ( $t/\tau_0 \gtrsim 600$ ). Figure 5.6(a) shows the magnetic field profile at the surface ( $z/H_0 = 0$ ) at the time  $t/\tau_0 = 650$ , i.e., just before the secondary emergence. From this figure, four apices of the subphotospheric flux sheet are seen. Figure 5.6(b) shows the vertical distribution of magnetic pressure  $p_{\text{mag}}/p_0$ , gas pressure  $p_{\text{gas}}/p_0$ , and density  $\rho/\rho_0$  at  $(x/H_0, y/H_0) = (13, 1)$  (one center of the emergent regions) at  $t/\tau_0 = 650$ . At around  $z/H_0 = 0$ , magnetic field excludes the plasma ( $\beta = p_{\text{gas}}/p_{\text{mag}} < 1$ ) to make a top-heavy structure. That is, this point is unstable. From Figure 5.6(a), we see that the surface field is mostly directed in the negative  $y$ -direction, and that  $\lambda_{\parallel} \sim 30H_0$  and  $\lambda_{\perp} \sim 20H_0$ . Here, we confirm only that the surface field is unstable, and we shall leave the analysis of what decides the wavelength of the instability for future work. The criterion for the magnetic buoyancy instability is as follows (Acheson, 1979,

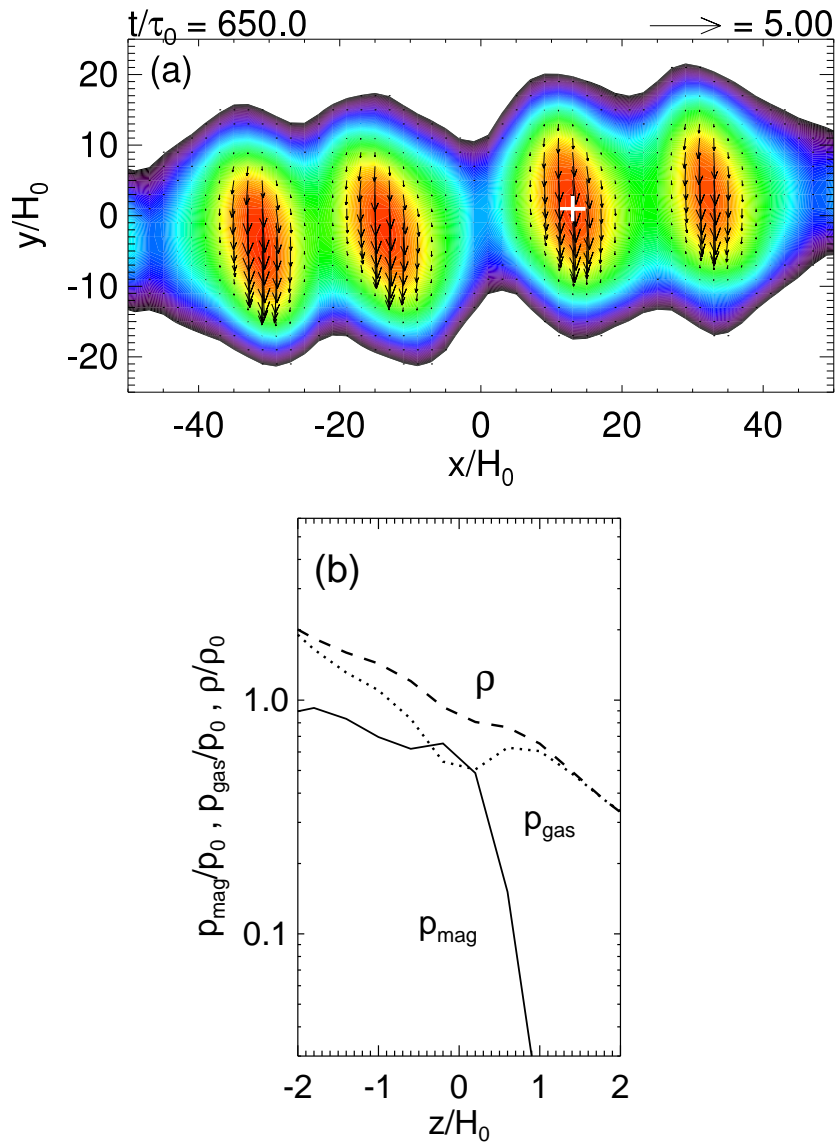


Figure 5.6: (a) Photospheric field profile  $\log(|B|/B_0)$  at  $z/H_0 = 0$  at the time  $t/\tau_0 = 650$ . Color contour is the same as that of Figure 5.4. Horizontal field is overplotted with arrows, while one center of the emergent regions  $(x/H_0, y/H_0) = (13, 1)$  is indicated with plus sign. (b) Vertical ( $z$ -)distributions of magnetic pressure  $p_{\text{mag}}/p_0$  (solid line), gas pressure  $p_{\text{gas}}/p_0$  (dotted line), and density  $\rho/\rho_0$  (dashed line) along  $(x/H_0, y/H_0) = (13, 1)$  at  $t/\tau_0 = 650$  are shown.

see also Appendix A):

$$-H_0 \frac{\partial}{\partial z} (\log B) > -\frac{\gamma}{2} \beta \delta, \quad (5.10)$$

where  $\delta = \nabla - \nabla_{\text{ad}}$  is the superadiabaticity,  $\nabla$  the logarithmic temperature gradient and  $\nabla_{\text{ad}}$  its adiabatic value. The left-hand-side term of the criterion (5.10) indicates the vertical distribution of the magnetic field. Where the magnetic field decreases drastically with height such as in Figure 5.6(b), this term has a destabilizing effect promoting the magnetic buoyancy instability. The right-hand side is the stabilizing term;  $\delta$  is negative in the isothermal photosphere, and  $\beta$  is below unity when there is no field. The time-development of the instability at the surface is shown in Figure 5.7. The solid line indicates the left-hand side of the criterion (5.10), namely, the destabilizing term, divided by plasma  $\beta$ , while the dashed line is the right-hand side (stabilizing term) also divided by  $\beta$ . We can confirm that, as time goes on, and as the magnetic field rises, the destabilizing effect overcomes the stabilizing term and satisfies the criterion (5.10) for the magnetic buoyancy instability.

Figure 5.8 shows the  $z$ -distribution of vertical velocity  $V_z$ , density  $\rho$ , and the horizontal magnetic field  $B_h = (B_x^2 + B_y^2)^{1/2}$  along the vertical axis  $(x/H_0, y/H_0) = (13, 1)$ . When the magnetic field is below the base height of the corona ( $z_{\text{cor}}/H_0 = 10$  at the initial state), the vertical velocity increases linearly with height (Figure 5.8(a)). The expansion law for the rising velocity is written as

$$V_z/C_{s0} = az/H_0. \quad (5.11)$$

From the figure, the approximate value of  $a$  is 0.08. The evolution of the density and the field strength follow

$$\rho \propto z^{-1}, \quad (5.12)$$

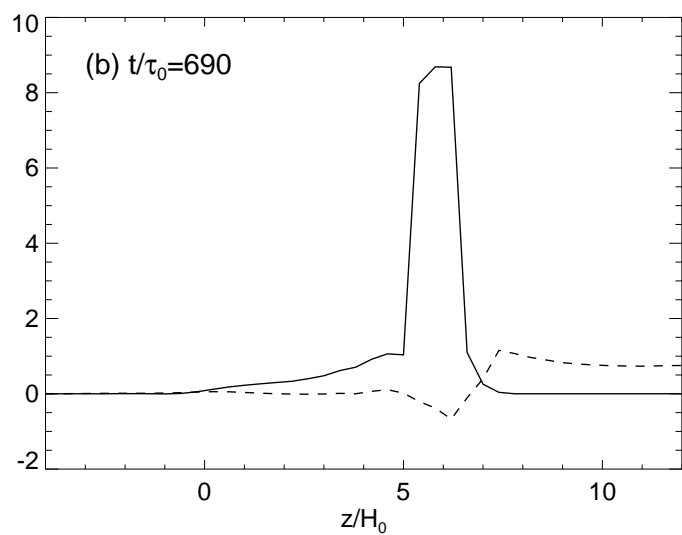
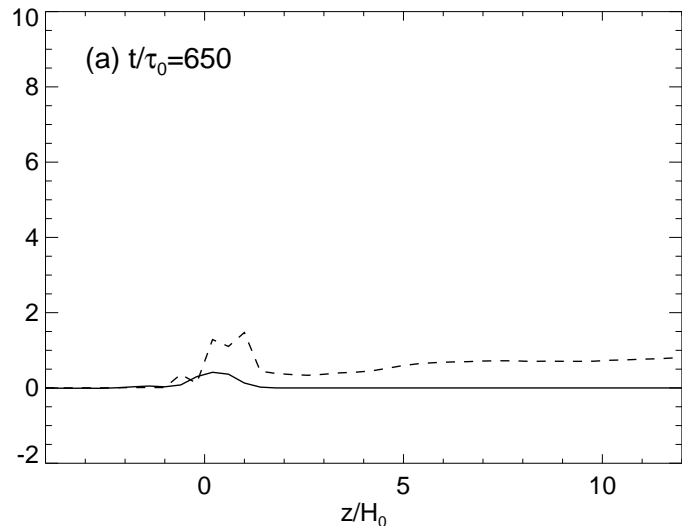


Figure 5.7: The vertical distribution along  $(x/H_0, y/H_0) = (13, 1)$  of the left-hand side of the criterion (5.10) divided by plasma  $\beta$ , i.e.,  $-H_0 \partial(\log B)/\partial z/\beta$  (solid line), and the right-hand side divided by  $\beta$ , i.e.,  $-\gamma\delta/2$  (dashed line). (a)  $t/\tau_0 = 650$  and (b)  $t/\tau_0 = 690$ .

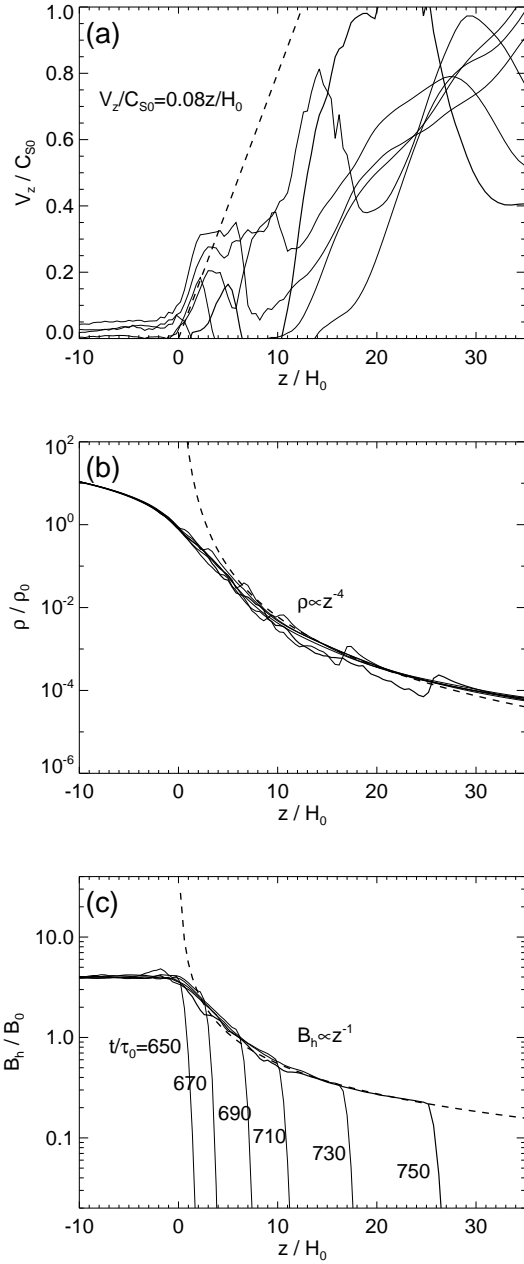


Figure 5.8: (a)  $z$ -distribution of the upward velocity  $V_z$  along the vertical axis  $(x/H_0, y/H_0) = (13, 1)$  at  $t/\tau_0 = 650$  (the thinnest line), 670, 690, 710, 730, 750 (the thickest line). The dashed line indicates the velocity-height relation. (b)  $z$ -distribution of the gas density  $\rho$ . The dashed line denotes the dependence  $z^{-4}$ . (c)  $z$ -distribution of the horizontal component of the magnetic field  $B_h = (B_x^2 + B_y^2)^{1/2}$ . The dashed line denotes the dependence  $z^{-1}$ .

and

$$B_h \propto z^{-4}, \quad (5.13)$$

respectively (Figures 5.8 (b) and (c)). These relations are fitted to the self-similar solution of a two-dimensional magnetic loop (e.g. Shibata et al., 1989). According to Matsumoto et al. (1993), the field strength of a three-dimensional single loop decreases faster than  $z^{-1}$  due to the horizontal expansion, i.e., the loop can also expand in the direction perpendicular to the magnetic field (the free expansion regime). However, in our case, the field strength almost follows  $z^{-1}$ , which indicates that the horizontal expansion is restricted by the neighboring loops (the collimated expansion regime). Here, we assume that the effect of the magnetic shear is relatively small in the initial phase of the second-step emergence. Figure 5.9 shows the vertical distribution of the shear angle [ $\arctan(B_y/B_x)$ ]. The shear

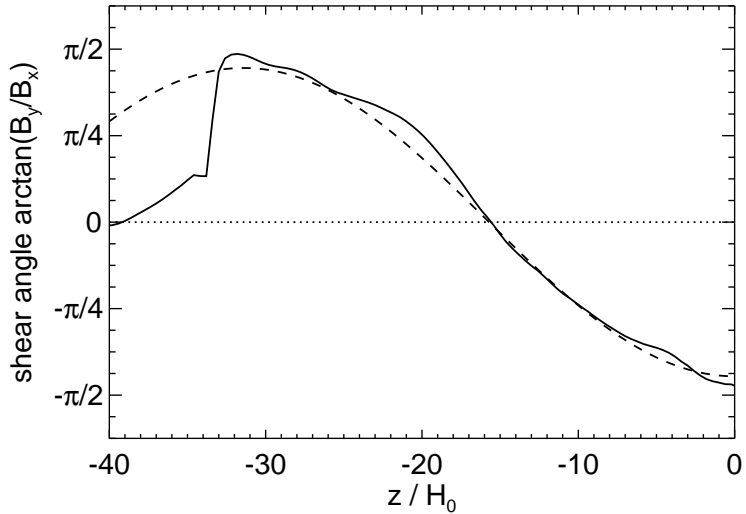


Figure 5.9: The solid line indicates the  $z$ -profile of the shear angle  $\arctan(B_y/B_x)$  along  $(x/H_0, y/H_0) = (13, 1)$  at the time  $t/\tau_0 = 650$ . The dashed line is  $-1.4 \cos(z/10H_0)$ , and the dotted line indicates the shear is 0.

is almost constant around the surface ( $z/H_0 > -5$ ). Therefore, we apply the discussion by Matsumoto et al. (1993), which considers the non-sheared magnetic flux.

### 5.3.4 Time-evolution of the Photospheric Magnetic and Flow Fields

Figure 5.10 shows the evolution of the photospheric vertical magnetic field  $B_z/B_0$  (magnetogram), while Figure 5.11 is the corresponding vertical velocity  $V_z/C_{s0}$  (Dopplergram) with the horizontal velocity field. Here, red indicates the downward motion ( $V_z/C_{s0} < 0$ ) of the plasma. At  $t/\tau_0 = 600$ , there is no magnetic field and no clear movement (Figures 5.10(a) and 5.11(a)). In Figures 5.10(b) and 5.11(b), we find that some blueshifts and divergent flows have come out before the magnetic fields appear. Four apices of the magnetic field emerge at  $t/\tau_0 = 650$  (Figure 5.10(c)). In Figure 5.10(d), at  $t/\tau_0 = 680$ , four pairs of white and black patches are clearly seen. The absolute field strength of each polarity is more than a hundred Gauss. In Figure 5.11(d), downflows of up to  $0.2C_{s0} = 2 \text{ km s}^{-1}$  are seen in the core of each patch, while the blueshifts are of the order of a few  $\text{km s}^{-1}$ . At this time, the flow speed in the positive and negative polarities is at its peak ( $\sim 0.5C_{s0} = 5 \text{ km s}^{-1}$ ). These features indicates that the magnetic flux emerges upward, while the plasma drains downward to the both footpoints along the field lines. The observed values are fitted to the actual observations introduced in Section 1.2 (see Section 5.4.2 for discussion in detail). Note that the horizontal velocity of the plasma does not always agree with the transverse speed of the magnetic element. However, at the point where the magnetic field is nearly vertical (e.g., at the footpoint of the emerging flux), the horizontal velocity of the flow field almost agrees with the transverse motion of the field line.

At  $t/\tau_0 = 700$ , another four pairs of magnetic elements emerge beside the four main patches in the central area (Figure 5.10(e)). While the emergence (separation) continues, inflows occur at the both sides of each emerging field (Figure 5.11(e)). In Figure 5.10(f), each patch has come into the shape of a tadpole and is slightly sheared. The tadpoles are formed because the newly emerging elements separate outward and catch up with the elements that had emerged earlier and stopped at the edge of the region. The shearing motion of the heads of tadpoles (pores) is leftward in the upper half and rightward in the

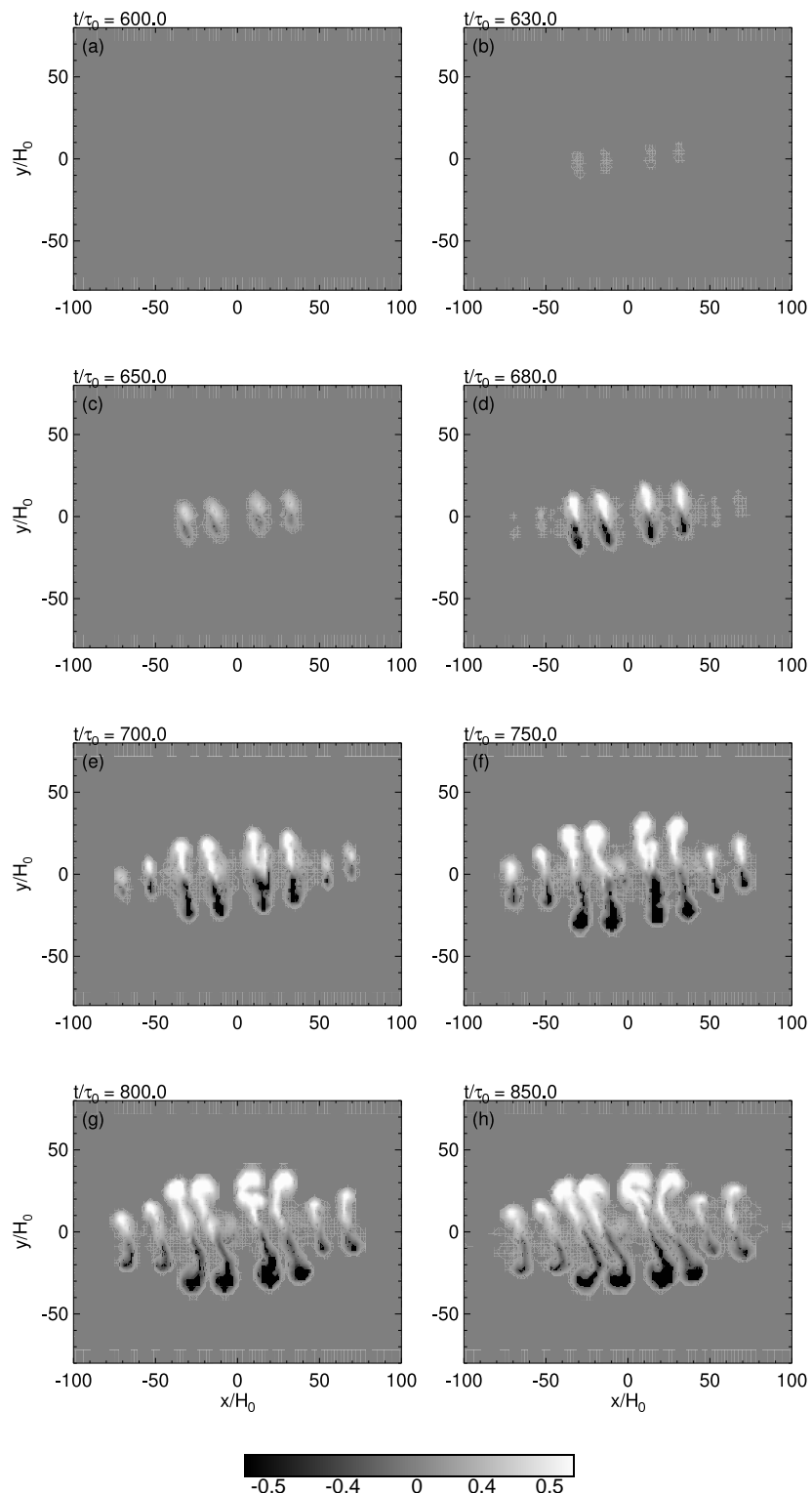


Figure 5.10: Time-evolution of the photospheric vertical magnetic field  $B_z/B_0$  (magnetogram). White (black) indicates the positive (negative) polarity.

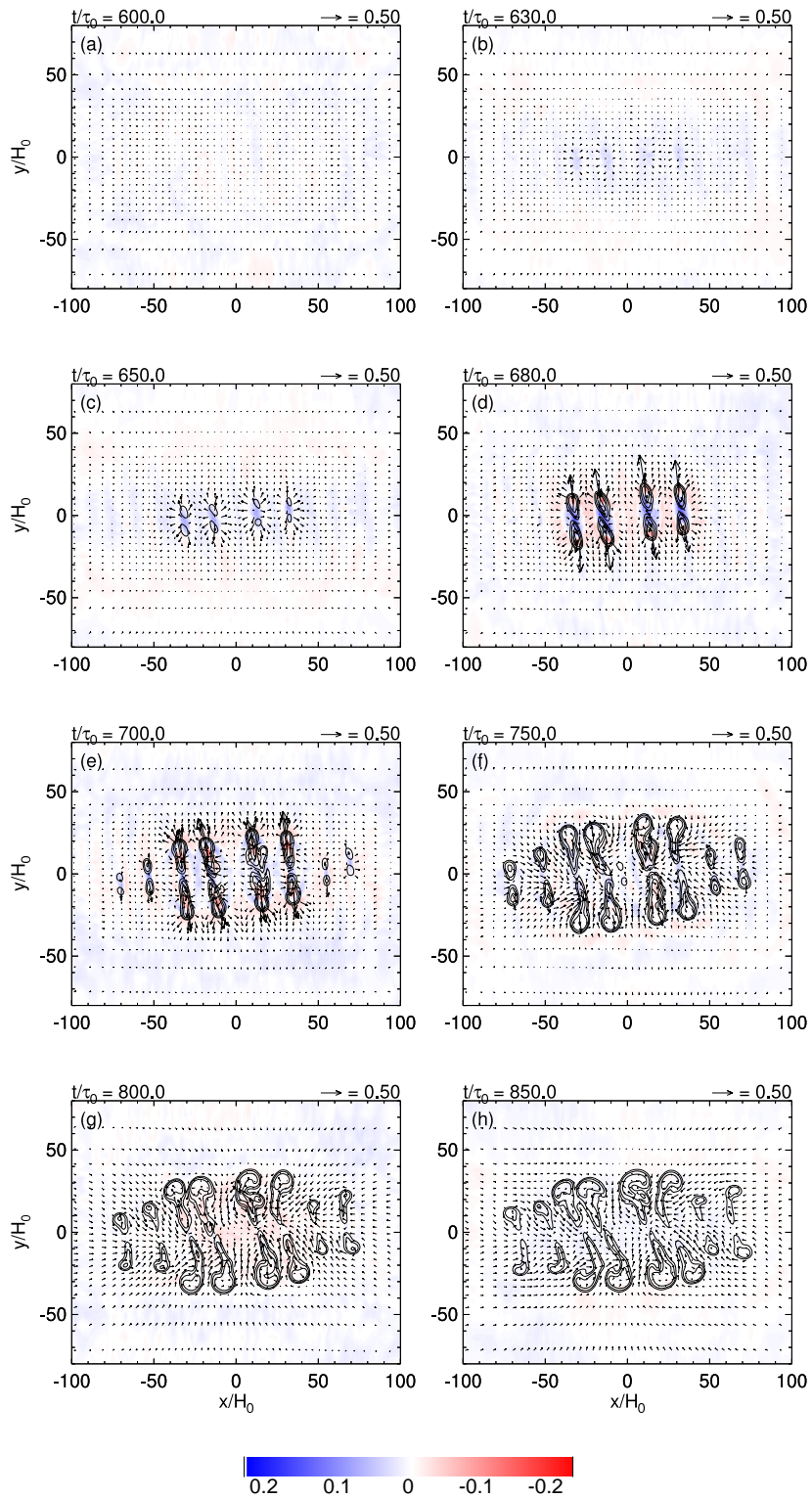
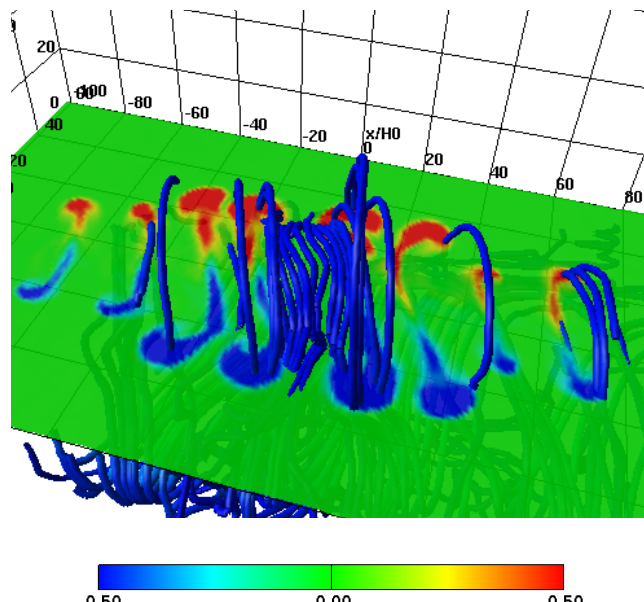


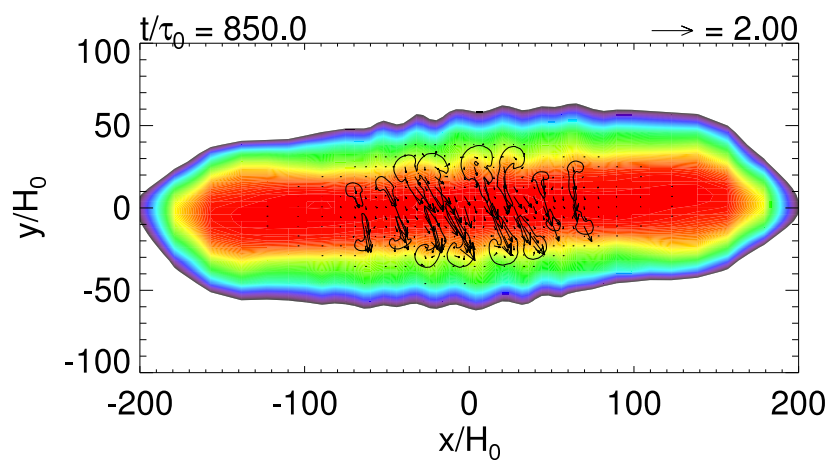
Figure 5.11: The corresponding velocity field (Dopplergram). Shown are the vertical velocity  $V_z/C_{s0}$  (the red-blue color; red is downward), the horizontal speed (arrows), and the vertical magnetic field (contour;  $B_z = \pm 0.17B_0, \pm 0.33B_0$ , and  $0.67B_0$ .)

lower. At this moment, in Figure 5.11(f), the separations are no more seen. The horizontal flow field reveals that the converging flows go into each center of the emergent area. This may be caused by the rapid expansion of the magnetic field in the upper atmosphere. At the time  $t/\tau_0 = 800$ , both polarities do not move in the  $y$ -direction anymore, only to continue shearing in the  $x$ -direction (Figure 5.10(g)). There is no strong red/blueshift in the magneto patches in Figure 5.11(g), which indicates that the emergence has stopped.

Finally, at  $t/\tau_0 = 850$ , the active region extends  $-80 < x/H_0 < 80$  and  $-40 < y/H_0 < 40$ , i.e.,  $32 \text{ Mm} \times 16 \text{ Mm}$  (Figure 5.10(h)). The magnetic elements in the central region reveals a strongly tilted structure. Also, the heads of the tadpoles ( $|B_z|$  up to 240 G) make two alignments in the upper and lower halves. Figure 5.12(a) shows the magnetic field lines at this moment. We find that the field lines connect the photospheric patches. The heads are fragmented by the converging flows (Figure 5.11(h)). The consequent Figures 5.10(h) and 5.12(a) are strongly reminiscent of the observations of NOAA AR 5617 by Strous & Zwaan (1999) (see Figure 1.6). The separating and shearing motion of the photospheric magneto-patches and the atmospheric field lines connecting the patches are consistent. Note that the difference between the present tilt of the magnetic elements and that of AR 5617 in Figure 1.6 is due to the twist of the initial flux tube. In the present case, we assume a flux tube of right-handed twist, which is favorable for the southern hemisphere. Active region 5617 emerged in the northern hemisphere, which implies that the twist of this region would be left-handed. Figure 5.12(b) shows the subsurface magnetic sheet at  $z/H_0 = -10$  and the corresponding photospheric vertical field  $B_z/B_0$  and the horizontal field at the time  $t/\tau_0 = 850$ . From this figure, we see that the footpoints of the expanding coronal fields (separated magnetic patches) stop at the boundary of the subphotospheric field. Note that the wavy structure of the subphotospheric field in the middle ( $-80 < x/H_0 < 80$ ) is due to the interchange mode instability of the field lines.



(a)



(b)

Figure 5.12: (a) Perspective view of photospheric vertical magnetic field  $B_z/B_0$  with selected field lines at  $t/\tau_0 = 850$ . (b) Color is the subphotospheric magnetic field  $\log(|B|/B_0)$  at  $z/H_0 = -10$  at the time  $t/\tau_0 = 850$ . Color bar is the same as that in Figure 5.4. Also plotted are the surface vertical field  $B_z/B_0 = 0.17$  (contour) and the corresponding horizontal field (arrows).

### 5.3.5 Coronal Magnetic Field and the Shearing Motion

As time goes on, several magnetic domes are built above the surface till  $t/\tau_0 = 850$  (e.g. Figure 5.2). During this period, photospheric fields are continuously transported into the corona. The driving force of the expansion is the magnetic pressure. At  $t/\tau_0 \sim 850$ , the rising motion stops since the upward magnetic pressure balances with the surrounding gas pressure. The height of the magnetic domes are  $z_{\text{apex}}/H_0 \sim 40$ , which is much smaller than those of previous 2D calculations ( $z_{\text{apex}}/H_0 \sim 200$ ). This is an effect of the three-dimensionality. In 3D simulation, the magnetic pressure expands the magnetized plasma in the horizontal direction as well as in the vertical direction. As a result, the consequent magnetic domes as a whole show a “free expansion” and become less taller, although the some central domes show a “collimated expansion” (see Section 5.3.3).

Figure 5.13 shows the perspective view of the photospheric vertical field  $B_z/B_0$  with selected field lines that pass through the vertical axis  $(x/H_0, y/H_0) = (13, 1)$ , i.e., one center of the separations. In this figure, some selected field lines that pass through the vertical axis  $(x/H_0, y/H_0) = (13, 1)$  are overplotted. As the evolution develops, field lines rise upward and the footpoints separate. Also one can see that the field lines become sheared.

The shearing motion of the magnetic field is caused by the two reasons: (1) the emergence of the inner field lines (kinematic effect), and (2) the Lorentz force acting on the surface field (dynamic effect). In this calculation, the initial flux tube is uniformly twisted, i.e.,  $B_\phi(r) = qrB_x(r)$ . Here, the pitch angle of the tube field line  $\tan \Psi \equiv B_\phi/B_x$  increases as the radial distance to the tube axis increases. Thus, the field lines that appear first at the photosphere are the outermost fields of the flux tube (Figure 5.13(*top*)). As the field rises above the photosphere, the inner field of the flux tube become emerged. Therefore, the photospheric patches and the field lines in the central area become tilted (Figure 5.13(*bottom*)). The approximate angle of the photospheric horizontal field in the emergent area from the  $x$ -axis, i.e.,  $\arctan(B_y/B_x)$  is  $\sim -0.4\pi$ , which was almost  $-\pi/2$ .

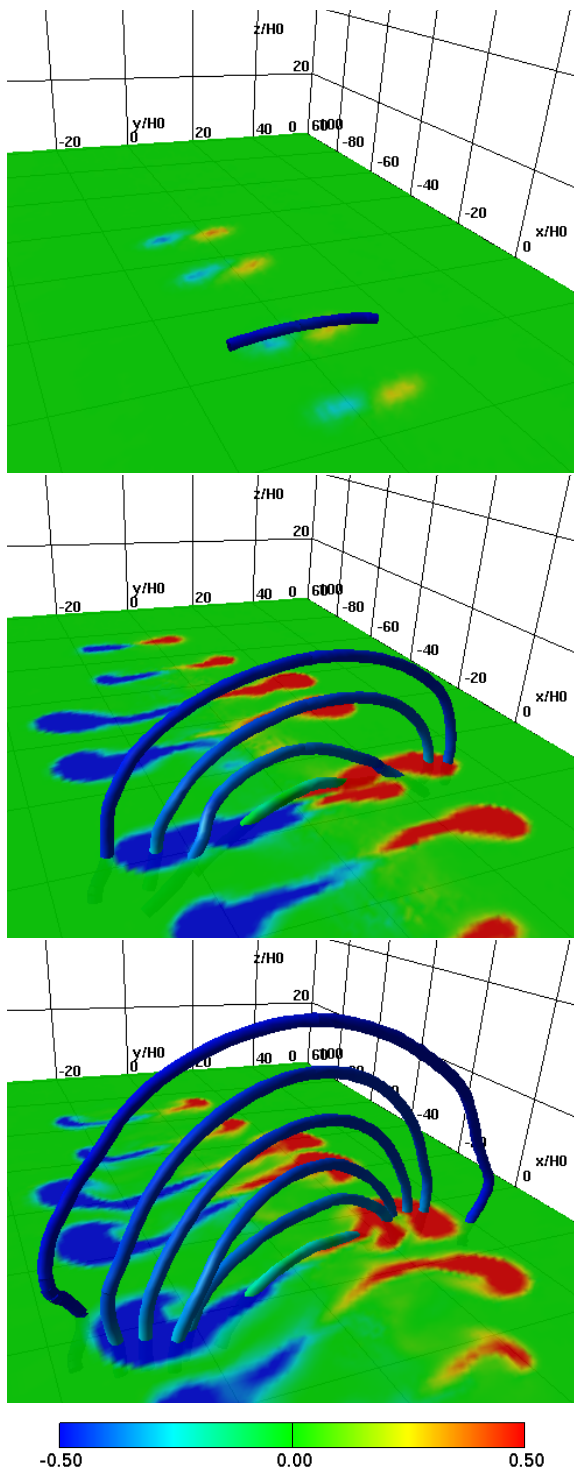


Figure 5.13: Perspective view of photospheric vertical magnetic field  $B_z/B_0$  with selected field lines that pass through the vertical axis  $(x/H_0, y/H_0) = (13, 1)$ . From top to bottom,  $t/\tau_0 = 650, 750$ , and  $850$ , respectively.

at  $t/\tau_0 = 650$ . In Figure 5.9, the shear angle  $-0.4\pi$  was located at  $z/H_0 = -5$  at  $t/\tau_0 = 650$ . Therefore, it can be said that the present photospheric field has emerged from  $z/H_0 = -5$  in this  $200\tau_0 = 5000$  s  $\sim 1.4$  hr. This result also indicates that the axial field of the rising flux tube is far below the surface in this final phase.

The magnetic field in the head of the tadpole-like structure is also shearing. This is caused by the Lorentz force

$$\mathbf{f}_{\text{Lorentz}} = -\nabla \left( \frac{B^2}{8\pi} \right) + \frac{1}{4\pi} (\mathbf{B} \cdot \nabla) \mathbf{B}. \quad (5.14)$$

The first term of the right hand side is the gradient of the magnetic pressure, which results in the expansion of magnetic domes. The second term describes the magnetic tension force. When the rapid expansion of the magnetic field into the rarefied corona occurs, the  $x$ -component of the magnetic field decreases with height, which makes the  $x$ -component of the magnetic tension  $(\mathbf{B} \cdot \nabla) B_x / (4\pi)$  positive (negative) if the vertical field  $B_z$  is downward (upward). Then this term drives the horizontal shearing motion. Figure 5.14 shows the horizontal magnetic tension at  $t/\tau_0 = 850$ . The magnetic tension is almost positive (negative) in the  $x$ -direction in the lower (upper) half.

Figure 5.15 shows the development of the photospheric vertical flux for each polarity and the total unsigned flux. After  $t/\tau_0 \sim 630$ , the fluxes gradually increase. The positive and the negative fluxes are strongly correlate with each other, which indicates that the structure of the photospheric magneto patches is highly point-symmetric. The vertical flux levels off after  $t/\tau_0 = 750$ . In this phase, the surface magnetic patches show the shearing motion. The final value of the total unsigned flux is  $\sim 1.9 \times 10^{20}$  Mx.

At the final moment  $t/\tau_0 = 850$ , the magnetic flux above the surface calculated at the middle of the flux tube ( $x/H_0 = 0$ ) is  $\int_{z>0} B_x dy dz = 7.9 \times 10^{18}$  Mx. That is, only 1.2 % of the initial axial total flux ( $\int B_x dy dz = 6.3 \times 10^{20}$  Mx) has emerged into the atmosphere.

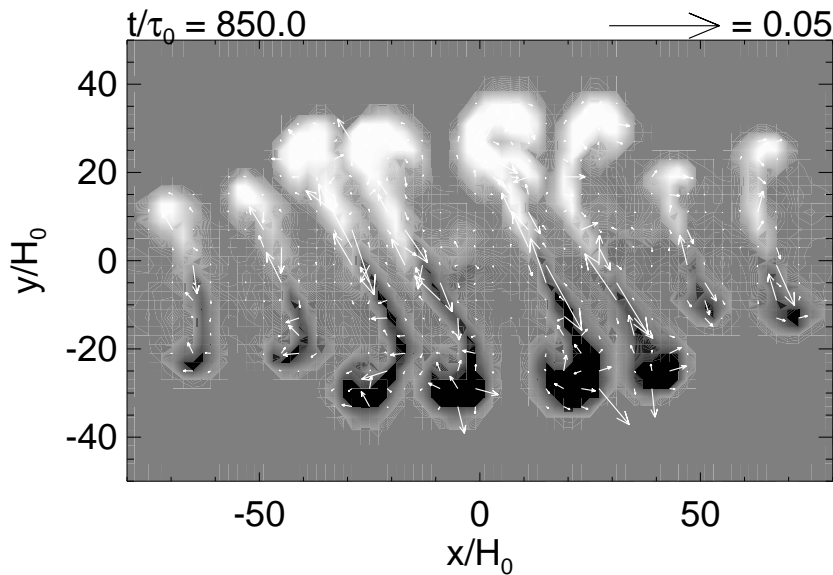


Figure 5.14: Photospheric vertical magnetic field  $B_z/B_0$  at the time  $t/\tau_0 = 850$ . The black-white contour is the same as in Figure 5.10. Overplotted arrows are the horizontal magnetic tension force  $(\mathbf{B} \cdot \nabla)\mathbf{B}/(4\pi)$ .

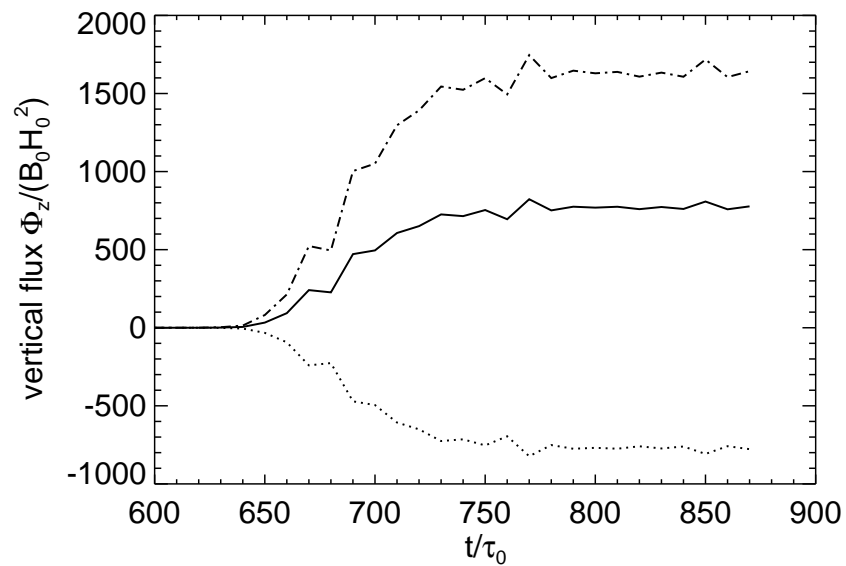


Figure 5.15: Time-evolution of photospheric vertical fluxes in the unit of  $B_0 H_0^2 = 1.2 \times 10^{15}$  Mx are shown. The solid, dotted, and dash-dotted lines are the positive, negative and the total unsigned flux, respectively.

## 5.4 Discussion

### 5.4.1 Overall Evolution

In this Chapter, we performed the three-dimensional experiment on the flux tube emergence from  $z = -20,000$  km. The initial condition adopted in this calculation ( $B_{\text{tube}} = 2.0 \times 10^4$  G,  $R_{\text{tube}} = 1000$  km, and  $q = 5.0 \times 10^{-4}$  km $^{-1}$ ) is consistent with the previous 2D results in Chapter 3 and 4. The flux tube rises through the convection zone due to its buoyancy. While in the interior,  $(x, z)$ -section at  $y/H_0 = 0$  shows a symmetric arched structure (see Figure 5.4), rather than a trapezoidal structure found in the 2D undular calculation in Chapter 3. In the 3D calculation, the plasma above the flux tube flows down around the tube's cross-section. Therefore, the flux tube is not so pushed down by the accumulated plasma as in the 2D sheet case. On the other hand,  $(y, z)$ -section at  $x/H_0 = 0$  (Figure 5.5) is similar to those in the 2.5D cross-sectional experiment in Chapter 4.

In the widely accepted picture by Zwaan (1985), the rising tube directly enters the atmosphere to make coronal fields (see Figure 1.4). In our case, however, as the tube reaches the photosphere, it expands horizontally to make a flattened structure (magnetic sheet) beneath the surface at  $t \sim 600\tau_0 = 4.2$  hr, with a spread of  $\sim 40$  Mm  $\times$  20 Mm (see e.g. Figure 5.2(e)). This is caused by the isothermal, i.e., convectively stable photosphere. The subphotospheric extension is consistent with both types of previous 2D experiments, although the sheet size of the present model at this moment is only a half of that in the 2D undular experiment. The picture of the direct entrance in Figure 1.4 should be somewhat modified as to show the subphotospheric structure extending beneath the active region.

As the surficial field locally satisfies the criterion (5.10) for the magnetic buoyancy instability, the field starts further evolution into the upper atmosphere due to its magnetic pressure. Because of the neighboring domes, each dome evolves mainly in the vertical direction, i.e., the collimated expansion regime in Matsumoto et al. (1993). However, as the domes grow, the magnetic pressure comes to exert also in the horizontal direction (the

free expansion regime). As a result, the magnetic domes reach  $z \sim 40H_0 = 8000$  km, which is shorter than  $z = 20,000$  km in both 2D experiments in Chapter 3 and 4.

### 5.4.2 Comparison with NOAA AR 5617

In the photospheric magnetogram, we observed several separations of the magnetic elements (see Figure 5.10). At the edge of the region, we found the alignments of heads of tadpole-like magnetic structures (pores). The tadpoles were formed because the newly separated elements move outward to catch up with the elements that had emerged earlier and stopped at the edge. And the alignments of the pores showed shearing motions. These are the new findings in this experiment. As far as we know, we have never seen such photospheric features, especially the several separations, in the previous calculations (e.g. Fan, 2001; Archontis et al., 2004; Murray et al., 2006).

These features are strongly reminiscent of the observation of NOAA AR 5617 by Strous & Zwaan (1999) (see Figure 1.6). The shearing motion of the heads of the tadpole structures is consistent with the pores moving along the edges of the active region toward the main sunspots. The difference of the tilt of magnetic elements in two cases is caused by the twist direction. We assumed a right-handed tube in the initial state, which is favorable for the southern hemisphere, while AR 5617 was in the northern hemisphere, which indicates the left-handed twist.

The summary of the comparison between our results and the observations by Strous et al. (1996) and Strous & Zwaan (1999) is presented in Table 5.1. From this Table, one can see that the size of the region and the length of the aligned pores of our present result are comparable to those of the actual active region. We confirmed that these values (length scales of the region) are dependent on the spread of the subphotospheric magnetic structure (see Figure 5.12(b)). Namely, the flattened flux tube beneath the surface decides the extension of the active region.

The photospheric total flux is one digit smaller than the observed value. Also, we

Table 5.1: Summary of Comparison with NOAA AR 5617

	Present Result	NOAA AR 5617
size of the region	32 Mm $\times$ 16 Mm	50 Mm $\times$ 30 Mm
length of aligned pores	$\sim$ 16 Mm	$\sim$ 15 Mm
vertical unsigned total flux	$1.9 \times 10^{20}$ Mx	$4 \times 10^{21}$ Mx
age from the first appearance	(0–1.4) hr	(7.5–9) hr
separation speed	(4–10) km s $^{-1}$	0.84 km s $^{-1}$ <sup>a</sup>
shearing speed	$\sim$ 1 km s $^{-1}$	0.73 km s $^{-1}$ <sup>b</sup>
upflow velocity	$\sim$ a few km s $^{-1}$	0.86 km s $^{-1}$ <sup>c</sup>
downflow velocity	< 2 km s $^{-1}$	1.26 km s $^{-1}$ <sup>d</sup>
wavelength of emergence pattern	-	$\sim$ 8 Mm

<sup>a</sup>Separation of facular elements (Strous et al., 1996).

<sup>b</sup>Separation of pores (Strous et al., 1996).

<sup>c</sup>Upflow in an emergent region (Strous & Zwaan, 1999).

<sup>d</sup>Downflow in a facula (Strous & Zwaan, 1999).

did not find the major sunspots in our active region. These may be because the rising magnetic field in our calculation stops in 1.4 hours since it appears at the surface. The age of AR 5617 was estimated to be 6.5–7.5 hours old at the beginning of the observation and 8–9 hours old at the end. In Section 5.3.5, we found that the axis of the flux tube is far below the surface at the final phase and that only 1.2 % of the initial axial flux has emerged above the surface. The mechanism of the rising of the whole tube, at least half of the tube, is needed to be solved.

The upward and downward velocities and the shearing speed are consistent with the observed values, while the separation speed is somewhat larger than the observation. However, according to Harvey & Martin (1973), the separation speed was measured to be more than 2 km s $^{-1}$  at the initial phase of the emergence. In AR 5617 observation, the emergence events showed undulatory structures with a typical wavelength of 8 Mm, which can be explained by the undulatory instability (see Appendix A). However, in our case, each photospheric field line makes only a single apex. The undulating feature might be found in a more resolved calculation or in the calculation that includes the thermal convection. The formation of photospheric undulatory fields is also discussed in Chapter

6.

Fan (2001) also compared her numerical results of the 3D tube emergence with AR 5617 observation by Strous et al. (1996). One of the essential differences of the present results from Fan (2001) is the multiple separation events at the surface (compare, e.g., Figure 1.12 and Figure 5.10). This difference reflects the initial conditions of the two cases. That is, in her calculation, the strong initial tube of 6000 G embedded in  $-1500$  km directly enters the photosphere, without significantly showing a subsurface magnetic structure (see Fan, 2001, Figures 2 and 3). As a result, the flux tube emerges into the corona as a single dome and shows only a single pair of magneto patches at the surface. On the contrary, we found that the initial tube embedded much deeper in  $-20,000$  km suffers a deceleration and extends horizontally beneath the surface to make a flat magnetic sheet. Eventually, multiple domes are built above the surface due to the interchange mode instability. The picture of  $\Omega$ -tube emergence in Fan (2001) is intrinsically the same in our calculation. However, we confirmed that the subsurface structure owing to the large-scale emergence is essential to determine the size of active region and the detailed structures such as separations.

### **5.4.3 A Model for the Flux Emergence and the Formation of Active Region**

On the basis of the observations, Strous & Zwaan (1999) suggested the vertical sheet model that each emergence occurs in a single vertical sheet, which forms a series of sheets aligned in a parallel fashion (see Figure 1.7). In our case, the separation events are the consequence of the interchange mode instability of the photospheric magnetic flux. Therefore, the vertical sheet model can be considered as the result of the interchange mode instability of the flattened twisted flux tube beneath the surface. Also, the shearing motion of the magnetic elements traveling along the edge of the active region can be explained as the emergence of the inner field of the flux tube. The pitch angle of the

inner field is smaller, thus the footpoints shift as the secondary emergence continues (the kinematic effect). The shearing of the aligned pores (heads of the tadpoles) are explained by the Lorentz force (the dynamic effect).

The above results are schematically illustrated in Figure 5.16. (1) The flux tube rises through the convection zone. Since the density decreases with height, the tube expands and the pitch angle of the field lines increases during its ascent to the surface. (2) Approaching the surface, the flux tube gradually becomes flattened due to the convectively stable photosphere in front of the rising tube. (3) When the photospheric field satisfies the criterion for the magnetic buoyancy instability, the secondary evolution to the corona breaks out. Due to the interchange mode instability, photospheric magnetogram shows several ( $\sim 8$ ) separation events. The separated elements reach the edge of the region, which is determined by the subsurface field, and make two alignments of pores. (4) As the emergence continues, the inner field of the flux tube emerges and the footpoint shifts to show the shearing motion. The Lorentz force (the magnetic tension force) also drives the pores to shear.

Matsumoto et al. (1998) performed three-dimensional MHD simulations on the buoyant emergence of tightly twisted flux tube. The rising portions of the flux tube are deformed into a helical shape due to the kink instability and finally emerge into the corona. In their model, sequentially aligned sunspots observed in the magnetogram are explained as the consequence of the helical field (see Figure 1.11). That is, multiple regions are formed from a single kink-unstable tube. In the present model, on the other hand, only a single region is formed. The formation of main sunspots is considered as a result of the axial or inner field emergence.

#### 5.4.4 Comparison with 2.5D Cross-sectional Experiment

The initial condition of the present experiment ( $B_{\text{tube}} = 67B_0 = 2.0 \times 10^4 G$ ,  $R_{\text{tube}} = 5H_0 = 1000 \text{ km}$ , and  $q = 0.1/H_0 = 5.0 \times 10^{-4} \text{ km}^{-1}$ ) is the same as that of Case 5 in the

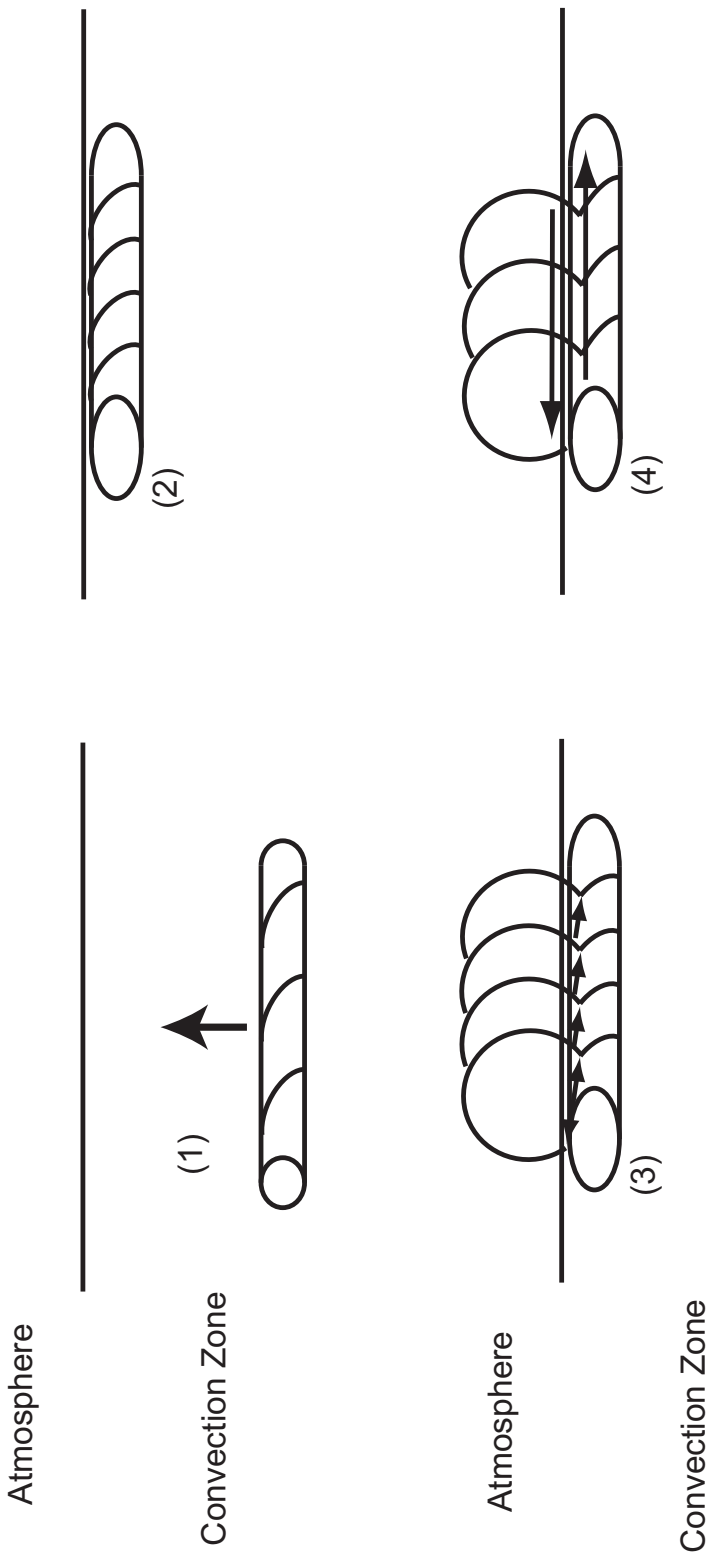


Figure 5.16: Model of flux tube emergence and the formation of active region. (1) The flux tube rises through the convection zone due to its buoyancy. (2) As the tube approaching the surface, it expands horizontally to make a flattened subphotospheric field. (3) When the surface field locally satisfies the condition for the instability, the field expands again into the rarefied atmosphere. Several separation events are observed due to the interchange mode instability. At the region edge, surface elements gather to make alignments of pores. (4) As the inner field appears, the footpoints show a shearing motion. The Lorentz force also drives the aligned pores.

“2.5D” cross-sectional calculation in Chapter 4. One of the basic differences between the two simulation results is the rising time from the initial depth of  $-20$  Mm to the surface. In 2.5D calculation, the flux tube reached the surface in  $t \sim 550\tau_0 = 3.8$  hr, while, in 3D case, it takes  $t \sim 600\tau_0 = 4.2$  hr. That is, the present tube rises slower. In 3D case, plasma in the tube apex drains down along the field lines to the both feet of the tube, which drives the tube more buoyant. At the same time, in the 3D regime, the magnetic curvature force pulls down the rising tube. The time difference between the two cases indicates that the curvature force dominates the draining effect in the present 3D experiment.

## 5.5 Conclusions

The followings are the conclusions of the present large-scale 3D experiment.

- Initially, the flux tube with the field strength of  $2.0 \times 10^4$  G, the total flux of  $6.3 \times 10^{20}$  Mx, and the twist of  $5.0 \times 10^{-4}$  km $^{-1}$  starts emergence due to its buoyancy in the convection zone. As reaching the surface after  $t \sim 2.8$  hr, the tube decelerates and extends horizontally (40 Mm  $\times$  20 Mm) owing to the convectively stable surface ahead of the tube. As the surface field satisfies the criterion for the magnetic buoyancy instability, the field emerges again into the upper atmosphere after  $t \sim 4.1$  hr. Eventually, several domes reach of a height of  $\sim 8000$  km are formed at  $t \sim 5.9$  hr.
- The size of the active region grows to 32 Mm  $\times$  16 Mm. At the photosphere, several separation events of the surface magnetic element are newly observed. Such elements of both polarities move apart from each other at the rate of 4–10 km s $^{-1}$ , and stop at the edge of the active region, which is determined by the extension of the subphotospheric field. Thus, the magnetic elements gather at the edge to make two alignments of the pores in the upper and lower halves. The several separations are the result of the interchange mode instability of the surface field. The alignments

of the pores show shearing motions of the order of  $1 \text{ km s}^{-1}$ , which is explained by the emergence of the inner field and the effect of the Lorentz force. Upflows of a few  $\text{km s}^{-1}$  and downflows up to  $2 \text{ km s}^{-1}$  are observed in the emergent areas and in the cores of surface fields, respectively. These findings are well similar to the observations of NOAA AR 5617 by Strous et al. (1996) and Strous & Zwaan (1999). However, the total flux is much smaller than the observed value and the major sunspots are not formed, since only a part of the surface field rises above the photosphere. We have to figure out the mechanism of the emergence of the whole tube.

- On the basis of the numerical results, we suggest a new model of the flux emergence and the consequent formation of active region, which includes the vertical sheet model by Strous & Zwaan (1999). The key points of our model are the separation events caused by the interchange instability of the photospheric field, the alignments of pores at the edge of the region determined by the subsurface field, and the shearing motions of the pores due to the inner field emergence and the Lorentz force.
- Compared to the 2D cross-sectional experiment, the present 3D flux tube rises slower. In the 3D calculation, the mass draining from the apex occurs to accelerate the Parker instability, while the downward magnetic tension pulls down the rising tube. The result of the present slow emergence implies the dominance of the tension force.



# Chapter 6

## Dependence on the Twist Intensity

### 6.1 Introduction

From the observations of active regions and the corresponding numerical calculations, it is widely accepted that the emerging flux tube is somewhat and somehow twisted (see Chapter 1). Observationally, the twist rate is measured by using force-free parameter. In the place where plasma  $\beta$  is less than 1, such as in the corona, the Lorentz force overcomes the pressure gradient and the gravity,  $0 = \mathbf{J} \times \mathbf{B}$ , namely, the current is parallel to the field. Since the electric current is proportional to  $\nabla \times \mathbf{B}$ , we can see

$$\nabla \times \mathbf{B} = \alpha \mathbf{B}, \quad (6.1)$$

where  $\alpha$  is the force-free parameter.

Seehafer (1990) summarized the previous reports and confirmed the dominance of left-handed (right-handed) over right-handed (left-handed) spiral structures of the active regions in the northern (southern) hemisphere, regardless of magnetic polarity and of the activity cycle. That is, force-free parameter  $\alpha$  is negative (positive) in the northern (southern) hemisphere.

Using vector magnetograms, Pevtsov et al. (1995) found the hemispheric rule of  $\alpha$ . They determined a best-fit single value  $\alpha_{\text{best}}$  for a whole active region to reduce the influ-

ence of single pixel noise.  $\alpha_{\text{best}}$  is the value for which the computed transverse field (computed from observed longitudinal field by assuming constant- $\alpha$  force-free field) is best matched with the observed transverse field for a whole region. The mean values of  $\alpha_{\text{ave}}$  (average values of several  $\alpha_{\text{best}}$  of each active region) are about  $-9 \times 10^{-9} \pm 3 \times 10^{-9} \text{ m}^{-1}$  in the northern hemisphere and  $5 \times 10^{-9} \pm 4 \times 10^{-9} \text{ m}^{-1}$  in the southern hemisphere. Pevtsov et al. (1997) also calculated the coronal twist  $\alpha_c$ . They modeled dipole force-free field for a certain  $\alpha$  and determined the shear angle  $\gamma$  between the axis of two polarities and the field line whose projection onto the horizontal plane passes through the central point of the active region. Here,  $\alpha_c$  is the value for which the angle  $\gamma$  fits the X-ray image of the active regions taken by *Yohkoh* satellite. As a result,  $\alpha_p$  (the previous  $\alpha_{\text{ave}}$ ) is strongly correlated with  $\alpha_c$ , and its value is about  $\pm 2 \times 10^{-8} \text{ m}^{-1}$ .

Leka et al. (1996) found that  $\alpha$  increases as the flux emerges, and concluded that the emerging region carries current and twist generated below the photosphere. Leka & Skumanich (1999) and Leka (1999) convinced the consistency of the three types of  $\alpha$ : (1) parameterized  $\alpha(x, y)$  using moments of its distribution, (2) the slope of the function  $J_z(x, y) = \alpha B_z(x, y)$ , and (3)  $\alpha_{\text{best}}$  in Pevtsov et al. (1995).

Longcope & Klapper (1997) derived the equations for a twisted thin flux tube (TFT) and showed the relation

$$q = \frac{\alpha}{2}. \quad (6.2)$$

Also their model predicted a magnitude of  $\alpha \sim 2 \times 10^{-9} \text{ m}^{-1}$ , which is slightly smaller than that observed by Pevtsov et al. (1995). In Longcope et al. (1999), they assumed that the twist of flux tube is caused by helical turbulence ( $\Sigma$ -effect) in the convection zone, and reproduced the observed dependence of  $\alpha$  on latitude by the Coriolis effect. Through a dynamical model, Longcope & Welsch (2000) explained the observation by Pevtsov et al. (1997) that the emerged coronal field has an electric current and that  $\alpha_p$  is consistent with  $\alpha_c$ . In their model, the difference between the coronal and the photospheric twists is

relaxed in about a day by the torsional Alfvén wave propagating downward along the flux tube and the subsequent photospheric rotation.

Pevtsov et al. (2003) observed the evolution of the twist in the coronal fields of active regions  $\alpha_c$ . They found that the twist increases as the region grows. The twist reaches the plateau within approximately 1 day, while the growth of the region (e.g. the separation of two polarities) stops after 1.5 day. Following the work by Longcope & Welsch (2000), they developed a model for the helicity injection to the corona, and implied that the helicity is carried by twisted flux tubes.

Table 6.1 shows the quantitative summary of the twist  $q (= \alpha/2)$ . From the observa-

Table 6.1: Quantitative Summary of twist  $q$  in flux tubes (Longcope et al., 1999).

	$q$ ( $\text{m}^{-1}$ )	Reference
<b>Observations</b>		
Active region	$\sim 1 \times 10^{-8}$	Pevtsov et al. (1995)
Substructures	$\sim 2 \times 10^{-7}$	Leka et al. (1996)
<b>Constraints on twist</b>		
Integrity of tube	$\gtrsim 1 \times 10^{-7}$	Emonet & Moreno-Insertis (1998)
Kink stable		Linton et al. (1996)
overshoot	$\lesssim 5 \times 10^{-7}$	
always	$\lesssim 1 \times 10^{-7}$	
<b>Source of the twist</b>		
Joy's law	$\sim 1 \times 10^{-9}$	Longcope & Klapper (1997)
Differential rotation	$\sim 2 \times 10^{-9}$	
$\Sigma$ -effect	$\sim 2 \times 10^{-8}$	Longcope et al. (1998)
Created in dynamo	$\sim 4 \times 10^{-11}$	

tions, the typical value of photospheric and coronal twists is found to be  $q \sim 10^{-8} \text{ m}^{-1}$ . However, the expected tube's twist so as the tube not to be disintegrated during the emergence through the convection zone is  $q \gtrsim 10^{-7} \text{ m}^{-1}$  (obtained by Equation (4.2)), while, for the tube to be kink stable,  $q \lesssim 10^{-7} \text{ m}^{-1}$ . In other words, the observed twist is much less than the theoretically expected value. This problem is important for understanding the flux emergence and the corresponding formation of active region.

In this Chapter, we perform three-dimensional simulations of the twisted emerging flux tube from the uppermost convection zone to the corona. The aim is to study the

effect of the initial twist on the emergence process. A series of parametric studies on the flux tube's twist was done by Murray et al. (2006). Our work is dedicated to further detailed analyses, especially focusing on the effect of the initial twist on the resulting tube's structure (photospheric lateral expansion and multiple magnetic domes) and on the consequent coronal magnetic energy.

For numerical experiments, we used the same conditions as those by Murray et al. (2006); we calculated ten cases of different twist parameters that cover their three runs. As a result of experiments, we found that the evolution depends on the initial twist. When the twist is strong enough, the evolution to the corona reveals two-step way, showing a deceleration and a lateral expansion near the solar surface, although the case with weaker twist spends more time waiting for the secondary emergence to occur (Magara, 2001; Archontis et al., 2004; Murray et al., 2006). This picture of the two-step emergence is highly consistent with recent observations by Otsuji et al. (2010), especially its horizontally expanding speed and the rising speed. In addition to the confirmation of the results by Murray et al. (2006), it is also found that multiple magnetic domes are built and plasma accumulates in between the domes when the secondary emergence starts. At this moment, the direction of the field lines is almost perpendicular to the alignment of the domes, indicating that the second-step emergence is due to the interchange-mode instability. If the initial twist is too weak, the tube extends widely near the surface and further evolution never takes place, because the magnetic tension force of the azimuthal component cannot hold the tube's coherency.

Also, we newly found that the total magnetic energy measured above the surface relies on the initial twist. In the strong twist regime, the resulting magnetic energy follows the initial relation between the twist and the magnetic energy. In the weak twist regime, however, the magnetic energy deviates from the initial rule, because the tube with weak twist stores magnetic energy around the photosphere.

The rest of this Chapter is organized as follows. In Section 6.2, we describe the numerical model. The simulation results are shown in Section 6.3. Summary and discussion

are given in Section 6.4 and 6.5, respectively.

## 6.2 Numerical Setup

In numerical simulations, we solve nonlinear, time-dependent, compressible three-dimensional MHD equations given in Chapter 2. For comparison of numerical results with observations, we use normalizing units of length  $H_0 = 170$  km, speed  $C_{\text{s}0} = 6.8$  km s $^{-1}$ , time  $\tau_0 = H_0/C_{\text{s}0} = 25$  s, and density  $\rho_0 = 1.4 \times 10^{-7}$  g cm $^{-3}$ , which are typical values for the solar photosphere. Then, pressure  $p_0 = \rho_0 C_{\text{s}0}^2 = 6.3 \times 10^4$  dyn cm $^{-2}$ , temperature  $T_0 = mC_{\text{s}0}^2/(\gamma k_{\text{B}}) = 5600$  K, magnetic field strength  $B_0 = (\rho_0 C_{\text{s}0}^2)^{1/2} = 250$  G, and energy  $E_0 = \rho_0 C_{\text{s}0}^2 H_0^3 = 3.1 \times 10^{26}$  erg, where  $\gamma = 5/3$  is a specific heat ratio,  $k_{\text{B}}$  the Boltzmann constant, and  $m$  the mean molecular mass.

The initial background stratification consists of three regions: an adiabatically stratified convective layer, a cool isothermal photosphere/chromosphere (afterward, we simply call it photosphere), and a hot isothermal corona. The photosphere and the corona are smoothly connected by the transition region. We take  $z/H_0 = 0$  to be the base height of the photosphere, and the starting height of the transition region and the corona are  $z_{\text{tr}}/H_0 = 10$  and  $z_{\text{cor}}/H_0 = 20$ , respectively. The initial temperature of the photosphere and the corona are  $T_{\text{ph}}/T_0 = 1$  and  $T_{\text{cor}}/T_0 = 150$ , respectively. The background temperature distribution in the transition region is given by

$$\frac{T_s(z)}{T_0} = \left( \frac{T_{\text{cor}}}{T_{\text{ph}}} \right)^{(z-z_{\text{tr}})/(z_{\text{cor}}-z_{\text{tr}})}, \quad (6.3)$$

and that of the convection zone being

$$\frac{T_s(z)}{T_0} = 1 - \frac{z}{T_0} \left| \frac{dT}{dz} \right|_{\text{ad}}, \quad (6.4)$$

where

$$\left| \frac{dT}{dz} \right|_{\text{ad}} = \frac{\gamma - 1}{\gamma} \frac{mg_0}{k_B} \quad (6.5)$$

is the adiabatic temperature gradient (subscript s is for surrounding distribution). The initial gas pressure and density profiles are defined by solving one-dimensional hydrostatic equation

$$\frac{d}{dz} p_s(z) + \rho_s(z) g_0 = 0 \quad (6.6)$$

and the equation of state

$$p_s(z) = \frac{k_B}{m} \rho_s(z) T_s(z) \quad (6.7)$$

on the basis of the temperature distribution above.

The initial magnetic flux tube is embedded in the convection zone at  $z_{\text{tube}}/H_0 = -10$ . The longitudinal and azimuthal component of the flux tube are described as follows: for a radial distance from the axis  $r = [(y - y_{\text{tube}})^2 + (z - z_{\text{tube}})^2]^{1/2}$ ,

$$B_x(r) = B_{\text{tube}} \exp \left( -\frac{r^2}{R_{\text{tube}}^2} \right), \quad (6.8)$$

and

$$B_\phi(r) = qr B_x(r), \quad (6.9)$$

where  $(y_{\text{tube}}, z_{\text{tube}}) = (0, -10H_0)$  is the tube center,  $R_{\text{tube}}$  the radius,  $q$  the twist parameter, and  $B_{\text{tube}}$  the magnetic field strength at the axis. We take  $R_{\text{tube}}/H_0 = 2.5$  and  $B_{\text{tube}}/B_0 = 15$ , i.e., these parameters are almost the same as those of Murray et al. (2006). For pressure balance between the flux tube and the surrounding medium, the gas pressure

inside the tube is obtained as  $p_i = p_s + \delta p_{\text{exc}}$ , where

$$\delta p_{\text{exc}} = \frac{B_x^2(r)}{8\pi} \left[ q^2 \left( \frac{R_{\text{tube}}^2}{2} - r^2 \right) - 1 \right]. \quad (6.10)$$

The density inside the tube is also defined as  $\rho_i = \rho_s + \delta\rho_{\text{exc}}$ , where

$$\delta\rho_{\text{exc}} = \frac{\delta p_{\text{exc}}}{p_s} \rho_s \exp\left(-\frac{x^2}{\lambda^2}\right), \quad (6.11)$$

and  $\lambda/H_0 = 20$ . That is, the flux tube is most buoyant at the middle of the tube ( $x/H_0 = 0$ ), and the buoyancy diminishes as  $|x|$  increases.

Here, we investigate ten parameters of  $q$ , which are  $qH_0 = 0.5, 0.4, 0.3, 0.25, 0.2, 0.175, 0.15, 0.125, 0.1$ , and  $0.05$ . The plasma beta ( $\beta \equiv 8\pi p/B^2$ ) at the tube center is  $\beta \sim 3$  at the initial state. The initial background stratification (gas pressure, density, and temperature) and the magnetic pressure along  $x/H_0 = y/H_0 = 0$  of the case  $qH_0 = 0.2$  are indicated in Figure 6.1.

The simulation domain is taken as  $(-120, -120, -20) \leq (x/H_0, y/H_0, z/H_0) \leq (120, 120, 150)$ , resolved by  $256 \times 256 \times 256$  grids. The grid spacings for  $x$ ,  $y$ , and  $z$  directions are  $\Delta x/H_0 = \Delta y/H_0 = 0.5$  for  $(-40, -40) \leq (x/H_0, y/H_0) \leq (40, 40)$ , and  $\Delta z/H_0 = 0.2$  for  $-20 \leq z/H_0 \leq 20$ , respectively. Outside this range, the mesh size gradually increases. We assume periodic boundaries for horizontal directions and symmetric for vertical. A wave-damping region is attached near the top boundary.

## 6.3 Results

### 6.3.1 Overview of the Results

Figure 6.2 shows the time evolution of the flux tube with the twist  $qH_0 = 0.2$ . In this Figure, we plot the logarithmic field strength  $\log(|B|/B_0)$  and the photospheric magnetogram  $B_z/B_0$ . In each panel, the region  $x/H_0 \leq 0$  and  $y/H_0 \geq 0$  is shown. Initially, the

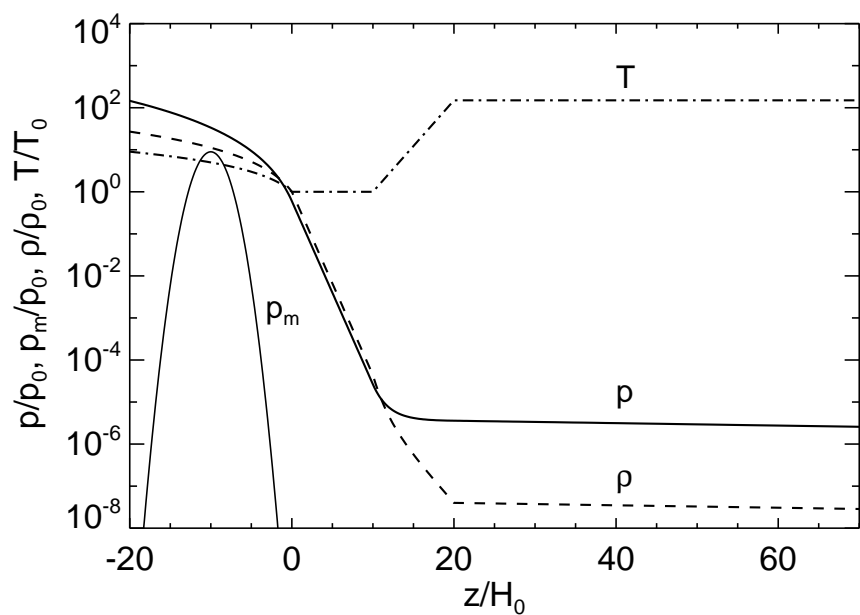


Figure 6.1: One-dimensional ( $z$ -)distributions of the initial background density (thick solid line), pressure (dotted line), and temperature (dashed line). The magnetic pressure  $p_m = B^2/(8\pi)$  of the tube  $qH_0 = 0.2$  along the vertical axis  $x/H_0 = y/H_0 = 0$  is overplotted with a thin solid line.

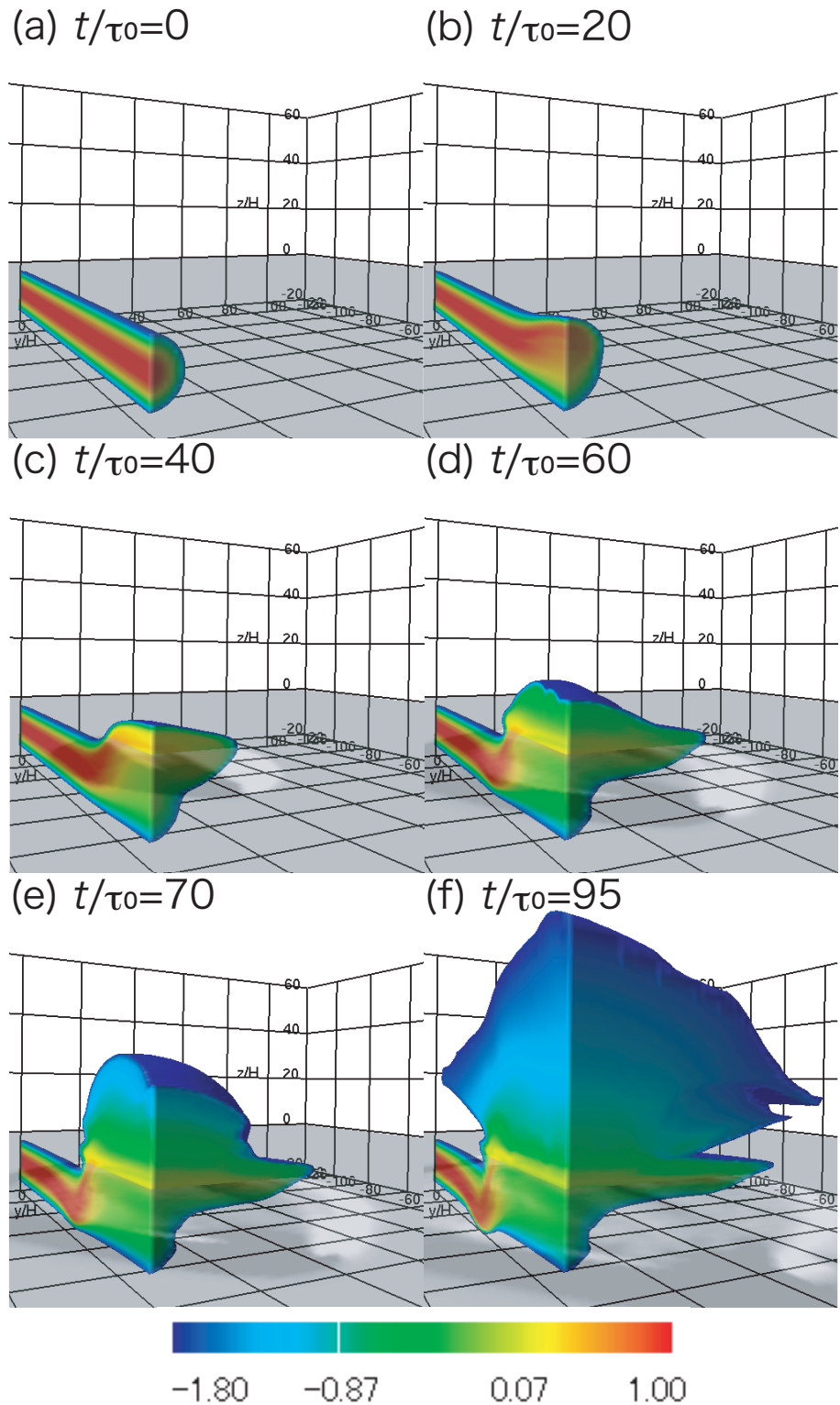


Figure 6.2: Time evolution of the flux tube with the twist  $qH_0 = 0.2$ . Logarithmic field strength  $\log(|B|/B_0)$  and photospheric magnetogram  $B_z/B_0$  are plotted. In each panel, the region  $x/H_0 \leq 0$  and  $y/H_0 \geq 0$  is shown.

flux tube is embedded at  $z_{\text{tube}}/H_0 = -10$ , and is slightly buoyant around the tube center  $-20 < x/H_0 < 20$ . The tube rises through the convection zone by magnetic buoyancy, and reaches the surface at  $t/\tau_0 = 20$  (Figure 6.2(b)), while the outskirt of the rising portion ( $x/H_0 \sim -20$ ) begins to sink, because the fluid is drained along the field lines from the apex of the rising tube. Due to the isothermal (i.e., strongly-subadiabatic) photosphere, the tube is decelerated and expands laterally near the surface to make a “photospheric tongue” (Figure 6.2(c)). That is, the convectively stable photosphere inhibits an upward motion of the fluid, and thus, the magnetic field cannot penetrate the photosphere only to escape in the horizontal direction. (It should be noted that the term “tongue” here is different from that used in Li et al. (2007) and Archontis & Hood (2010).) The horizontal extension of the magnetic field is also observed in a recent radiative MHD calculation by Cheung et al. (2010). The lateral expansion speed is  $|V_y| \sim 0.4C_{s0} = 2.7 \text{ km s}^{-1}$ , i.e., a fraction of the photospheric sound speed. At this moment, the photospheric magnetogram shows a north-south ( $y$ -directional) magnetic distribution, and the total field strength is  $|B| \sim 2B_0 = 500 \text{ G}$  and plasma beta is  $\beta \equiv p/p_{\text{mag}} \sim 2$  around the photosphere.

As the magnetic pressure gradient enhances, the second-step emergence takes place. In Figure 6.2(d), multiple expansions are observed: the rise velocity is about  $(0.3\text{--}0.5)C_{s0} = (2.0\text{--}3.4) \text{ km s}^{-1}$ . This multi-dome structure is more noticeable in a weaker twist case. Figure 6.3(a) shows the magnetic field structure of the case  $qH_0 = 0.15$  at  $t/\tau_0 = 80$ . The corresponding density structure and velocity vectors in the  $y/H_0 = 0$  plane, and the field lines are indicated in Figure 6.3(b). From these figures, one can see four magnetic domes are built and the fluid is accumulated between the domes. In this region, the field lines are generally directed in the  $y$ -direction. Therefore, this situation can be explained as a consequence of the interchange mode of the magnetic buoyancy instability, i.e., the wavenumber vector is perpendicular to the field lines.

As time goes on, the flux tube expands both vertically and horizontally, while the photospheric tongue also continues to expand laterally (Figure 6.2(e)). Finally, the flux tube makes a single dome of the height  $z/H_0 \sim 60$  on the pancake-like structure at the

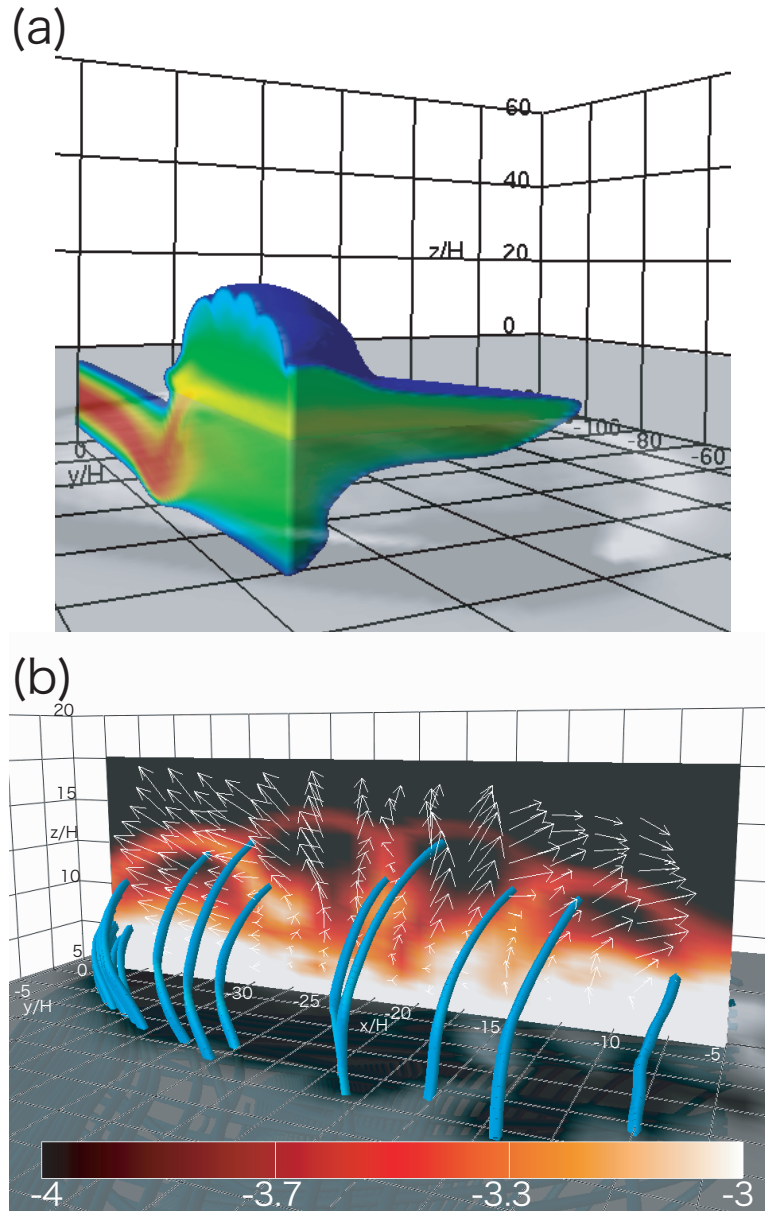


Figure 6.3: The flux tube with  $qH_0 = 0.15$  at the time  $t/\tau_0 = 80$ . (a) Magnetic field structure  $\log(|B|/B_0)$  and photospheric magnetogram  $B_z/B_0$ . Plotted colors are the same as those of Figure 6.2. (b) The corresponding logarithmic density profile  $\log(\rho/\rho_0)$  at  $y/H_0 = 0$  plane ( $-40 \leq x/H_0 \leq -5$  and  $5 \leq z/H_0 \leq 17.5$ ) with velocity vectors (white arrows), magnetogram at  $z/H_0 = 5$ , and field lines (blue lines) are shown.

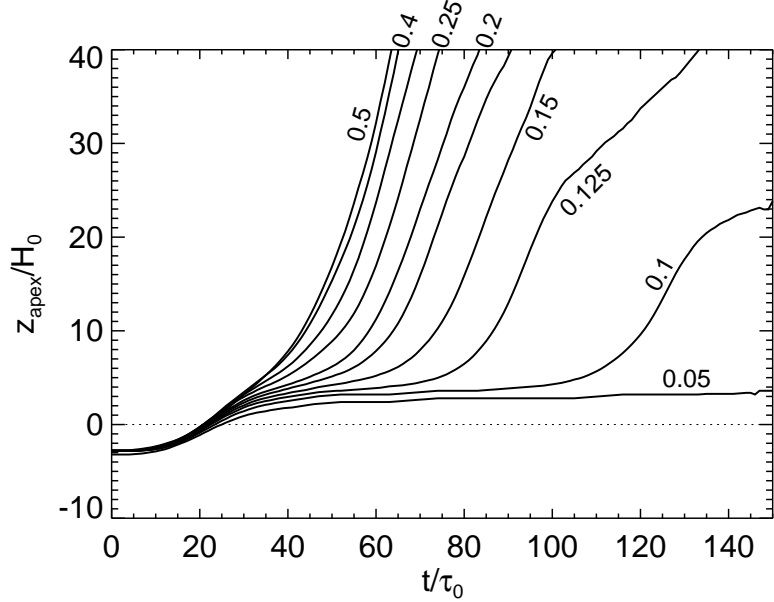


Figure 6.4: Height-time relations for various twist cases. From left to right, each line shows the evolution of  $qH_0 = 0.5, 0.4, 0.3, 0.25, 0.2, 0.175, 0.15, 0.125, 0.1, \text{ and } 0.05$ . It takes more time to rise into the corona as the twist strength decreases.

surface (Figure 6.2(f)). At the same time, the sunk part approaches the bottom of the simulation domain ( $z/H_0 \sim -20$ ).

Overall evolution described above is similar to the observation by Otsuji et al. (2010). They found the lateral expansion with the speed of  $2.9 \text{ km s}^{-1}$  at the surface before further evolution occurred, which is consistent with our results of  $|V_y| = 2.7 \text{ km s}^{-1}$ . The gradual rise speed of the secondary emergence was observed to be  $2.1 \text{ km s}^{-1}$ , which is also consistent with our results of  $(2.0\text{--}3.4) \text{ km s}^{-1}$ .

### 6.3.2 Parameter Study on the Twist Strength

Figure 6.4 shows the height-time relation of the top of the tube for various twist cases. Here, in this figure, we plot the height at the highest portion of the emerging flux tube ( $z_{\text{apex}}/H_0$ ). The evolutions are found to depend on the initial twist, and each line distributes in a continuous fashion. It can be seen from this figure that almost all the tubes ( $0.5 \geq qH_0 \geq 0.1$ ) show the two-step emergence to the corona. Although the rise times

within the convection zone are similar to each other, tubes with weaker twists spend more time in the surface waiting for the second-step emergence to be triggered. The tube with  $qH_0 = 0.1$  shows only a slight emergence in the atmosphere ( $z/H_0 \lesssim 20$ ). As for the weakest twist case with  $qH_0 = 0.05$ , further evolution never takes place within the elapse calculated (failed emergence). These results are consistent with those of Magara (2001), Murray et al. (2006), and the work in Chapter 4.

Cross-sections at  $x/H_0 = 0$  plane of eight out of ten flux tubes are shown in Figure 6.5. These tubes are those who reach  $z/H_0 = 40$ , and each figure shows the arrival at that height. As the initial twist  $qH_0$  becomes smaller, the lateral expansion at the surface (tongue-like structure around  $z/H_0 \sim 0$ ) is increasingly remarkable, because the more intense initial twist of the magnetic flux tube yields the stronger azimuthal magnetic tension force, and thus keeps the tube coherent. Therefore, the coronal field intensity also reduces with decreasing  $qH_0$ , and the coronal structure with a weaker twist is more fragmented compared to the stronger twist cases.

### 6.3.3 Comparison of the Magnetic Field Structure at the Surface

In this Subsection, we compare the magnetic field structures of the different emergence cases to study the horizontal expansion and the mechanism of the second-step evolution at the solar surface. Figure 6.6 shows (*top*) the cross-sectional configuration of the flux tubes at  $x/H_0 = 0$  with velocity vectors, (*middle*) the horizontal components of forces along the horizontal axis  $x/H_0 = z/H_0 = 0$ , and (*bottom*) the vertical components of forces along the vertical axis  $x/H_0 = y/H_0 = 0$  for cases with  $qH_0 = 0.4$  (rapid emergence), 0.15 (slow emergence), and 0.05 (failed emergence) at the time  $t/\tau_0 = 40$ .

As can be seen from the top figures, the second-step evolution has already begun at this time for the case with  $qH_0 = 0.4$ , while the vertical expansion cannot be seen in  $qH_0 = 0.05$  case. It should be noted that the downflow in the uppermost areas in Figures 6.6(b) and (c) is a reflected wave from the top boundary. Horizontally, for a strongest

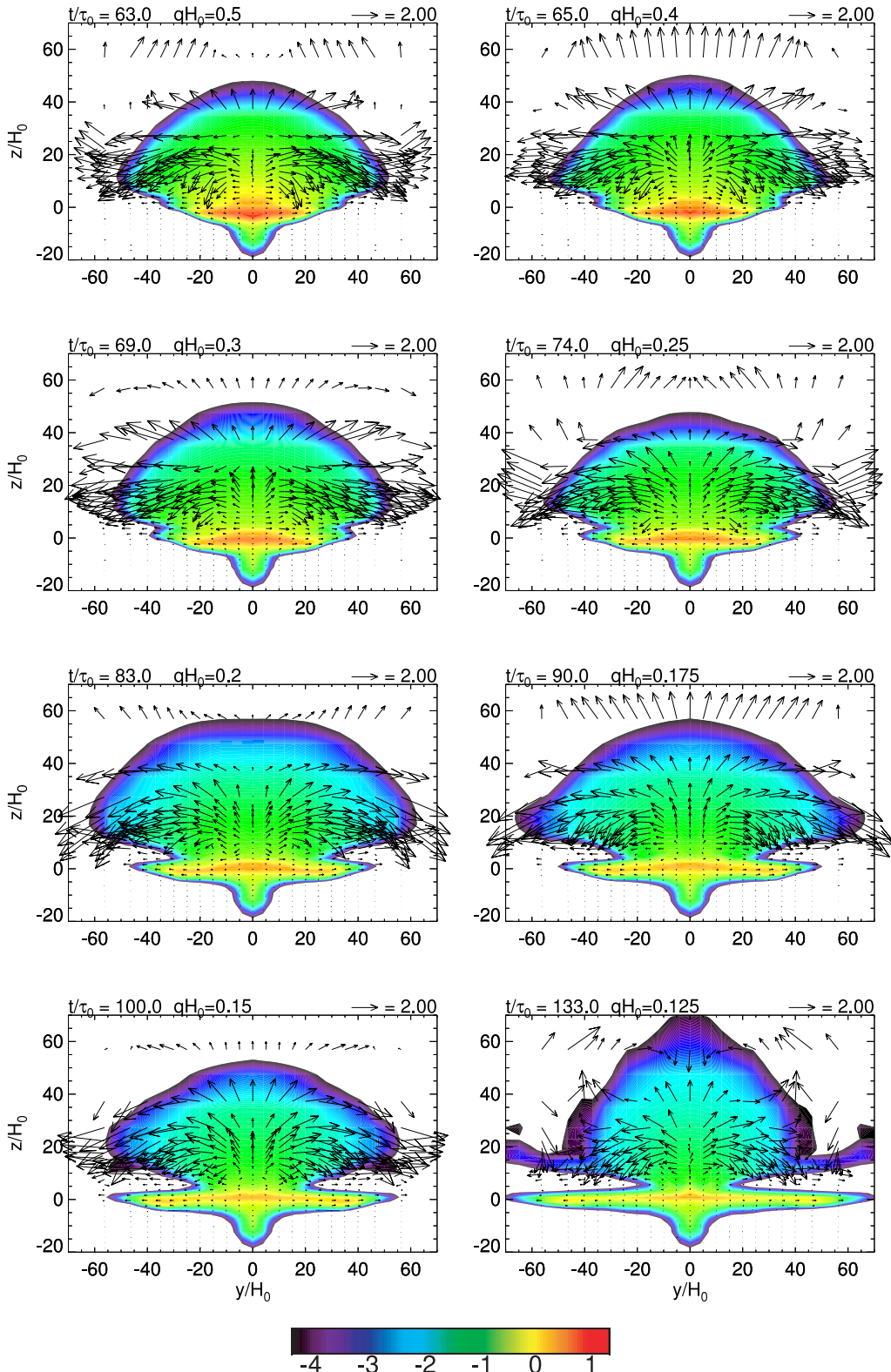


Figure 6.5: Cross-sections at  $x/H_0 = 0$  plane of eight out of ten flux tubes that reach  $z/H_0 = 40$ . Each figure shows the logarithmic field strength  $\log(|B|/B_0)$  when the tube reaches that height.

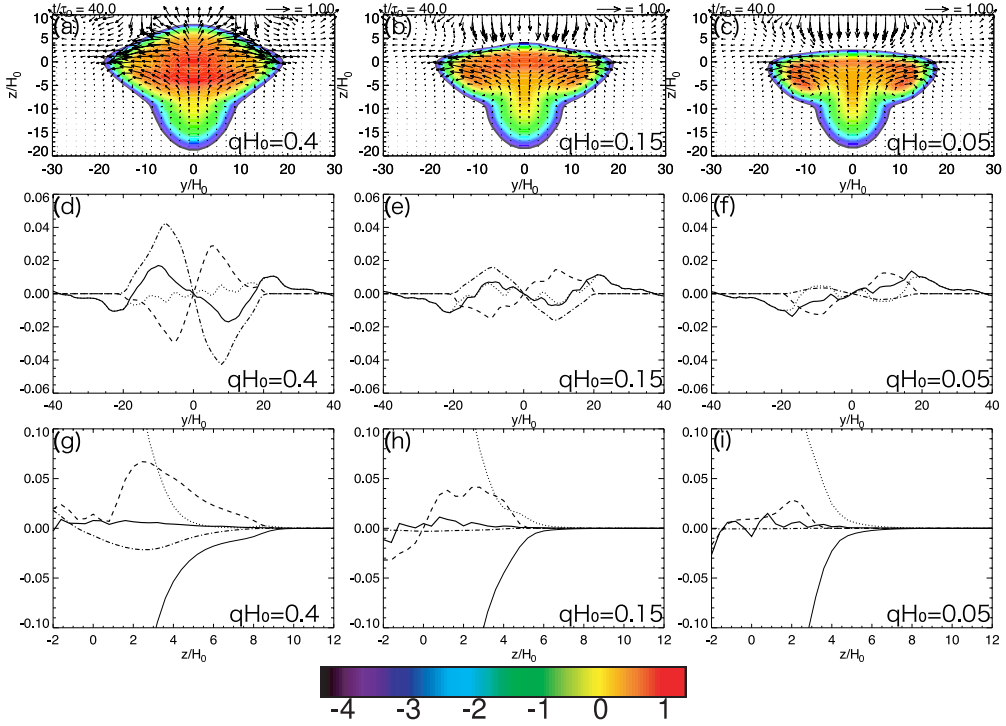


Figure 6.6: (Top) Cross-sectional configuration of the flux tubes at  $x/H_0 = 0$  with velocity vectors, (middle) horizontal components of each force along the horizontal axis  $x/H_0 = z/H_0 = 0$ , and (bottom) vertical components of forces along the vertical axis  $x/H_0 = y/H_0 = 0$  for cases with  $qH_0 = 0.4$  (rapid emergence), 0.15 (slow), and 0.05 (failed) at the time  $t/\tau_0 = 40$ . Plotted lines are the total force (thick solid line), gas pressure gradient (dotted), magnetic pressure gradient (dashed), magnetic tension (dash-dotted), and gravity (thin solid), respectively.

twist case (Figure 6.6(d)), an inward magnetic tension force is dominant, and thus the inward total force keeps the tube from a lateral fragmentation. As the twist decreases, the magnetic tension reduces so that the total force is outward in a wider range for  $qH_0 = 0.05$  (Figure 6.6(f)), resulting in the tube's fragmentation and the further expansion never to occur. As for vertical forces, magnetic pressure gradient is principal at front of the tube (Figure 6.6(g)):  $3 < z/H_0 < 9$ ). However, the total force is about zero within this area. That is, the second-step expansion is caused by the tube's magnetic pressure, while the tube is almost in a hydrostatic equilibrium with surrounding materials. For a weak twist case (Figure 6.6(i)), the magnetic pressure gradient is much less effective. Therefore, further rise cannot occur.

### 6.3.4 Undulating Configuration of the Photospheric Field Lines

Figure 6.7 shows the surface magnetogram  $B_z/B_0$  and the field lines above the surface for the medium twist case ( $qH_0 = 0.15$ ) at the time  $t/\tau_0 = 125$ , namely, in the later phase. We confirm that some undulating field lines connect magnetic patches at the surface, and that, as time goes on, they gradually rise into the corona by forming longer fields. At this time, both near-surface undulating fields and coronal fields are directed almost parallel to the axis of the original flux tube, which is in contrast to the perpendicular fields observed in the earlier phase of the emergence (see Figure 6.3(b)). This result is reminiscent of the “sea-serpent” field lines and the resistive emergence by Pariat et al. (2004). Undulating photospheric fields of a weakly twisted tube are also found by Archontis & Hood (2010). We will discuss this again in Section 6.5.

### 6.3.5 Magnetic Energy in the Atmosphere and the Initial Tube's Twist

Figure 6.8 shows the initial twist  $qH_0$  and the total magnetic energy measured above the solar surface  $E_{\text{mag}}/E_0$  when each tube arrives at  $z/H_0 = 40$  (see Figure 6.5). The

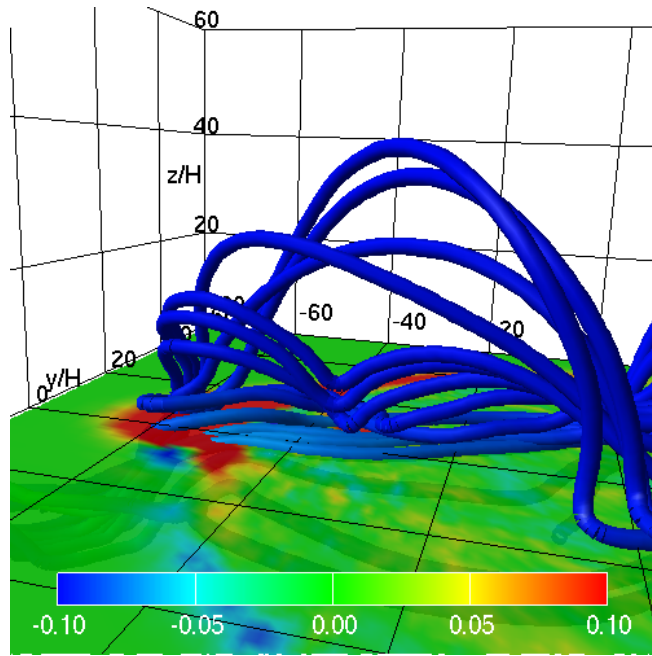


Figure 6.7: Surface magnetogram  $B_z/B_0$  (color contour) and the field lines (blue lines) for the middle twist case ( $qH_0 = 0.15$ ) at the time  $t/\tau_0 = 125$  are shown. Note that some field lines undulate near the surface and gradually rise into the corona as longer loops.

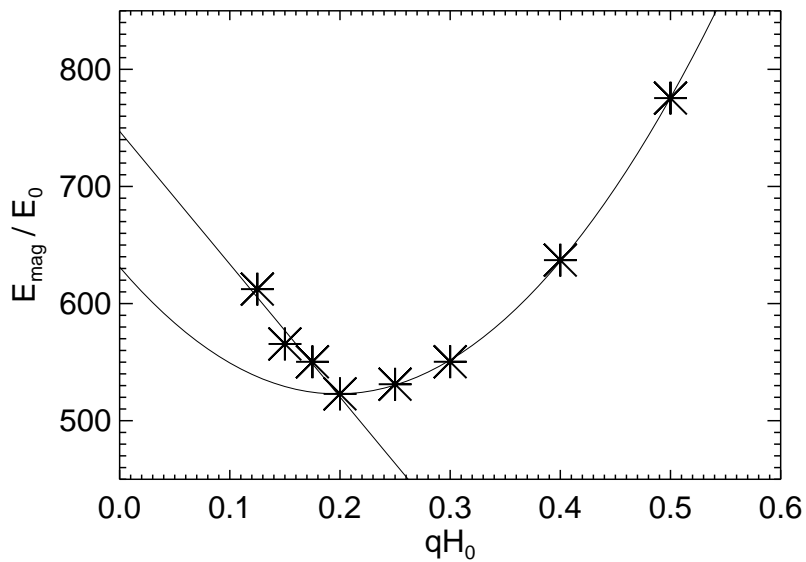


Figure 6.8: Total magnetic energy above the surface  $E_{\text{mag}} = \int_{z>0} B^2/(8\pi) dV$  versus the initial twist  $q$ , measured at the time when each tube reaches  $z/H_0 = 40$ . Quadratic and linear lines are overplotted with solid lines.

magnetic energy above the surface is defined as:

$$E_{\text{mag}} = \int_{z>0} \frac{B^2}{8\pi} dV. \quad (6.12)$$

When the initial twist is large ( $qH_0 \geq 0.2$ ), the magnetic energy  $E_{\text{mag}}$  is found to obey a  $q^2$  law. From the field configuration (6.8) and (6.9), the initial magnetic energy per unit volume can be calculated as

$$\frac{B^2}{8\pi} = (q^2 r^2 + 1) \frac{B_{\text{tube}}^2}{8\pi} \exp\left(-\frac{2r^2}{R_{\text{tube}}^2}\right), \quad (6.13)$$

that is, the initial tube's magnetic energy depends on  $q^2$ . When the twist is strong, the azimuthal magnetic tension force is more effective and the lateral expansion around the photosphere is less efficient that the initial magnetic energy is directly transported into the atmosphere above the surface. As a result of this regime, the observed magnetic energy within the atmosphere relies on a  $q^2$  function.

Contrary to this, when the initial twist is weak ( $qH_0 \leq 0.2$ ), the consequent magnetic energy deviates from the  $q^2$  line and is negatively-correlated with the initial twist. It is speculated that, for these tubes with weaker twists, it takes a longer time to reach  $z/H_0 = 40$  from the surface. It is because the photospheric field needs more time to satisfy the condition for the second-step emergence (i.e. Acheson, 1979), for the weak azimuthal field causes the tube to expand horizontally around the surface. Since the magnetic energy is continuously transported from below and the horizontal expanding velocity is almost the same for  $qH_0 \leq 0.2$  cases ( $V_y/C_{s0} \sim 0.1$ ), the magnetic energy of the photospheric tongue is expected to depend on the time lag between the tube's arrival at the photosphere and at  $z/H_0 = 40$ .

It can be concluded that the magnetic energy in the atmosphere correlates critically with the initial twist. In the strong twist regime, the energy-twist relation follows the initial  $q^2$  rule, because the tightly twisted tube does not exhibit a significant expansion

near the photosphere. As for the weak twist cases, they depend on the time lag between reaching the photosphere and the corona. It is because the weaker twist tube takes more time to rise further, and, therefore, more magnetic energy is stored in the photospheric tongue.

## 6.4 Summary

In this Chapter, we carried out three-dimensional MHD simulations to investigate the effect of the initial twist on the flux tube evolution. Here, we summarize the results:

- Initially, the flux tube rises through the convection zone due to its magnetic buoyancy. Reaching the surface, the tube expands laterally to make a “photospheric tongue.” The secondary emergence occurs after sufficient flux accumulates within the photosphere. Due to the interchange mode instability, the tube builds multiple domes above the surface, between which the fluids piles up. Finally, the flux tube arrives at  $z/H_0 \sim 60$  as a single dome. The overall emergence is consistent with the recent observations (e.g. Otsuji et al., 2010).
- We run ten twist cases to investigate the effect of the initial twist. Nine out of ten reach the coronal height ( $z/H_0 \geq 20$ ) showing two-step emergence, while the weakest twist case fails to rise further above the surface ( $qH_0 = 0.05$ ). In the two-step emergence regime, the rise time becomes shorter with increasing initial twist, which is consistent with the previous calculations by Murray et al. (2006). The photospheric tongue is more noticeable in weaker twist case.
- We study the force components at the solar surface for different twist cases at the time  $t/\tau_0 = 40$ . The stronger the initial twist is, the larger the inward magnetic tension is, resulting the tube keeps its coherency. In the weak twist case, the magnetic tension is much less effective, causing the tube distorted. At the same time, the

strong twist tube rises further into the atmosphere mainly by the magnetic pressure gradient.

- We found that the photospheric fields of the middle twist case ( $qH_0 = 0.15$ ) undulate in the later phase of the emergence. The field lines gradually rise into the corona as longer loops. The photospheric and coronal fields are almost parallel to the axis of the initial flux tube. These features remind us of the resistive emergence model by Pariat et al. (2004).
- We measure the magnetic energy  $E_{\text{mag}}$  above the surface. The energy plot follows the initial  $q^2$  law when the twist is strong ( $qH_0 \geq 0.2$ ), while, for weaker twist cases ( $qH_0 \leq 0.2$ ), the energy depends on the time difference between reaching the surface and the corona. That is, weakly twisted tube takes more time for magnetic flux to accumulate near the surface and the secondary instability to be triggered.

## 6.5 Discussion

In Section 6.3, we showed the time-evolution of the twisted flux tube. When the second-step emergence starts, multiple domes are observed above the surface and fluid is trapped between the expanding magnetic structures (see Figure 6.3). At this time, field lines are directed perpendicular to the alignment of the magnetic domes. For middle twist tube, we also found undulating fields near the surface, emerging into the corona (see Figure 6.7).

In this Section, we discuss these features in connection with future observations.

### 6.5.1 Twist Intensity and the Interchange Instability

In Section 6.3.1, we saw that, as the twist decreases, the interchange mode instability becomes more noticeable. However, this is contrary to the expectation that the azimuthal field should be less pronounced in a weaker twist case. It may be because, in a weak twist case, the tube extends laterally near the photosphere and thus the twist increases. As the

tube develops the interchange instability, field lines perpendicular to the alignment of the magnetic domes become more pronounced (see Sections 6.3.2 and 6.3.3).

### 6.5.2 Twist of the Actual Flux Tube in the Sun

Multiple magnetic structures and the density accumulation between them are also found in previous observations and calculations. Pariat et al. (2004) found that photospheric fields are undulating at its earlier phase of the flux emergence event, and proposed a resistive emergence model that undulating multiple loops reconnect with each other to make larger coronal fields. Isobe et al. (2007) carried out two-dimensional MHD simulation to study the evolution of the serpentine magnetic loops (resistive emergence model), finding that density accumulates in between the magnetic loops; their elongated vertical plasma structures are similar to our results (for three-dimensional study, see Archontis & Hood (2009)). However, in our model, field lines are directed almost perpendicular to the alignment of the domes, which is against the observations of the undular field lines (e.g. Pariat et al., 2004). The direction of the field lines are the consequence of the initial tube's twist. Therefore, the difference between the present calculations and the observations indicates that the actual twist of the flux tube beneath the surface may be much weaker than those assumed in our models (e.g.  $q = 0.15/H_0 = 8.8 \times 10^{-4} \text{ km}^{-1}$  for Figure 6.3).

On the other hand, flux tube with insufficient twist was found to fail to rise through the convection zone (Moreno-Insertis & Emonet, 1996; Emonet & Moreno-Insertis, 1998, and the work in Chapter 4). It is because the weak azimuthal field of the flux tube cannot hold its coherency during its ascent within the solar interior. Therefore, one of the important problems to be solved is the emergence of the flux tube with much weaker twist ( $q \leq 0.1/H_0 = 5.9 \times 10^{-4} \text{ km}^{-1}$ ).

We also found that the medium twist tube ( $q = 0.15/H_0 = 8.8 \times 10^{-4} \text{ km}^{-1}$ ) reveals the undulating fields at the surface, which gradually rise into the upper atmosphere as longer coronal loops (Section 6.7). These fields are directed parallel to the main axis

of the initial flux tube. This picture seems well accorded with the resistive emergence model. However, it is in the later phase that this undulatory evolution is observed, and, in the earlier phase, the field lines are perpendicular to the original tube's axis (see Figure 6.3). Therefore, the reproduction of the undulating fields parallel to the original axis (Pariat et al., 2004) is not achieved.

### 6.5.3 Formation of Undulating Photospheric Fields

Recently, Cheung et al. (2010) have conducted a radiative MHD simulation of the formation of an active region. They showed that the rising flux tube flattens to make a pancake-like structure near the surface, and that the convective flows create serpentine field lines.

In the present study, which does not include the convection, we also found the sideway expansion of the rising field at the photosphere (tongue) and the undulation of the photospheric fields in the later phase of the emergence of the weaker twist tube. These features are also confirmed by Archontis & Hood (2010); their simulations do not take account of the convection effects, either. Therefore, we can see that other mechanisms, apart from the convection, could also explain the formation of serpentine fields at the photosphere.

### 6.5.4 For Future Observations

In this Chapter, we found some aspects of the flux emergence event. One is the photospheric tongue, i.e., the magnetic structure extending horizontally around the surface just before further evolution takes place. Temporally- and spacially-resolved spectroscopic observations of the earlier phase of the flux emergence are required to study this magnetic extension at the photosphere.

At the same time, we found that the initial twist of  $q \sim 0.1/H_0 = 5.9 \times 10^{-4} \text{ km}^{-1}$  at  $-1700 \text{ km}$  is too strong to match the observations (as mentioned above in Section 6.5.2). Local and global helioseismology are needed to reveal the flux emergence (especially on

the twist evolution) within the convection zone. The key issue is how weakly twisted flux tubes manage to rise through the solar interior.



# Chapter 7

## Summary

In this Thesis, we have performed four types of large-scale flux emergence simulation from the solar convection zone to the corona, passing through the photosphere. Three of them are the emergence from  $-20,000$  km. The first two are on the two-dimensional evolution, i.e., the undular mode emergence of a flux sheet (Chapter 3) and the cross-sectional emergence of a flux tube (Chapter 4). From parametric studies in the 2D experiments, we obtained preferable values of the magnetic flux that makes an actual active region: the field strength of  $10^4$  G, the total flux of  $(10^{21}-10^{22})$  Mx, and the sufficient twist  $> 2.5 \times 10^{-4} \text{ km}^{-1}$  (in the tube calculations) at  $-20,000$  km. Then we conducted a three-dimensional simulation of a flux tube by using these values (Chapter 5). Although there were some differences in physical quantities among three, the results were in qualitative agreement with one another. The other calculation in Chapter 6 intended to figure out the dependence of the flux evolution on the twist intensity of the initial tube.

In this Chapter, we will summarize the numerical results above.

### 7.1 Emergence from a Depth of -20,000 km

The outline of the flux emergence derived from the experiments from  $-20,000$  km is as follows. Initially, the magnetic flux at  $-20,000$  km starts rising through the convection zone due to its buoyancy. As the tube rises, the tube becomes into an arched shape, and

the rising portion expands because of the density decreasing with height. In the tube regime (in Chapter 4 for 2D tube and in Chapter 5 for 3D tube), the relative flow around the cross-section peels away the periphery of the tube, and the wake is formed behind the main tube.

As the emerging tube reaching the surface, it decelerates due to the photosphere in front. Here, we assume the photosphere as isothermally stratified, namely, convectively stable against the vertical motion of the fluid element. In the sheet emergence regime in Chapter 3, the plasma between the flux and the photosphere cannot pass through the surface with ease. And thus the plasma tends to pile up on the emerging sheet and makes it slow down. The deceleration by the fluid accumulation is also found in the tube calculation. As a result, the emerging flux gradually gathers around the photosphere to make a flat structure, and the rising speed drops to almost zero.

Since the magnetic flux is continuously transported from below, the surficial flux becomes fortified to make a top-heavy stratification. When the vertical gradient of the magnetic pressure at tube's apex steepens enough, the condition for the magnetic buoyancy instability is satisfied and the secondary emergence to the upper atmosphere starts. In the two-dimensional experiments, the magnetic pressure exerts only in the two directions, and thus the coronal loop reaches high in the atmosphere  $\sim 40$  Mm. In the 3D simulation, on the other hand, several magnetic domes emerge above the surface. At first, they expand two-dimensionally (collimated expansion) because of the obstruction by neighboring domes, and as time goes on, they as a whole expand in every direction (free expansion), and thus the domes reach only  $\sim 8$  Mm. Also, at the surface, several magneto patches separate to reach the outer edge of the active region, which is decided by the subsurface field, and make two alignments of pores there. As the inner field emerges, the direction of separations becomes inclined and the aligned pores move apart showing sheared motion. The schematic illustration of our model for flux emergence and the formation of active region derived from the 3D calculation is shown as Figure 5.16.

## 7.2 Dependence on the Initial Tube's Twist

From the parameter survey on tube's twist of the initial flux tube, we found that (1) the tube takes more time to emerge into the corona as the twist decreases, (2) if the twist is smaller than the critical value  $q = 0.05/H_0 = 2.5 \times 10^{-4} \text{ km}^{-1}$ , the secondary emergence never occurs, and (3) the magnetic energy measured above the surface increases with the tube twist in the stronger twist regime because of the initial twist law, while it decreases with twist in the weaker twist regime since the photospheric field extends narrower as the twist increases. The critical value obtained in this calculation ( $q = 2.5 \times 10^{-4} \text{ km}^{-1}$ ) is much larger than the observed value of  $2 \times 10^{-5} \text{ km}^{-1}$ .



# Chapter 8

## Discussion

In this Chapter, we will have discussions, especially from the points of thermal convection and the twist intensity of the flux tube.

### 8.1 Effect of Thermal Convection

In the calculations throughout the Thesis, we have neglected the effect of thermal convection. The convection is caused by the radiative cooling at the photosphere and the continuous energy transportation from the interior. In the upper convective layer, the ionizing energy of hydrogen drives the convection. The convections in the Sun form a hierarchy (see e.g. Miesch, 2005). The small-scale convective cells called granulation ( $\sim (1\text{--}2)$  Mm) dominates the surface, and there are also larger-scale convections such as mesogranulation ( $\sim 5$  Mm) and supergranulation ( $\sim 30$  Mm). These convections may affect the flux emergence. That is, a downdraft may pin down the rising tube to the bottom of the convection zone, and an upflow may help the emergence. Moreover, the strong upflow would help emergence of the weak field that could not have emerged alone, and vice versa.

Fan et al. (2003) calculated the flux emergence in the convecting interior. They found that the flux tube needs to be stronger than about  $(H_p/R_{\text{tube}})^{1/2}B_{\text{eq}} \sim 3B_{\text{eq}}$  in order for the tube to rise against the convective downflows, where  $H_p$ ,  $R_{\text{tube}}$ , and  $B_{\text{eq}}$  are the pres-

sure scale height, the tube radius, and the field strength in equipartition with the kinetic energy density of the downdraft, respectively. Using radiative MHD code, Cheung et al. (2007, 2008) performed the numerical experiments on the emergence of a horizontal tube in the photosphere filled with turbulent convections, and compared their results with SOT image taken by the *Hinode* satellite. Cheung et al. (2010) found that local granulations pin down the magnetic field to create sea-serpent field lines. Note that the serpentine field is also observed in our calculation of weakly twisted tube, which does not include the convection (see Chapter 6).

The interaction between the emerging flux and the convection leaves much room for study, especially on the interaction with larger-scale convection such as supergranulation. From the observations, Vrabel (1974) thought that the newly emerged magnetic elements are advected to the boundary of supergranulation cell. In our 3D experiment without convections, however, we have confirmed that the pores move into the edge of the subsurface field. Through convective simulations, we can figure out what makes the large- and small-scale structures of active regions. On the other hand, such a simulation using the radiative MHD needs much larger numerical resources. One approach is to mimic the convection by pseudo cooling and heating. The strategy is to reduce the temperature from the surface and add it to the bottom of the calculation domain. Isobe & Shibata (2004) presented their 3D MHD calculation of convection and flux emergence. They found that the twisted flux tube makes coronal loops. However, the loops lose their coherence in several turnover times of convection.

## 8.2 Tube Twist and Active Region Helicity

In Chapter 4 and in Chapter 6, we conducted a parameter study aiming the dependence of flux emergence on the initial tube twist. We found that the initial tube with  $q \leq 2.5 \times 10^{-4} \text{ km}^{-1}$  does not emerge further above the photosphere. It is because the rising tube expands horizontally due to the weak inward curvature force that maintains tube's

coherency. It follows that the upward magnetic pressure gradient becomes too small for the secondary emergence to take place.

The critical twist of  $2.5 \times 10^{-4} \text{ km}^{-1}$  is much larger than the observed helicity of active regions  $\sim 2 \times 10^{-5} \text{ km}^{-1}$  (see e.g. Pevtsov et al., 1997). That is, the flux tube with the observed amount of twist never rises into the corona in the numerical calculation. This would be one of the next targets of the theoretical study of flux emergence. Much wider parameter studies on the field strength, the tube radius, the total flux, and the configuration of the initial flux, and the stratification of the subphotospheric layer (stable or unstable to the convective instability), and the wavelength of the initial perturbation, etc, are needed.

## 8.3 Future Works

The following are some problems that are still remained.

**Interaction with Convection:** Several classes of convections affect the rise of magnetic flux in the solar interior. We want to figure out how they affect the rising flux in the emerging process in the photosphere as well as in the convection zone. Also we can understand the formation of umbra and penumbra through the convective collapse process.

**Tube Twist and Active Region Helicity:** The expected twist of the flux tube from the numerical modelings is much larger than the observed values. The emergence of a weakly twisted tube of order  $10^{-5} \text{ km}^{-1}$  should be studied further.

**Formation of Main Sunspots:** In the large-scale 3D experiment in Chapter 5, we did not find a pair of main sunspots. From the observations, main spots are thought to be created through the coalescence of photospheric pores (e.g. Zwaan, 1985). The key mechanism of the formation of main spots may be the emergence of the axial field of the flux tube. Such a process has been achieved by the MHD calculations

using the toroidal flux tube rather than the ordinary horizontal tube (Hood et al., 2009).

**Photospheric Undulating Field and the Resistive Emergence:** It is thought that large-scale coronal loops are created through the reconnection of smaller-scale loops aligned as a serpentine field in the lower atmosphere (resistive emergence model by Pariat et al. (2004)). The formation of undulating fields is observed by Cheung et al. (2010) in their convective MHD calculation. Also, such a field is found in Archontis & Hood (2010) and in our calculation in Chapter 6, both of which do not include the convection. The resistive emergence process is verified numerically by Isobe et al. (2007) in 2D and by Archontis & Hood (2009) in 3D. Both cases assumed the emergence of the flux sheet beneath the surface. The resistive emergence from the flux tube should be carried out.

**Global-scale Emergence:** The emergence model derived from our calculations from a depth of 20 Mm would not be so different in the emergence from  $-30$  or  $-40$  Mm, etc, although the calculation would be tougher. However, in the global-scale calculation from, say, the bottom of the convection zone ( $-200$  Mm), the Coriolis effect due to the rotation of the Sun itself may influence the emergence process (see also Appendix B).

# Appendix A

## Instabilities of a Magnetized Atmosphere

### A.1 Interchange and Undular Mode Instabilities

In Chapter 1.3, we introduced Parker (1955) to show that the isolated magnetic flux tube in a thermal equilibrium is inevitably buoyant (magnetic buoyancy). To make system in a mechanical equilibrium, as well as in a thermal equilibrium, one can consider the horizontal magnetic sheet instead of the flux tube. However, the sheet will be unstable according to the profile of the density and magnetic field, and it will partially emerge. This instability is called magnetic buoyancy instability.

This instability has several modes, and, here, the two different modes are especially mentioned. One is the interchange mode that the perturbation is perpendicular to the magnetic field ( $\mathbf{k} \perp \mathbf{B}$ , where  $\mathbf{k}$  and  $\mathbf{B}$  denote the wavenumber of the perturbation and the magnetic field vector, respectively). The other is the undular mode that the perturbation is parallel to the field ( $\mathbf{k} \parallel \mathbf{B}$ ). This mode corresponds to the bend of the field lines. The plasma at the local apex of the undulating field drains down along the field line due to the gravitation. Then, the apex becomes less dense and more buoyant, which, in turn, accelerates the instability. This mode is also called the Parker instability after his pioneering

work on the interstellar gas and magnetic field (Parker, 1966).

Here, we consider the horizontal magnetic sheet of the field  $\mathbf{B} = (B, 0, 0)$ , pressure  $p$ , and density  $\rho$  in the downward gravitation  $\mathbf{g} = (0, 0, -g)$ . This layer is illustrated in Figure A.1(a). According to Newcomb (1961), the necessary and sufficient condition for

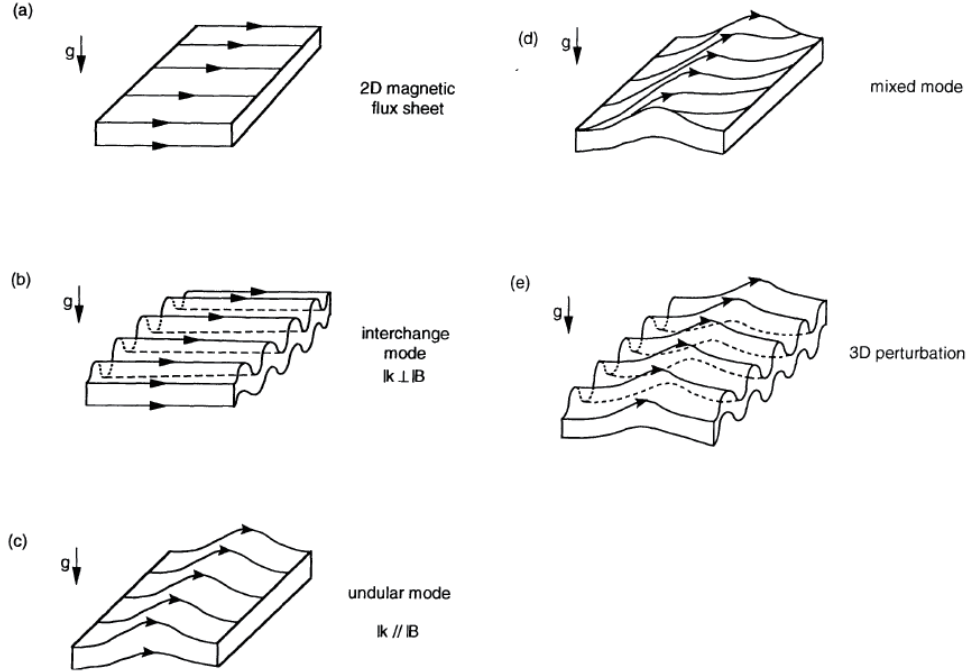


Figure A.1: A schematic illustration of the magnetic buoyancy instability in a magnetic flux sheet (Matsumoto et al., 1993).

the (pure) interchange mode instability (Figure A.1(b)) is

$$\frac{d\rho}{dz} > -\frac{\rho^2 g}{\gamma p + B^2/(4\pi)}, \quad (\text{A.1})$$

where  $\gamma$  is the ratio of specific heats. Acheson (1979) rewrote this relation as

$$\frac{d}{dz} \ln \left( \frac{B}{\rho} \right) < -\frac{N^2 C_s^2}{g V_A^2}, \quad (\text{A.2})$$

where  $N$  is the Brunt-Väisälä frequency, or the buoyancy frequency

$$N^2 = \frac{g}{\gamma} \frac{d}{dz} \ln \left( \frac{p}{\rho^\gamma} \right), \quad (\text{A.3})$$

and  $C_s$  and  $V_A$  are the sound speed and the Alfvén velocity, respectively. On the other hand, the necessary and sufficient condition for the general undular mode perturbation ( $k_x \neq 0, k_y \neq 0$ ; Figure A.1(e)) by Newcomb (1961) is

$$\frac{d\rho}{dz} > -\frac{\rho^2 g}{\gamma p}, \quad (\text{A.4})$$

which can be rewritten as (Acheson, 1979)

$$\frac{d}{dz} \ln B < -\frac{N^2}{g} \frac{C_s^2}{V_A^2}. \quad (\text{A.5})$$

If there is no perturbation perpendicular to the field line ( $k_y = 0$ ), or if the system is in a two-dimensional scheme ( $x, z$ ), this relation gives the condition for the Parker instability as in Figure A.1(c).

Comparing Conditions (A.1) and (A.4), or Conditions (A.2) and (A.5), one can see that the condition for the (pure) interchange mode is more stringent than that for the (general) undular mode. However, the typical wavelength of the Parker instability is restricted:  $\lambda_{\text{Parker}} = (10\text{--}20)H_p$ , where  $H_p$  is the local pressure scale height. It is because, if the wavelength of the perturbation is too short, the downward magnetic tension of the undulating field exceeds the upward magnetic buoyancy, and if the wavelength is too long, the downdraft of the plasma takes so long that the buoyancy will not develop. The photospheric scale height of the Sun is about 200 km. Thus, the most unstable wavelength is (2000–4000) km at the surface. According to Parker (1979), the growth time of the instability  $\tau_{\text{Parker}}$  is expressed as

$$\frac{1}{\tau_{\text{Parker}}} \simeq 0.3 \frac{V_A}{H_p}, \quad (\text{A.6})$$

that is, the growth time is of the order of three times the Alfvén transit time across one scale height. At the surface, the Alfvén velocity is  $\sim 10 \text{ km s}^{-1}$  if plasma- $\beta$  is  $\sim 1$ , and thus, the growth time is a few minutes.

## A.2 Derivation of Acheson's Condition for the Interchange Mode Instability

In Appendix A.1, we introduce the conditions for the interchange mode instability by Newcomb (1961) and Acheson (1979). Here, we show the derivation of Acheson's condition (A.2) in two ways.

### A.2.1 Derivation by the Thought Experiment

This Subsection is based on Appendix A of Acheson (1979).

Consider the horizontal layer in the magnetized atmosphere of the field  $B$  with the cross-section  $S$  initially at a level  $z$ . For the vertical displacement of  $dz$ , physical quantities inside the flux at the height  $z + dz$  are expressed as  $\phi + \delta\phi$ , and that of external media  $\phi + d\phi$ . Because of the mass conservation  $\rho S = (\rho + \delta\rho)(S + \delta S)$  and the flux conservation  $BS = (B + \delta B)(S + \delta S)$ ,

$$\frac{B + \delta B}{\rho + \delta\rho} = \frac{B}{\rho}, \text{ i.e., } \frac{\delta B}{B} = \frac{\delta\rho}{\rho}. \quad (\text{A.7})$$

If the tube is in a mechanical equilibrium, the total pressure should be equivalent to the local value:

$$(p + \delta p) + \frac{(B + \delta B)^2}{8\pi} = (p + dp) + \frac{(B + dB)^2}{8\pi}.$$

Therefore, omitting second-order values, one can get

$$\delta p + \frac{B\delta B}{4\pi} = dp + \frac{BdB}{4\pi}. \quad (\text{A.8})$$

Poisson's relation of adiabatic state  $p/\rho^\gamma = \text{constant}$  gives

$$\frac{\delta p}{p} = \gamma \frac{\delta \rho}{\rho}. \quad (\text{A.9})$$

Using Equations (A.7) and (A.9), Equation (A.8) can be rewritten as

$$\left( \gamma \frac{p}{\rho} + \frac{B^2}{4\pi\rho} \right) \delta \rho = dp + \frac{BdB}{4\pi}. \quad (\text{A.10})$$

The condition for the instability is that the density inside the lifted layer is still less than that outside ( $\delta\rho < d\rho$ ), namely,

$$\left( \gamma \frac{p}{\rho} + \frac{B^2}{4\pi\rho} \right) d\rho > dp + \frac{BdB}{4\pi}. \quad (\text{A.11})$$

Divided by  $dz$ , this relation becomes

$$\left( \gamma \frac{p}{\rho} + \frac{B^2}{4\pi\rho} \right) \frac{d\rho}{dz} > \frac{dp}{dz} + \frac{B}{4\pi} \frac{dB}{dz}. \quad (\text{A.12})$$

Multiplying it by  $4\pi/B^2$  gives

$$\frac{1}{B} \frac{dB}{dz} - \frac{1}{\rho} \frac{d\rho}{dz} < -\frac{4\pi p}{B^2} \left[ \frac{1}{p} \frac{dp}{dz} - \gamma \frac{1}{\rho} \frac{d\rho}{dz} \right],$$

namely,

$$\frac{d}{dz} \ln \left( \frac{B}{\rho} \right) < -\frac{4\pi p}{B^2} \frac{d}{dz} \ln \left( \frac{p}{\rho^\gamma} \right).$$

Using the Brunt-Väisälä frequency

$$N^2 = \frac{g}{\gamma} \frac{d}{dz} \ln \left( \frac{p}{\rho^\gamma} \right), \quad (\text{A.3})$$

and the sound speed  $C_s^2 = \gamma p / \rho$  and the Alfvén velocity  $V_A^2 = B^2 / (4\pi\rho)$ , we get Ache-

son's criterion for the interchange instability

$$\frac{d}{dz} \ln \left( \frac{B}{\rho} \right) < -\frac{N^2}{g} \frac{C_s^2}{V_A^2}. \quad (\text{A.2})$$

### A.2.2 Derivation from Newcomb's Condition

Newcomb (1961) showed the necessary and sufficient condition for the interchange mode instability as

$$\frac{d\rho}{dz} > -\frac{\rho^2 g}{\gamma p + B^2/(4\pi)}. \quad (\text{A.1})$$

By transposition, we get

$$\frac{1}{\rho} \left( \gamma p + \frac{B^2}{4\pi} \right) \frac{d\rho}{dz} > -\rho g. \quad (\text{A.13})$$

Using the equation of magnetohydrostatic equilibrium

$$\frac{d}{dz} \left( p + \frac{B^2}{8\pi} \right) = -\rho g, \quad (\text{A.14})$$

Equation (A.13) becomes

$$\frac{1}{\rho} \left( \gamma p + \frac{B^2}{4\pi} \right) \frac{d\rho}{dz} > \frac{d}{dz} \left( p + \frac{B^2}{8\pi} \right),$$

that is,

$$\left( \gamma \frac{p}{\rho} + \frac{B^2}{4\pi\rho} \right) \frac{d\rho}{dz} > \frac{dp}{dz} + \frac{B}{4\pi} \frac{dB}{dz}. \quad (\text{A.15})$$

This is the same as the relation (A.12). Therefore, we can see that Newcomb's criterion (A.1) gives Acheson's criterion (A.2) under the condition that the system is in a magnetohydrostatic equilibrium.

### A.3 Derivation of Acheson's Condition for the General Undular Mode Instability

Here, we show the derivation of Acheson's condition for the general undular mode from Newcomb's condition (Newcomb, 1961)

$$\frac{d\rho}{dz} > -\frac{\rho^2 g}{\gamma p}. \quad (\text{A.4})$$

By transposition, this relation becomes

$$\gamma \frac{p}{\rho} \frac{d\rho}{dz} > -\rho g.$$

Using Equation (A.14), we get

$$\gamma \frac{p}{\rho} \frac{d\rho}{dz} > \frac{d}{dz} \left( p + \frac{B^2}{8\pi} \right). \quad (\text{A.16})$$

Multiplying it by  $4\pi/B^2$ ,

$$\frac{1}{B} \frac{dB}{dz} < -\frac{4\pi p}{B^2} \left[ \frac{1}{p} \frac{dp}{dz} - \gamma \frac{1}{\rho} \frac{d\rho}{dz} \right], \quad (\text{A.17})$$

namely,

$$\frac{d}{dz} \ln B < -\frac{4\pi p}{B^2} \frac{d}{dz} \ln \left( \frac{p}{\rho^\gamma} \right). \quad (\text{A.18})$$

Using the Brunt-Väisälä frequency  $N$ , the sound speed  $C_s$ , and the Alfvén velocity  $V_A$ , we get Acheson's criterion for the general undular mode instability

$$\frac{d}{dz} \ln B < -\frac{N^2 C_s^2}{g V_A^2}. \quad (\text{A.5})$$

Acheson (1979) showed the criterion for the 3D undular mode instability as

$$\frac{d}{dz} \ln B < -k_{\parallel}^2 \left( 1 + \frac{k_z^2}{k_{\perp}^2} \right) H_p - \frac{N^2}{g} \frac{C_s^2}{V_A^2}, \quad (\text{A.19})$$

where  $k_{\parallel}$ ,  $k_{\perp}$ , and  $k_z$  are the wavenumbers of the perturbation in the two horizontal directions parallel and perpendicular to the magnetic field and in the vertical direction, respectively.

## A.4 Normal Mode Analysis of Undular Mode Instability

In this Section, we derive the conditions for the general and pure undular modes of magnetic buoyancy instability (Figures A.1(e) and (c)) by conducting normal mode analysis on an idealized situation. The analysis is based on Parker (1979). The initial unperturbed state is assumed as (1) the gravity is constant, (2) the gas is isothermal, and (3) the magnetic field is horizontal and (4) is stratified so that plasma  $\beta \equiv p/p_m = 8\pi p/B^2$  is constant throughout the entire volume. If we take  $z$ -coordinate to be parallel to the gravity acceleration vector  $\mathbf{g}$ , the stratification can be described as follows:

$$p_0(z) = p|_{z=0} \exp \left( -\frac{z}{H_0} \right), \quad (\text{A.20})$$

$$\rho_0(z) = \rho|_{z=0} \exp \left( -\frac{z}{H_0} \right), \quad (\text{A.21})$$

and

$$\mathbf{B}_0(z) = B_0(z) \mathbf{e}_{\parallel} = B|_{z=0} \exp \left( -\frac{z}{2H_0} \right) \mathbf{e}_{\parallel}, \quad (\text{A.22})$$

where

$$H_0 = \left(1 + \frac{1}{\beta}\right) \frac{k_B T}{mg} = \left(1 + \frac{1}{\beta}\right) H_p \quad (\text{A.23})$$

is the pressure scale height of the magnetized atmosphere, and  $e_{||}$  is the unit vector parallel to the magnetic field. Note that the subscript “0” means the equilibrium values. The basic equations are

$$\frac{\partial \rho}{\partial t} + \nabla \cdot (\rho \mathbf{V}) = 0, \quad (\text{A.24})$$

$$\frac{\partial}{\partial t}(\rho \mathbf{V}) + \nabla \cdot (\rho \mathbf{V} \mathbf{V}) = -\nabla p + \mathbf{J} \times \mathbf{B}/c + \rho \mathbf{g}, \quad (\text{A.25})$$

$$\frac{\partial \mathbf{B}}{\partial t} = \nabla \times (\mathbf{V} \times \mathbf{B}), \quad (\text{A.26})$$

$$\frac{D}{Dt} \left( \frac{p}{\rho^\gamma} \right) = 0, \quad (\text{A.27})$$

and

$$\mathbf{J} = \frac{c}{4\pi} \nabla \times \mathbf{B}. \quad (\text{A.28})$$

Separate physical quantities into equilibrium parts and perturbations:

$$\rho = \rho_0 + \rho_1, \quad (\text{A.29})$$

$$p = p_0 + p_1, \quad (\text{A.30})$$

$$\mathbf{V} = \mathbf{V}_1, \quad (\text{A.31})$$

and

$$\mathbf{B} = B_0 \mathbf{e}_{\parallel} + \mathbf{B}_1. \quad (\text{A.32})$$

Here, the subscript “1” denotes the perturbation. Considering the perturbation is small, the linearized equations of (A.24) - (A.28) are

$$\frac{\partial \rho_1}{\partial t} + \nabla \cdot (\rho_0 \mathbf{V}_1) = 0, \quad (\text{A.33})$$

$$-\rho_0 \frac{\partial \mathbf{V}_1}{\partial t} = \nabla p_1 + \frac{1}{4\pi} (\nabla \times \mathbf{B}_1) \times \mathbf{B}_0 + \frac{1}{4\pi} (\nabla \times \mathbf{B}_0) \times \mathbf{B}_1 - \rho_1 g \mathbf{e}_z, \quad (\text{A.34})$$

$$\frac{1}{\rho_0^\gamma} \frac{\partial p_1}{\partial t} - C_s^2 \frac{1}{\rho_0^\gamma} \frac{\partial \rho_1}{\partial t} + (\mathbf{V}_1 \cdot \nabla) \left( \frac{p_0}{\rho_0^\gamma} \right) = 0, \quad (\text{A.35})$$

and

$$\frac{\partial \mathbf{B}_1}{\partial t} = \nabla \times (\mathbf{V}_1 \times \mathbf{B}_0). \quad (\text{A.36})$$

We can describe perturbations as

$$\mathbf{u}_1 \equiv \sqrt{\rho_0} \mathbf{V}_1 = \Re \left\{ \sum_{\omega, \mathbf{k}} \mathbf{u}_1 \exp [i(\mathbf{k} \cdot \mathbf{x} - \omega t)] \right\}, \quad (\text{A.37})$$

$$\mathbf{B}_1 \equiv \Re \left\{ \sum_{\omega, \mathbf{k}} \mathbf{B}_1 \exp [i(\mathbf{k} \cdot \mathbf{x} - \omega t)] \right\}, \quad (\text{A.38})$$

$$D_1 \equiv \rho_1/\sqrt{\rho_0} = \Re \left\{ \sum_{\omega, \mathbf{k}} D_1 \exp [i(\mathbf{k} \cdot \mathbf{x} - \omega t)] \right\}, \quad (\text{A.39})$$

and

$$\phi_1 \equiv p_1/\sqrt{\rho_0} = \Re \left\{ \sum_{\omega, \mathbf{k}} \phi_1 \exp [i(\mathbf{k} \cdot \mathbf{x} - \omega t)] \right\}, \quad (\text{A.40})$$

where  $\omega$  and  $\mathbf{k} = (k_{\parallel}, k_{\perp}, k_z)$  are the frequency and the wavenumber vector of the perturbation, respectively. By putting these into (A.33)–(A.36), we get

$$-i\omega D_1 + ik_{\perp} u_{\perp 1} + ik_{\parallel} u_{\parallel 1} + \left( ik_z - \frac{1}{2H_0} \right) u_{z1} = 0, \quad (\text{A.41})$$

$$-i\omega u_{\perp 1} = -ik_{\perp} \phi_1 - ik_{\perp} \frac{V_A}{\sqrt{4\pi}} B_{\parallel 1} + ik_{\parallel} \frac{V_A}{\sqrt{4\pi}} B_{\perp 1}, \quad (\text{A.42})$$

$$-i\omega u_{\parallel 1} = -ik_{\parallel} \phi_1 - \frac{V_A}{\sqrt{4\pi}} \frac{1}{2H_0} B_{z1}, \quad (\text{A.43})$$

$$\begin{aligned} -i\omega u_{z1} = & - \left( ik_z - \frac{1}{2H_0} \right) \phi_1 + ik_{\parallel} \frac{V_A}{\sqrt{4\pi}} B_{z1} \\ & - \frac{V_A}{\sqrt{4\pi}} \left( ik_z - \frac{1}{2H_0} \right) B_{\parallel 1} - D_1 g, \end{aligned} \quad (\text{A.44})$$

$$-i\omega \phi_1 + i\omega C_s^2 D_1 + \frac{C_s^2}{H_0} \left( 1 - \frac{1}{\gamma} \right) u_{z1} = 0, \quad (\text{A.45})$$

$$-i\omega B_{\perp 1} = (-ik_z u_{z1} - ik_{\perp} u_{\perp 1}) \sqrt{4\pi} C_A, \quad (\text{A.46})$$

and

$$-i\omega B_{z1} = ik_{\parallel} u_{z1} \sqrt{4\pi} C_A, \quad (\text{A.47})$$

where  $C_s \equiv \gamma p / \rho$  is the sound speed and  $V_A \equiv B^2 / (4\pi\rho)$  is the Alfvén velocity. Deleting  $D_1$ ,  $u_{\perp 1}$ ,  $u_{\parallel 1}$ ,  $\phi_1$ , and  $\mathbf{B}_1$ , we get the dispersion relation

$$\begin{aligned} & (\omega^2 - k_{\parallel}^2 C_A^2) [\omega^4 - k^2 (V_A^2 + C_s^2) \omega^2 + k_{\parallel}^2 k^2 V_A^2 C_s^2] \\ & + \frac{1}{H_0^2} (\omega^2 - k_{\parallel}^2 V_A^2) \left[ -\frac{V_A^2 + C_s^2}{4} (\omega^2 + k_{\parallel}^2 V_A^2) - \left( \frac{1}{\gamma} - 1 \right) \left( \frac{C_s^2}{\gamma} + V_A^2 \right) k_{\parallel}^2 C_s^2 \right] \\ & + \frac{1}{H_0^2} \left( \frac{C_s^2}{\gamma} + \frac{V_A^2}{2} \right) k_{\perp}^2 \left[ \frac{V_A^2}{2} (\omega^2 + k_{\parallel}^2 V_A^2) - \left( \frac{1}{\gamma} - 1 \right) C_s^2 (\omega - k_{\parallel}^2 V_A^2) \right] = 0, \end{aligned} \quad (\text{A.48})$$

where  $k^2 \equiv k_{\parallel}^2 + k_{\perp}^2 + k_z^2$ . The left-hand side of Equation (A.48) is cubic in  $\omega^2$ . Here we write (A.48) as  $f(\omega^2) = 0$ . The condition for the magnetic layer to be unstable, i.e., the condition that Equation (A.48) has a solution satisfying  $\omega^2 < 0$ , is found to be  $f(\omega^2 = 0) > 0$ . That is, the condition for the general undular instability (Figure A.1(e)) is

$$\begin{aligned} & -k_{\parallel}^2 k^2 V_A^2 C_s^2 + \frac{1}{H_0^2} \left[ \frac{V_A^2 + C_s^2}{4} k_{\parallel}^2 V_A^2 + \left( \frac{1}{\gamma} - 1 \right) \left( \frac{C_s^2}{\gamma} + V_A^2 \right) k_{\parallel}^2 C_s^2 \right] \\ & + \frac{1}{H_0^2} \left( \frac{C_s^2}{\gamma} + \frac{V_A^2}{2} \right) k_{\perp}^2 \left[ \frac{V_A^2}{2} + \left( \frac{1}{\gamma} - 1 \right) C_s^2 \right] > 0. \end{aligned} \quad (\text{A.49})$$

Hereafter, we only assume the special situation that the gas is isothermal, i.e.,  $\gamma = 1$ . Then the condition reduces to

$$-k_{\parallel}^2 k^2 C_s^2 + \frac{1}{H_0^2} \frac{V_A^2 + C_s^2}{4} k_{\parallel}^2 + \frac{1}{H_0^2} \left( C_s^2 + \frac{V_A^2}{2} \right) \frac{k_{\perp}^2}{2} > 0. \quad (\text{A.50})$$

The left-hand side of Equation (A.50) is quadratic in  $k_{\parallel}^2$ :

$$-k_{\parallel}^4 + \left[ -(k_{\perp}^2 + k_z^2) + \frac{1}{4H_0^2} \left( \frac{2}{\beta} + 1 \right) \right] k_{\parallel}^2 + \frac{1}{2H_0^2} \left( 1 + \frac{1}{\beta} \right) k_{\perp}^2 > 0. \quad (\text{A.51})$$

It should be noted that  $C_s^2/V_A^2 = \gamma\beta/2$  and here we assume  $\gamma = 1$ . It follows that

$$\begin{aligned} 0 < k_{\parallel}^2 &< \frac{1}{2} \left[ -(k_{\perp}^2 + k_z^2) + \frac{1}{4H_0^2} \left( \frac{2}{\beta} + 1 \right) \right] \\ &+ \frac{1}{2} \left[ \left\{ -(k_{\perp}^2 + k_z^2) + \frac{1}{4H_0^2} \left( \frac{2}{\beta} + 1 \right) \right\}^2 + \frac{2}{H_0^2} \left( 1 + \frac{1}{\beta} \right) k_{\perp}^2 \right]^{1/2}. \end{aligned} \quad (\text{A.52})$$

To obtain the condition for the pure undular mode instability (Figure A.1(c)), let  $k_{\perp}$  and  $k_z$  be zero. Then we get

$$0 < k_{\parallel}^2 < \frac{1}{H_0^2} \left( \frac{1}{2\beta} + \frac{1}{4} \right). \quad (\text{A.53})$$

This relation shows that the magnetized layer will be unstable for a perturbation with a longer wavelength.



# Appendix B

## Tips on Flux Emergence Simulation

In this Appendix, we briefly mention some tips on the numerical experiment of flux emergence in the Thesis.

### B.1 Computational Difficulty of the Emergence from the Base of the Convection Zone

One of the most stringent conditions for calculating flux emergence from the bottom of the convection zone is the scale difference between the flux tube and the external fluid. Considering the total flux of sunspots to be  $\Phi = 10^{22}$  Mx, and the required field strength of the flux tube at the base to be  $B = 10^5$  G (see Section 1.3), the radius of the flux tube is

$$R = \sqrt{\frac{\Phi}{\pi B}} = \sqrt{\frac{10^{22} \text{ Mx}}{3.14 \times 10^5 \text{ G}}} \sim 1.7 \times 10^3 \text{ km.} \quad (\text{B.1})$$

Therefore, we need a grid spacing of a few 100 km to resolve the cross-section of the flux tube.

On the other hand, the local scale height at the base is much longer than this value.

Pressure scale height is

$$H_p = \frac{k_B T}{mg}, \quad (\text{B.2})$$

where  $k_B$ ,  $T$ ,  $m$ , and  $g$  are the Boltzmann constant, temperature, mean molecular mass, and the gravitational acceleration, respectively. That is to say, the scale height is approximately a linear function of temperature:  $H_p \propto T$ . At the surface, the scale height is about 200 km and the temperature is of the order of  $10^4$  K, while the temperature at the bottom is about a million K. Thus, the scale length at the bottom of the convective layer is a few 10,000 km.

That is to say, we have to assume a grid spacing of 100 km to resolve a flux tube, while the local pressure scale height of the external media is of 10,000 km. This results in a stringent CFL condition. Therefore, the numerical computation on the flux emergence from the bottom of the convection zone is highly inefficient.

## B.2 Importance of the Coriolis Effect

Throughout the series of numerical experiments in the Thesis, we neglect the effect of the Coriolis force in the equation of motion (2.2) and use rectangular calculation domains. It is because the time scale of the emergence (in most of our cases,  $1000\tau_0 \sim 7$  hours) is much smaller than the rotation period of the Sun from 26 days at the equator to 37 days at the poles.

More precisely, the importance of the Coriolis effect in the system can be determined by its Rossby number. The equation of motion including the Coriolis term is

$$\rho \frac{\partial \mathbf{V}}{\partial t} + \rho (\mathbf{V} \cdot \nabla) \mathbf{V} = \dots - 2\rho \boldsymbol{\Omega} \times \mathbf{V} + \dots, \quad (\text{B.3})$$

where  $\mathbf{j}$  is the current density, and  $\boldsymbol{\Omega}$  is the angular velocity vector. The Rossby number is the ratio of inertial to Coriolis term. Here, the scale of these terms are  $|\rho (\mathbf{V} \cdot \nabla) \mathbf{V}| \sim$

$\rho V^2/L$  and  $|\rho \Omega \times \mathbf{V}| \sim \rho \Omega V$ , respectively. Thus, the Rossby number is defined as

$$\text{Ro} = \frac{V^2/L}{\Omega V} = \frac{V}{\Omega L}, \quad (\text{B.4})$$

and the Coriolis force is efficient when  $\text{Ro} \ll 1$ .

If we take  $V$  and  $L$  as the typical rising velocity of the magnetic flux tube  $1 \text{ km s}^{-1}$  and the wavelength of the initial perturbation  $100 \text{ Mm}$ , respectively, and assume  $\Omega \sim 2\pi/(30 \text{ days})$ , the Rossby number of our calculations is estimated as

$$\text{Ro} = \frac{V}{\Omega L} = \frac{1 \text{ km s}^{-1}}{(2\pi/30 \text{ days}) \times 100 \text{ Mm}} \sim 4 > 1. \quad (\text{B.5})$$

Therefore, we can neglect the Coriolis effect in the experiments. When considering the emergence from the base, however, we have to take into account the Coriolis effect in the calculations, since the emergence from the base is thought to take a few month.



# Acknowledgments

I would like to express my deepest gratitude to Associate Professor Yokoyama, Takaaki, my supervisor, for his innumerable valuable comments and suggestions throughout the course of my study. I am very happy to spend my years with him and all members of his laboratory, namely, Iida, Y., Kitagawa, N., Hotta, H., and Matsui, Y.

I would like to thank Drs. Shibata, K., Isobe, H. (Kyoto Univ.), Matsumoto, R. (Chiba Univ.), Miyagoshi, T (JAMSTEC), and Magara, T. (Kyung Hee Univ.) for their precise and helpful comments. I also would like to thank Dr. Fan, Y. for supervising my two-month staying at the High Altitude Observatory (HAO), Dr. Cheung, M.C.M. for supporting my visit to the Lockheed Martin Solar and Astrophysics Laboratory (LMSAL), and Prof. Kosovichev, A. for the discussion at Stanford University. I thank all members of the Space and Magnetospheric Physics Colloquium (Univ. of Tokyo), the MHD Seminar (Kyoto Univ.), the Solar and Space Plasma Seminar (NAOJ), the Solar Terrestrial Physics Group (ISAS/JAXA), the HAO, the LMSAL, and the Stanford Solar Observatories Group (Stanford Univ.).

Numerical computations were carried out on NEC SX-8 at the Nobeyama Solar Radio Observatory (NAOJ), NEC SX-6, SX-9 (V System), and Fujitsu FX1 (M System) of the JAXA Supercomputer System, and NEC SX-9 and Cray XT4 at the Center for Computational Astrophysics (NAOJ). My research at HAO was supported by the Overseas Internship Program for Outstanding Young Earth and Planetary Researchers (OIYR Program).



# References

- Abbott, W. P., & Fisher, G. H. 2003, ApJ, 582, 475
- Acheson, D. J. 1979, Sol. Phys., 62, 23
- Archontis, V., & Hood, A. W. 2009, A&A, 508, 1469
- . 2010, A&A, 514, A56
- Archontis, V., Moreno-Insertis, F., Galsgaard, K., Hood, A., & O’Shea, E. 2004, A&A, 426, 1047
- Bernasconi, P. N., Rust, D. M., Georgoulis, M. K., & Labonte, B. J. 2002, Sol. Phys., 209, 119
- Bruzek, A. 1967, Sol. Phys., 2, 451
- . 1969, Sol. Phys., 8, 29
- Caligari, P., Moreno-Insertis, F., & Schüssler, M. 1995, ApJ, 441, 886
- Cheung, M. C. M., Moreno-Insertis, F., & Schüssler, M. 2006, A&A, 451, 303
- Cheung, M. C. M., Rempel, M., Title, A. M., & Schüssler, M. 2010, ApJ, 720, 233
- Cheung, M. C. M., Schüssler, M., & Moreno-Insertis, F. 2007, A&A, 467, 703
- Cheung, M. C. M., Schüssler, M., Tarbell, T. D., & Title, A. M. 2008, ApJ, 687, 1373
- Choudhuri, A. R., & Gilman, P. A. 1987, ApJ, 316, 788

- D'Silva, S., & Choudhuri, A. R. 1993, A&A, 272, 621
- Ellerman, F. 1917, ApJ, 46, 298
- Emonet, T., & Moreno-Insertis, F. 1998, ApJ, 492, 804
- Fan, Y. 2001, ApJL, 554, L111
- . 2009, Living Reviews in Solar Physics, 6, 4
- Fan, Y., Abbott, W. P., & Fisher, G. H. 2003, ApJ, 582, 1206
- Fan, Y., Fisher, G. H., & Deluca, E. E. 1993, ApJ, 405, 390
- Fan, Y., Zweibel, E. G., & Lantz, S. R. 1998, ApJ, 493, 480
- Fox, P. 1908, ApJ, 28, 253
- Georgoulis, M. K., Rust, D. M., Bernasconi, P. N., & Schmieder, B. 2002, ApJ, 575, 506
- Hagenaar, H. J. 2001, ApJ, 555, 448
- Hale, G. E., Ellerman, F., Nicholson, S. B., & Joy, A. H. 1919, ApJ, 49, 153
- Hanawa, T., Matsumoto, R., & Shibata, K. 1992, ApJL, 393, L71
- Harvey, K. L., & Martin, S. F. 1973, Sol. Phys., 32, 389
- Hood, A. W., Archontis, V., Galsgaard, K., & Moreno-Insertis, F. 2009, A&A, 503, 999
- Iida, Y., Yokoyama, T., & Ichimoto, K. 2010, ApJ, 713, 325
- Isobe, H., & Shibata, K. 2004, in Astronomical Society of the Pacific Conference Series, Vol. 325, The Solar-B Mission and the Forefront of Solar Physics, 63
- Isobe, H., Tripathi, D., & Archontis, V. 2007, ApJL, 657, L53
- Kosugi, T., et al. 2007, Sol. Phys., 243, 3

- Kusano, K., Moriyama, K., & Miyoshi, T. 1998, Physics of Plasmas, 5, 2582
- Leka, K. D. 1999, Sol. Phys., 188, 21
- Leka, K. D., Canfield, R. C., McClymont, A. N., & van Driel-Gesztelyi, L. 1996, ApJ, 462, 547
- Leka, K. D., & Skumanich, A. 1999, Sol. Phys., 188, 3
- Li, H., Schmieder, B., Song, M. T., & Bommier, V. 2007, A&A, 475, 1081
- Linton, M. G., Longcope, D. W., & Fisher, G. H. 1996, ApJ, 469, 954
- LongCOPE, D., Linton, M., Pevtsov, A., Fisher, G., & Klapper, I. 1999, in Measurement Techniques in Space Plasmas Fields, 93
- LongCOPE, D. W., Fisher, G. H., & Arendt, S. 1996, ApJ, 464, 999
- LongCOPE, D. W., Fisher, G. H., & Pevtsov, A. A. 1998, ApJ, 507, 417
- LongCOPE, D. W., & Klapper, I. 1997, ApJ, 488, 443
- LongCOPE, D. W., & Welsch, B. T. 2000, ApJ, 545, 1089
- Magara, T. 2001, ApJ, 549, 608
- . 2008, ApJL, 685, L91
- Magara, T., & LongCOPE, D. W. 2001, ApJL, 559, L55
- Matsumoto, R., & Shibata, K. 1992, PASJ, 44, 167
- Matsumoto, R., Tajima, T., Chou, W., Okubo, A., & Shibata, K. 1998, ApJL, 493, L43
- Matsumoto, R., Tajima, T., Shibata, K., & Kaisig, M. 1993, ApJ, 414, 357
- Miesch, M. S. 2005, Living Reviews in Solar Physics, 2, 1

Moreno-Insertis, F. 2006, in ASP Conf. Ser., Vol. 354, Solar MHD Theory and Observations: A High Spatial Resolution Perspective, 183

Moreno-Insertis, F., Caligari, P., & Schüssler, M. 1995, ApJ, 452, 894

Moreno-Insertis, F., & Emonet, T. 1996, ApJL, 472, L53

Murray, M. J., & Hood, A. W. 2008, A&A, 479, 567

Murray, M. J., Hood, A. W., Moreno-Insertis, F., Galsgaard, K., & Archontis, V. 2006, A&A, 460, 909

Newcomb, W. A. 1961, Phys. of Fluids, 4, 391

Nozawa, S. 2005, PASJ, 57, 995

Nozawa, S., Shibata, K., Matsumoto, R., Sterling, A. C., Tajima, T., Uchida, Y., Ferrari, A., & Rosner, R. 1992, ApJS, 78, 267

Otsuji, K., Kitai, R., Matsumoto, T., Ichimoto, K., Ueno, S., Nagata, S., Isobe, H., & Shibata, K. 2010, PASJ, 62, 893

Pariat, E., Aulanier, G., Schmieder, B., Georgoulis, M. K., Rust, D. M., & Bernasconi, P. N. 2004, ApJ, 614, 1099

Parker, E. N. 1955, ApJ, 121, 491

—. 1966, ApJ, 145, 811

—. 1974, ApJ, 191, 245

—. 1975, ApJ, 198, 205

—. 1979, Cosmical magnetic fields: Their origin and their activity

Pevtsov, A. A., Canfield, R. C., & McClymont, A. N. 1997, ApJ, 481, 973

- Pevtsov, A. A., Canfield, R. C., & Metcalf, T. R. 1995, ApJL, 440, L109
- Pevtsov, A. A., Maleev, V. M., & Longcope, D. W. 2003, ApJ, 593, 1217
- Schüssler, M. 1977, A&A, 56, 439
- . 1979, A&A, 71, 79
- Seehafer, N. 1990, Sol. Phys., 125, 219
- Sekii, T., et al. 2007, PASJ, 59, 637
- Sheeley, Jr., N. R. 1969, Sol. Phys., 9, 347
- Shibata, K., Tajima, T., Steinolfson, R. S., & Matsumoto, R. 1989, ApJ, 345, 584
- Solanki, S. K., Lagg, A., Woch, J., Krupp, N., & Collados, M. 2003, Nature, 425, 692
- Spruit, H. C. 1981, A&A, 98, 155
- Stix, M. 1989, The Sun. an Introduction
- Strous, L. H., Scharmer, G., Tarbell, T. D., Title, A. M., & Zwaan, C. 1996, A&A, 306, 947
- Strous, L. H., & Zwaan, C. 1999, ApJ, 527, 435
- Tsinganos, K. C. 1980, ApJ, 239, 746
- Vrabec, D. 1974, in IAU Symposium, Vol. 56, Chromospheric Fine Structure, 201
- Watanabe, H., et al. 2008, ApJ, 684, 736
- Yokoyama, T., & Shibata, K. 1995, Nature, 375, 42
- Zirin, H. 1972, Sol. Phys., 22, 34
- Zirin, H. 1974, in IAU Symposium, Vol. 56, Chromospheric Fine Structure, 161

Zwaan, C. 1978, Sol. Phys., 60, 213

—. 1985, Sol. Phys., 100, 397

—. 1987, ARAA, 25, 83